Master's thesis

NTNU
Norwegian University of Science and Technology
Faculty of Natural Sciences
Department of Physics

Joseba Miren Ormaetxea Orobengoa

Coloured intermediate band solar cells

Initial optimization of bandgaps and reflectance

Master's thesis in MSISEE Solar Cell Systems and Materials
Supervisor: Turid Reenaas
Co-supervisor: Sune Thorsteinsson
June 2023

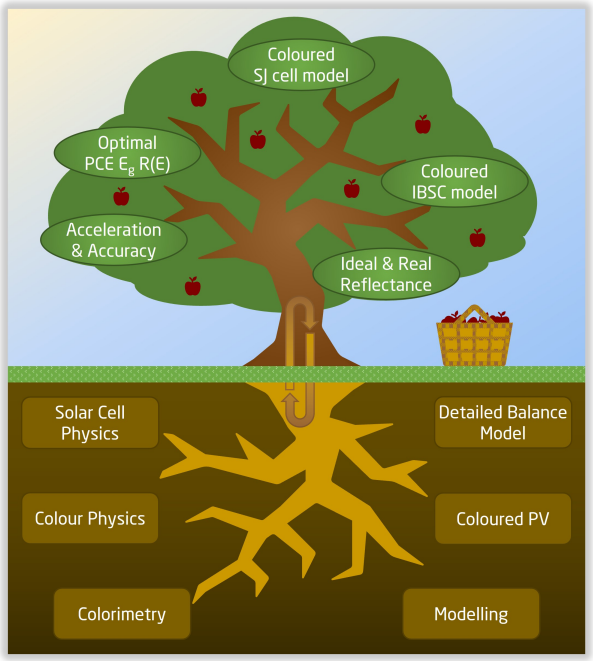

NTNU
Norwegian University of Science and Technology

Joseba Miren Ormaetxea Orobengoa

Coloured intermediate band solar cells

Initial optimization of bandgaps and reflectance

Master's thesis in MSISEE Solar Cell Systems and Materials
Supervisor: Turid Reenaas
Co-supervisor: Sune Thorsteinsson
June 2023

Norwegian University of Science and Technology
Faculty of Natural Sciences
Department of Physics

NTNU
Norwegian University of
Science and Technology

NTNU
Norwegian University of Science and Technology

Technical University of Denmark
DTU

Coloured intermediate band solar cells

Initial optimization of bandgaps and reflectance

Joseba M. Ormaetxea Orobengoa

Master's thesis, ISEE Solar Cell Systems and Materials

Submission:	June 2023
NTNU supervisor:	Turid Reenaas
DTU supervisor:	Sune Thorsteinsson

Norges Teknisk-Naturvitenskapelige Universitet - NTNU
Department of Physics
Solar Cell Physics group

Danmarks Tekniske Universitet - DTU
Department of Electrical and Photonics Engineering
Photovoltaic Materials and Systems

Abstract

The master thesis consists of the detailed balance analysis of the maximum power conversion efficiency (PCE) achievable with coloured single junction solar cells (SJSCs) and intermediate band solar cells (IBSCs). The work is based on previous work on detailed balance analysis of IBSCs by Linge and on coloured tandem solar cell optimization by Pearce et al. These are first described, together with the fundamentals of solar cell physics, the detailed balance model, third generation solar cells, colour science and coloured photovoltaic (PV) technologies.

The detailed balance model for SJSCs and IBSCs has been validated, and the code runtime has been accelerated based on approximations and simplifications, including a new MPPT algorithm for IBSCs. The reflectance spectrum has been introduced in the model to account for coloured opaque solar cells. The developed program has been employed to calculate the maximum PCE, optimum bandgaps and best rectangular-shaped reflectance spectra, for SJSCs and IBSCs with the colours of the Macbeth ColorChecker chart. The optimization of the SJSCs reproduces the results previously reported by Halme et al. The results for IBSCs are reported for the first time in this thesis and compared to those of the SJSCs. Both the coloured SJSCs and IBSCs present a power loss smaller than 12% for all but 3 colours of the Macbeth ColorChecker chart, with a linear decrease in PCE limit as a function of relative luminosity, for low values of the latter. In addition, the repeatability of the optimization algorithm has been studied. Finally, the developed models for the SJSC and IBSC have been employed to calculate the maximum PCE and the optimal bandgaps for solar cells with the reflectance spectrum of the MorphoColor solar module concept. The reflectance of the MorphoColor concept produces a 7-8% power loss with respect to a black cell for both the SJSC and IBSC, doubling the power loss caused by the optimized rectangular-shaped spectrum.

Sammendrag:

Masteroppgaven består av en grundig detaliert balanseanalyse av den maksimale effektomformingsgraden (PCE) som kan oppnås med fargede enkeltlags solceller (SJSCs) og solceller med mellombånd (IBSCs). Arbeidet er basert på tidligere arbeid med detaliert balanseanalyse av IBSCs av Linge og optimalisering av fargede tandem solceller av Pearce et al. Disse blir først beskrevet, sammen med grunnleggende prinsipper for solcelle-fysikk, den detalierte balansemodellen, tredje generasjons solceller, fargevitenskap og fargede fotovoltaiske (PV) teknologier.

Den detalierte balansemodellen for SJSCs og IBSCs er blitt validert, og kjøretiden til koden er blitt akselerert ved hjelp av tilnærmelser og forenklinger, inkludert en ny MPPT-algoritme for IBSCs. Refleksjonsspekteret er introdusert i modellen for å ta hensyn til fargede ugjennomsiktige solceller. Det utviklede programmet er blitt brukt til å beregne maksimal PCE, optimale båndgap og beste rektangulære refleksjonsspekter for SJSCs og IBSCs med fargene fra Macbeth ColorChecker-kartet. Optimaliseringen av SJSCs gjenskaper resultatene som tidligere er rapportert av Halme et al. Resultatene for IBSCs rapporteres for første gang i denne avhandlingen og sammenlignes med resultatene for SJSCs. Både de fargede SJSCs og IBSCs har en effekttap på mindre enn 12% for alle unntatt 3 farger fra Macbeth ColorChecker-kartet, med en lineær reduksjon i PCE-grensen som funksjon av relativ lysstyrke for lave verdier av sistnevnte. Videre er repetisjonsevnen til optimaliseringsalgoritmen studert. Til slutt er de utviklede modellene for SJSC og IBSC brukt til å beregne maksimal PCE og optimale båndgap for solceller med refleksjonsspekteret til MorphoColor solcellemodulkonseptet. Refleksjonen til MorphoColor-konseptet medfører et effekttap på 7-8% sammenlignet med en svart celle, både for SJSC og IBSC, og dobbelt så stort som effekttapet for det optimaliserte rektangulære spektret.

Acknowledgements

This is the final work as part of my master degree on Innovative Sustainable Energy Engineering with specialization in the Solar Cell Systems and Materials track, carried out at DTU and NTNU. I would like to thank all my classmates and colleagues of these two amazing years, as well as the professors that have taught me so much. Specially, I would like to thank my main supervisor from NTNU, Turid Reenaas, for her very helpful support and guidance during the development of this thesis, and for all the useful advice not only on academic aspects, but also about Norway in general. In the same way, I would like to show my gratitude to my supervisor from DTU, Sune Thorsteinsson, who has given me very effective input in our meetings and during the composition of this report. I must not forget to thank here Janne Halme and Phoebe Pearce, both of whom have very generously guided me in the interesting world of coloured photovoltaics with their discussions and help via email and in the meetings we shared. Of course, I would like to thank them as well for posting publicly the nice code they developed for their ECoPV project, together with Ned Ekins-Daukes and Jessica Yajie Jiang, who I thank very much too. To end with those who directly participated on the development of this thesis, I would like to mention and thank the hard work by Christer Linge, in his development of the code for detailed balance analysis of tandems of intermediate band solar cells during his thesis in the Solar Cell Physics group, and also the current members of the research groups, for the interesting talks and feedback during these months.

Finally, I would like to especially thank my family and all my friends, for their unconditional and constant support, no matter where I am.

Contents

List of Figures

List of Tables

Abbreviations

Symbols used in the text:

$\boldsymbol{\alpha}$	absorption coefficient
$\boldsymbol{\beta}$	spectral photon flux density per unit solid angle
$\boldsymbol{\gamma_s}$	solar elevation angle
$\boldsymbol{\Delta\lambda}$	wavelength step
$\boldsymbol{\epsilon}$	emissivity
$\boldsymbol{\eta}$	power conversion efficiency
$\boldsymbol{\mu}$	chemical potential
$\boldsymbol{\Phi}$	electrostatic potential
$\boldsymbol{\Omega}$	solid angle
$\boldsymbol{a}$	absorbance
$\boldsymbol{b}$	spectral photon flux density normal to the surface
$\boldsymbol{c}$	speed of light in vacuum
$\boldsymbol{E}$	energy
$\boldsymbol{E_c}$	energy of conduction band edge
$\boldsymbol{E_F}$	Fermi energy
$\boldsymbol{E_{F_i}}$ $\boldsymbol{E_{F_n}}$ $\boldsymbol{E_{F_p}}$	quasi-Fermi energy level in intermediate band; quasi-Fermi energy level of electrons in conduction band; quasi-Fermi energy level of holes in valence band
$\boldsymbol{E_g}$	bandgap energy
$\boldsymbol{E_{high}}$	highest subbandgap energy of intermediate band material
$\boldsymbol{E_i}$	Fermi energy in intrinsic semiconductor
$\boldsymbol{E_{low}}$	lowest subbandgap energy of intermediate band material
$\boldsymbol{E_v}$	energy of valence band edge
$\boldsymbol{F_a}$ $\boldsymbol{F_e}$ $\boldsymbol{F_s}$	geometrical factor relating normal to angular photon flux density for emission from: ambient; cell; sun.

$\boldsymbol{g}$	spectral photogeneration rate per unit volume
$\boldsymbol{h}$	Planck's constant
$\boldsymbol{J}$	current density
$\boldsymbol{J_0}$	reverse-bias saturation current density
$\boldsymbol{J_{amb}}$	photogenerated current density by absorption of photons from the ambient
$\boldsymbol{J_L}$	photogenerated current density by absorption of photons from the sun
$\boldsymbol{J_{rad}}$	current density lost by radiative recombination
$\boldsymbol{J_{sc}}$	short-circuit photocurrent density
$\boldsymbol{k_B}$	Boltzmann's constant
$\boldsymbol{L}$	spectral irradiance
$\boldsymbol{m}$	ideality factor
$\boldsymbol{n}$	refractive index
$\boldsymbol{P}$	power density
$\boldsymbol{q}$	electron charge
$\boldsymbol{r}$	transition rate
$\boldsymbol{R}$	reflectance
$\boldsymbol{R^2}$	coefficient of determination
$\boldsymbol{s}$	vector defining a point on surface
$\boldsymbol{T}$	temperature
$\boldsymbol{T_a}$	temperature of ambient
$\boldsymbol{T_c}$	temperature of solar cell
$\boldsymbol{T_s}$	temperature of sun
$\boldsymbol{V}$	voltage
$\boldsymbol{V_{oc}}$	open-circuit voltage

Acronyms:

2T 3T 4T	Two-, Three- and Four-Terminal
2J	Two-Junction
AM	Air Mass
AM1.5G	Air Mass 1.5 Global spectrum - standard for solar cell testing
AVR	Average Visible Reflectance
AVT	Average Visible Transmittance
a-Si	Amorphous Silicon
ARC	Anti-Reflection Coating
BAPV	Building Applied Photovoltaics
BIPV	Building Integrated Photovoltaics
c-Si	Crystalline Silicon
CB	Conduction Band
CdTe	Cadmium Telluride
CIE	International Commission on Illumination (Commission Internationale de l'Eclairage)
CIGS	Copper Indium Gallium Diselenide
CMF	Colour Matching Function
DBR	Distributed Bragg Reflector
DSSC	Die Sensitized Solar Cell
EQE	External Quantum Efficiency
IB	Intermediate Band
IBSC	Intermediate Band Solar Cell
MOEAD	Multi-Objective Evolutionary Algorithm based on Decomposition
MPP	Maximum Power Point
MPPT	Maximum Power Point Tracking
NIR	Near-Infrared
NTNU	Norwegian University of Science and Technology
NVP	Number of Voltage Points
OSC	Organic Solar Cell
PCE	Power Conversion Efficiency
PIPV	Product Integrated Photovoltaics
PSC	Perovskite Solar Cell
PV	Photovoltaic
SI	International System of Units
SJSC	Single Junction Solar Cell
SRH	Shockley-Read-Hall
UV	Ultraviolet
VB	Valence Band
VIPV	Vehicle Integrated Photovoltaics
VIS	Visible spectrum range

CHAPTER 1

Introduction

Nowadays, the global energy crisis is accelerating renewable energy expansion. First, increased fossil fuel and electricity prices have made renewable sources more economically attractive. Second, the current geopolitical instability has highlighted the energy security benefits of renewable energy.[1] Besides, based on the 2022 World Energy Outlook analysis renewable generation implementation is key to reach the Net Zero Emission scenario by 2050.[2] In this context, according to the International Energy Agency's 2022 forecast solar photovoltaic (PV) power capacity installations are expected to lead the renewable energy expansion.[1, 2]

As of 2023, the growing PV industry is dominated by crystalline silicon solar cell technologies. These accounted for 95% of the global PV production in 2021.[3] Mono-crystalline panels represent the most efficient commercial option. However, even though the industrial scale efficiencies are still increasing, the rise in record efficiencies of silicon solar cells has slowed down and nearly halted in the past five years at 26.1% power conversion efficiency (PCE) with non-concentrated light.[4, 5] This deceleration and the proximity to the theoretical Shockley-Queisser limit is making research focus on alternative technologies that could go beyond the current maximum PCE.

In light of this, third generation solar cells present alternative concepts that can exceed the physical PCE limit of silicon solar cells.[6] Among them, tandem solar cells have shown the highest efficiency and widest spread so far, reaching 47.6% under concentrated light in the lab, and with pilot production of tandem modules expected soon.[7, 8] However, there's extensive research in other third generation concepts, such as the intermediate band solar cell (with 18-19% reported record PCE under non-concentrated light).[9, 10] These cells could benefit from a potentially simpler fabrication process in comparison to tandem cells, while still reaching efficiencies above the Shockley-Queisser limit for silicon solar cells.[11]

Apart from innovation in solar cell technologies, diversification of PV applications is a hot topic in the solar industry and research, concerning both the targets and the means of integration (see Figure 1.1). The former gives an unlimited list of grid-connected and off-grid uses for PV: centralized power production, microgrid supply, powering stand-alone devices (in urban environment, remote areas or space), covering building-related needs, portable power supply, transportation, etc.[12] As for the means of integration, the most common are ground-mounted PV panels, floating PV, building applied PV (BAPV), building integrated PV (BIPV), vehicle integrated PV (VIPV) and product integrated PV (PIPV).[13]

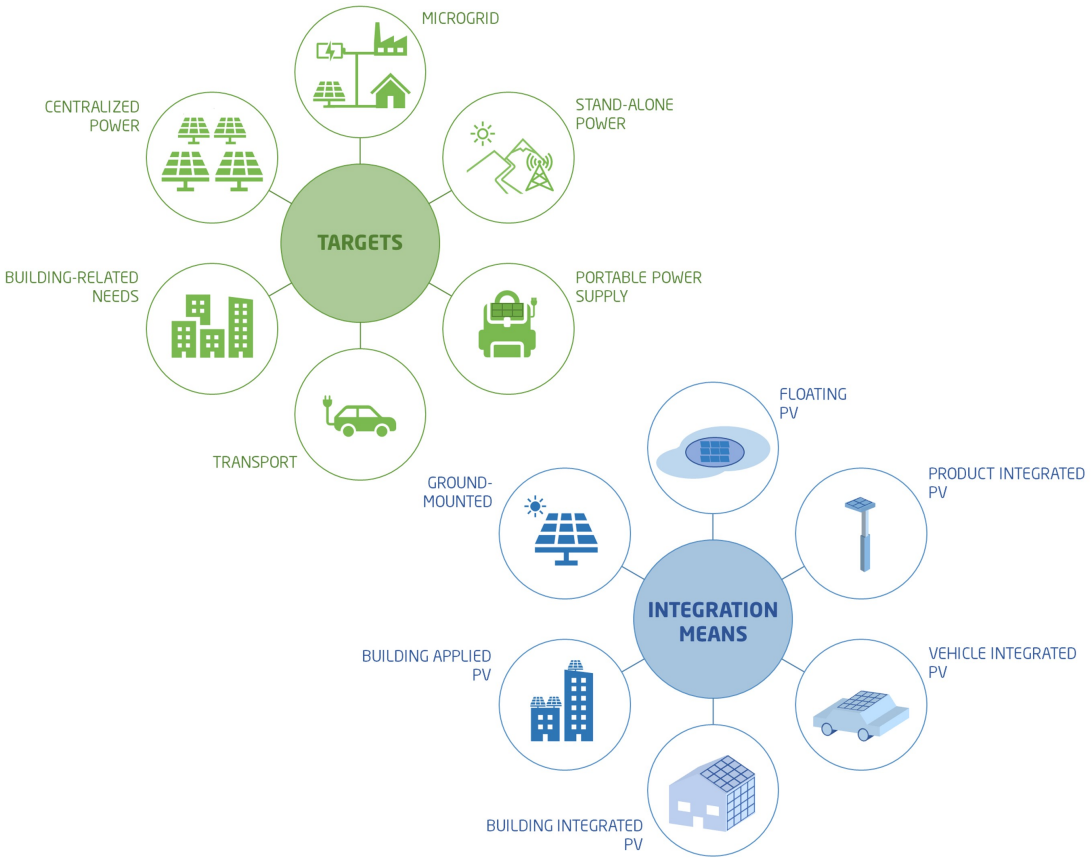

Figure 1.1: Illustration showing some of the applications of PV cells and modules.

Regarding the integration of PV in the building environment, there's growing interest in BIPV, which benefits from a dual function: generating power, and constituting the building envelope by substitution of traditional construction materials.[14]. BAPV, on the contrary, only permits power production. It has been stated that BIPV can support the transition into near-zero energy buildings and a higher renewable energy penetration.[15] The integration of PV in buildings introduces on-site electricity production, which can be partially or fully used to balance the electrical requirements of the indoor energy systems, mitigating the power supply pressures of traditional power grids (in a fast way, by relying on the already existing grid), and further reducing the fossil fuel consumption and greenhouse gas emissions.[14]

In spite of the potential benefits of BIPV, its market uptake has faced some major challenges, namely: social awareness, technical issues and low economic profitability, due to aesthetics issues, low PCE, and high cost. Some of the challenges have been addressed by improving the aesthetic quality and uniformity of BIPV installations, through appropriate mounting structures and colored products. In particular, the modules' aesthetics has been improved by modifying the perception of the original material of the PV cells through coloured layers. However, this increases the cost of the modules for different reasons: i) the manufacturing costs rise because of added layers or fabrication processes, ii) the energy yield of the PV system is reduced given the reflection of the modules, iii) the customization of the modules requires additional prototyping and testing, and iv) the fabrication of coloured PV modules is simply not scaled yet.[16] Nevertheless, it must be stated that by integrating the modules in the building skin part of the cost of conventional cladding systems is offset.

In the past years, the research of coloured PV cells and modules has grown considerably, which may partly be caused by the increased pressure on energy efficiency and renewable energy use on buildings. For example, the Energy Performance Building Directive (European Union, 2010) set a near zero energy target for new buildings after 2021, accompanied by the Renewable Energy Sources Directive, which makes the use of renewable energies compulsory in buildings (European Union, 2009).[17] This paves the way for a widespread implementation of BIPV and a greater need for customized solar systems that will structurally and aesthetically integrate in the architecture of the buildings

In this context, there's strong interest in modelling the effect of colour in the performance of solar cells.[16, 18, 19, 20, 21] This initial assessment based on simulations enables a reduction in the costs of BIPV, by allowing the evaluation of the impact of different colours in the PV system's energy yield, and by decreasing the need of prototyping and testing of modules for each considered colour.[16] Halme et al. reported a thorough study of the maximum PCE limit achievable with single junction solar cells with different colours.[20] However, as of spring 2023 no publication has been found concerning the effect of colour in 3rd generation multibandgap solar cells.

Considering the aforementioned situation, this master thesis aims to understand the effect of colour in the efficiency of third generation multibandgap solar cells. The objective is to develop and perform simulations employing the detailed balance model, in order to evaluate how the reflection of light to produce coloured PV modules can affect the maximum PCE achievable. The analysis of the results is meant to provide knowledge of the optimal coloured opaque multibandgap solar cells. This information should be contrasted with actual module coloring technologies, to comment on the potential implementation of colour in third generation solar cells.

The master thesis report is divided in 5 main chapters, which include this first introductory part. Next, Chapter 2 explains the general theory to understand the content of the project. Selected previous work on programs to perform detailed balance calculations is introduced in Chapter 3. This includes a description of the

inputs and outputs of the codes, together with the key calculations they perform. The presented MATLAB code, created by Christer Linge (master student of the Solar Cell Physics group at NTNU in 2011), is meant for black solar cells. The Python code, developed by Pearce et al. as part of the ECoPV project, can perform optimization of coloured PV cells by refining their reflectance spectra.

The modifications of the previous work, the performed simulations and their results are described and discussed in Chapter 4. It is divided in three parts. The first one regards simulations of single junction cells, and the second concerns intermediate band solar cells. Both parts begin by discussing the validation of the code and the effect of its modification to accelerate the runtime. Then, the result of introducing the reflectance is studied, so that the code is later applied to the optimization of both solar cell types with the 24 colours of the Macbeth ColorChecker chart. The third part of the chapter consists in using the developed models with the reflectance spectrum reported for the MorphoColor PV colouring concept. The maximum PCE limit attainable with this concept is compared to the maximum efficiency achievable employing an ideal rectangular shaped reflectance spectrum for the same colour.

The report ends with Chapter 5 outlining the general outcome and conclusions of the master thesis. In this last chapter, possible future work on the topic studied is suggested too.

CHAPTER 2

Theory

In this section, the theoretical concepts of the thesis are introduced, which are necessary to later comprehend the developed models and codes, and the results obtained with them. First of all, the solar radiation is briefly described. Then, the principle of operation of solar cells is explained, as well as the detailed balance model to calculate their ideal efficiency limit. This first two parts are mostly based on the book "The physics of solar cells" by Jenny Nelson.[22] Afterwards, the tandem cell and the intermediate band solar cell are introduced, which are multibandgap solar cell technologies. The modifications to the detailed balance model to compute their efficiency limit are also explained. Finally, some key concepts of colour science are summarized, followed by a short review on present coloured PV technologies, and the modifications to the detailed balance to include the colour of the solar cells.

2.1 Solar resource

Photovoltaics is the conversion of light into electrical power. Therefore, it is important to understand and describe the incident light, in order to study the conversion mechanisms and assess the PCE of solar cells. In most PV applications the light source is the Sun. So, in this section different models of the solar spectral irradiance are introduced.

2.1.1 Blackbody radiation

One of the ways to describe the spectral irradiance of the Sun is by modelling the star as a blackbody. A blackbody is an object that emits photons with a distribution of energies determined by its temperature, following Planck's law, given in equation (2.1).[23, 22] This provides the emitted spectral photon flux of the blackbody, which is the number of photons in the energy range E to E+dE emitted per unit area per unit solid angle at a point s of its surface (β_s).

$$\beta_s(E, s, \theta, \phi)d\Omega dSdE = \frac{2}{h^3c^2}\frac{E^2}{e^{\frac{E}{k_B T_s}} - 1}d\Omega dSdE \tag{2.1}$$

Outside the terrestrial atmosphere the Sun spectrum resembles the spectrum of a blackbody at 5760 K. Assuming that the temperature is uniform at all points of the surface of the Sun and the distance to the Earth is constant, the normal spectral photon flux at the surface of the planet in the absence of atmosphere (b_s) can be approximated by equation (2.2). F_s is a geometrical factor that results from the geometry of the Sun-Earth system, with a value of $2.15 \cdot 10^{-5}\pi$.[22]

$$b_s(E)dE = \frac{2F_s}{h^3c^2}\frac{E^2}{e^{\frac{E}{k_B T_s}} - 1}dE \tag{2.2}$$

One can simply multiply the spectral photon flux with the energy of the photons, to obtain the spectral irradiance (L), whose units are commonly given in $W \cdot m^{-2} \cdot nm^{-1}$, or $W \cdot m^{-3}$ in the International System of Units (SI). However, the blackbody radiation model is just an approximation of the actual spectral irradiance reaching the surface of the Earth. First, the Sun does not comply the characteristics attributed to a blackbody. Second, the photons reaching the Earth have to cross the atmosphere, which can reflect, absorb and scatter light. As discussed in the following section, there are other standardized models that describe more closely the solar spectral irradiance on Earth.

2.1.2 AM1.5G spectrum

Attenuation by the atmosphere is measured by the Air Mass factor (AM), calculated with equation (2.3). It depends on the optical path length of the light through the atmosphere, or the solar elevation angle (γ_s). The spectral irradiance measured in the surface of the Earth when the Sun is directly overhead ($\gamma_s = 90°$) is AM1. On the other hand, the spectral irradiance measured in the outer part of the atmosphere is AM0.

$$n_{AM} = \frac{\text{optical path length to Sun through atmosphere}}{\text{optical path length if Sun directly overhead}} = cosec(\gamma_s) \tag{2.3}$$

The standard irradiance spectrum usually considered is AM1.5G, the G standing for global, as it includes both the direct and diffuse components of the incident radiation. This corresponds to a 42° elevation angle of the Sun. The AM1.5G spectral irradiance used in the thesis is the ASTM G173-03 (2012) standard.[24] Figure 2.1 shows the difference between AM1.5G, AM0 and the spectral irradiance of the blackbody model at 5760K.

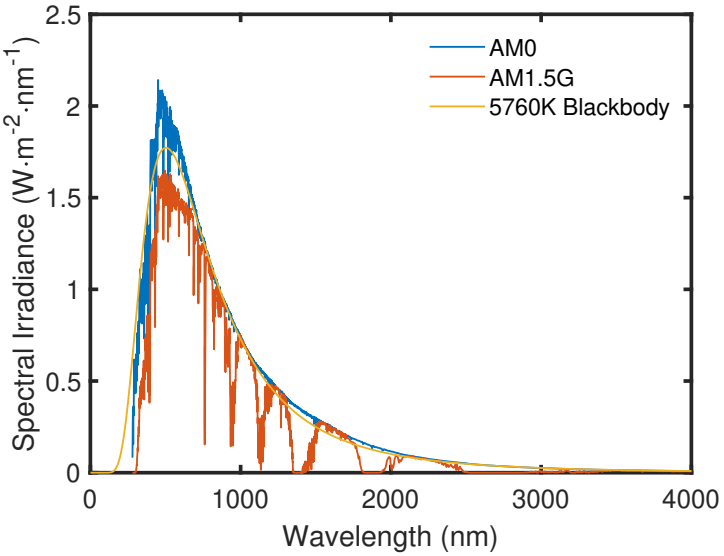

Figure 2.1: Standard extraterrestrial and terrestrial spectral irradiance of the Sun (AM0 and AM1.5G, respectively), and the spectral irradiance of the Sun according to the blackbody model at 5760K (including the geometrical factor F_s). AM0 and AM1.5G data from [24].

2.2 Solar cells

A solar cell is a device capable of turning light into electrical power via the photovoltaic effect. In this section, some basic concepts related to the operation of solar cells are introduced, as well as the carrier generation and recombination processes that take place in them. This knowledge will be useful to understand the calculation of the maximum power conversion efficiency (PCE) limit via the detailed balance model. To begin with, it is assumed that the reader has some basic knowledge of semiconductor and solar cell physics. For the sake of clarity, the initial explanation will be given with a conventional semiconductor single junction solar cell (SJSC) as example.

2.2.1 Operation principle

2.2.1.1 PN-junction

A single junction solar cell consists of a pn-junction with metal contacts on both extremes. Under dark conditions and in thermal equilibrium, the Fermi energy of the electrons is constant across the device. A schematic band diagram of the pn-junction is shown in Figure 2.2. A depletion region is formed in the interphase between the p-type and n-type semiconductor, with a built-in potential difference and electric field in it. The drift current due to the electric field and the diffusion current due to the carrier concentration difference in p- and n-regions compensate, so the net current from one side to the other is zero. When applying an external voltage between the metal electrodes the equilibrium breaks, and the current across the cell follows the Shockley equation for a pn-junction (equation (2.4)). J refers to current-density, while J_0 is the so-called reverse-bias saturation current density. q is the absolute value of the elemental electron charge, whereas k_B is the Boltzmann constant. T stands for temperature, and V for the voltage across the pn-junction. Finally, m is an ideality factor.

$$J = J_0(e^{\frac{qV}{mk_BT}} - 1) \tag{2.4}$$

The equation is derived from the diffusion-drift model for the current. For an ideal diode, the ideality factor m equals 1. As illustrated in Figure 2.3, when forward biased the diffusion current increases, while when reverse biased it is the drift current which increases.

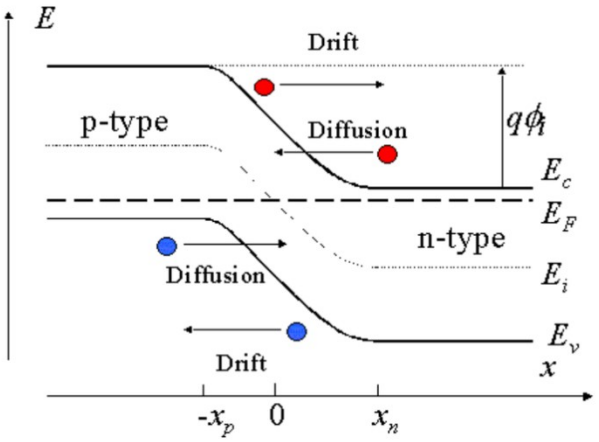

Figure 2.2: Band diagram of pn-junction under dark and no voltage applied (equilibrium). The direction of the electron (red) and hole (blue) diffusion and drift currents are indicated, as well as the constant Fermi energy and the built-in potential across the junction. Reproduced from [25].

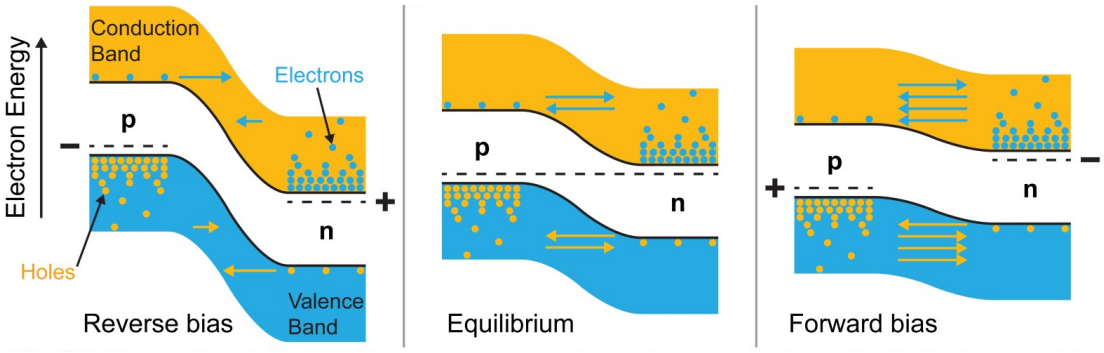

Figure 2.3: Band diagram of pn-junction under dark, in equilibrium (center) and with applied voltage in reverse (left) and forward (right) bias. Reproduced with permission from [26].

2.2.1.2 Photovoltaic effect

In most materials, when matter absorbs photons electrons are excited to higher energy states, but they quickly relax back to the ground state. In a solar cell, on the contrary, the built-in asymmetry created by the electric field in the depletion region separates the photogenerated electrons and holes before they recombine, as shown in Figure 2.4. The extra energy of the electrons on the n-side relative to the p-side creates a potential difference or electromotive force, which can drive the charge carriers through an external circuit to provide electrical power. This potential difference created when the electrodes of the solar cell are isolated is called the open-circuit voltage (V_{oc}), which is the voltage equivalent to the quasi-Fermi level split ($E_{Fn} - E_{Fp}$) between the holes in the p-side and electrons in the n-side of the junction.

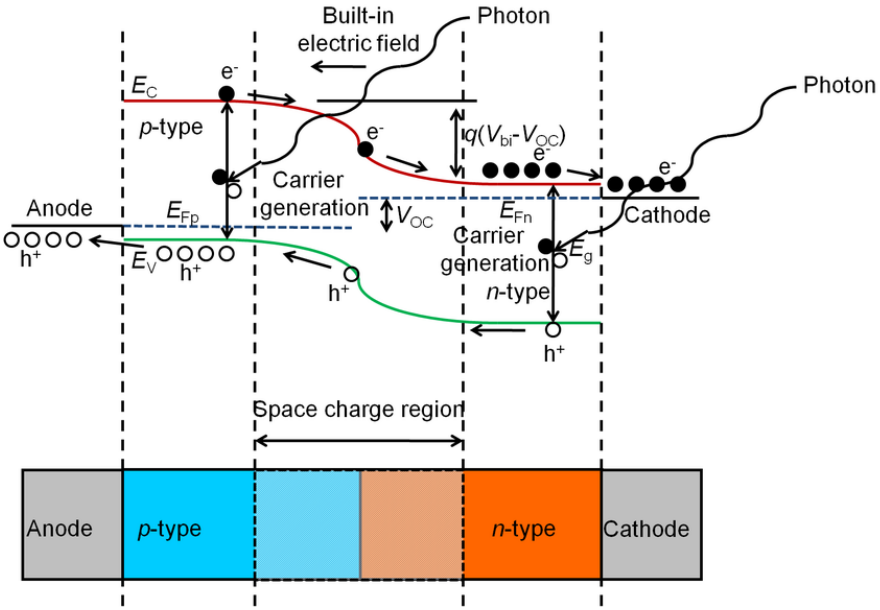

Figure 2.4: Schematic band diagram of a pn-junction solar cell under light with isolated terminals, including the cross-section of the pn-junction at the bottom. Reproduced from [27].

If the electrodes of the solar cell are short-circuited, the device provides photocurrent with the short circuit value. As shown in equation (2.5), the short-circuit photocurrent density (J_{sc}) depends on the incident light spectrum, via the cell's external quantum efficiency (EQE), which is the probability of a photon with energy E to deliver an electron in the external circuit. b_s refers to the incident spectral photon flux density normal to the surface.

$$J_{sc} = q \int b_s(E) EQE(E) dE \tag{2.5}$$

When a load is present in the external circuit, a potential difference develops between the terminals of the solar cell. The potential difference decreases the current across the cell. The reverse current (or dark current) is the one corresponding to that of the pn-junction according to equation (2.4) under an applied bias voltage, i.e. the Shockley equation for a diode. The sum of both contributions defines the current-voltage characteristic of the solar cell, provided by equation (2.6), considering an ideal diode. The sign convention for current and voltage in photovoltaics defines the photocurrent as positive.

$$J = J_{sc} - J_0(e^{\frac{qV}{k_B T}} - 1) \tag{2.6}$$

As already explained, when the terminals of the solar cell are isolated with no current output, the voltage between them is defined as the open-circuit voltage (V_{oc}). In this condition, the dark-current of the pn-junction and the short circuit photocurrent cancel out. Thus, the V_{oc} can be calculated via equation (2.7).

$$V_{oc} = \frac{k_B T}{q} ln\left(\frac{J_{sc}}{J_0} + 1\right) \tag{2.7}$$

The power density (P) provided by the solar cell to the electrical circuit is given by the product of current and voltage. There is a maximum power point (MPP) at which the cell operates providing the maximum possible power. The power conversion efficiency (η or PCE) of the solar cell is the ratio between the power at MPP and the incident irradiance on the cell (i.e. light power density, P_{in}), as given in equation (2.8).

$$\eta = \frac{P_{MPP}}{P_{in}} = \frac{J_{MPP} V_{MPP}}{P_{in}} \tag{2.8}$$

In Figure 2.5, the current-voltage characteristic of the solar cell is illustrated, both under dark and illuminated. The power provided by the solar cell at for varying voltage is also depicted. In the same plot, one can identify the already mentioned characteristic features of a solar cell: the short circuit current density (J_{sc}), the open circuit voltage (V_{oc}) and the current, voltage and power at MPP (J_{MPP}, V_{MPP}, and P_{MPP}, respectively).

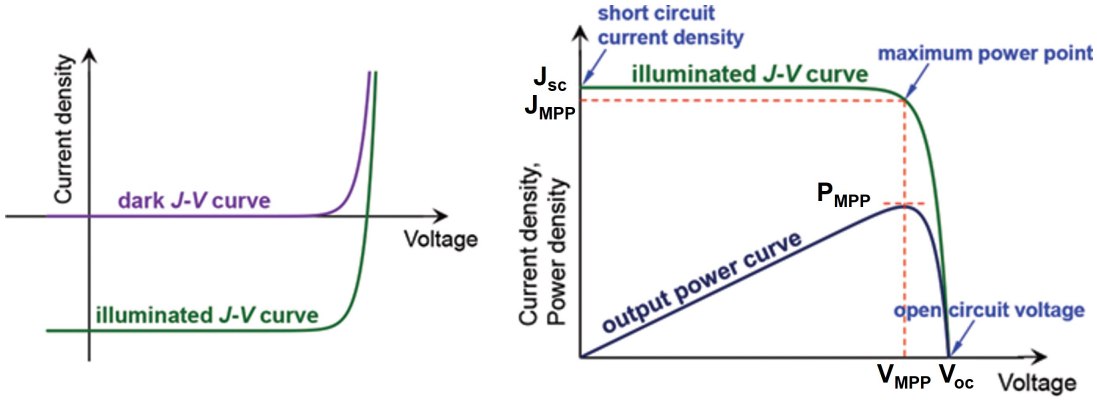

(a) (b)

Figure 2.5: Current-voltage characteristics of solar cell: (a) Dark and illuminated J-V curves with the sign convention of electrical circuits; (b) Typical representation of an illuminated J-V curve as well as the output power density curve as a function of voltage, with the sign convention for solar cells. Reproduced from [28].

The description of the solar cell operation given in this section corresponds to an ideal device, if m = 1. There are, however, non-idealities that must be taken into account (for $m \neq 1$). In order to make a more realistic description of the operation of a solar cell it is necessary to consider the paths for generation and recombination of carriers, which are shortly introduced in the next section.

2.2.2 Generation and recombination

The photocurrent provided by a solar cell depends on the generation and recombination rates of charge carriers. Generation is an electronic excitation event which increases the amount of them. On the contrary, recombination is an electronic relaxation event which decreases the amount of charge carriers. The energy needed for generation or given out in recombination is transformed from or into the vibrational energy of the lattice (phonons), light (photons) or kinetic energy of another carrier. Regarding the photovoltaic effect, to increase photocurrent the charge carriers must be generated and then extracted from the solar cell before they are recombined.

2.2.2.1 Generation mechanisms

First of all, at non-zero temperatures there's thermal generation and recombination. The vibrational kinetic energy of the lattice can excite an electron across the bandgap in a thermal generation process. Conversely, excited electrons can relax giving up vibrational energy to the lattice, in a thermal recombination process. The thermal generation and recombination rate are equal at thermal equilibrium.

Photogeneration is the most important generation process in PV devices. This

consists on electron-hole pair generation by absorption of light. The rate of photogeneration depends on the incident photon flux, its reflection at the surface, and the absorption of the photons in the semiconductor. The spectral photogeneration rate per unit volume at a depth x in the cell (g) is given by equation (2.9). This depends on the incident spectral photon flux density (b_s), the spectral reflectance (R) and the absorption coefficient (α). Other relevant generation processes are trap assisted-generation and Auger-generation.

$$g(E,x) = (1 - R(E))\alpha(E)b_s(E)e^{-\int_0^x \alpha(E,x')dx'} \tag{2.9}$$

It is important to note here that the generation rate does not only depend on the energy of the photons, because as long as they exceed the band gap energy and are absorbed they all generate an electron-hole pair regardless of their energy (that is, the same flux of photons with double the photon-energy will not double the generation current). So, it is more important to consider the number of excitation events than the amount of absorbed energy. This derives from the thermalization of the excited carriers, upon which they lose their excess thermal energy. The carriers undergo collisions with the lattice and produce phonons until they are in thermal equilibrium with the ambient. The thermalization process usually occurs very fast with respect to other competing processes, in the order of picoseconds, so the photogenerated carriers have enough time to reach thermal equilibrium.

2.2.2.2 Recombination mechanisms

Unlike generation, where photogeneration is dominant, in recombination different mechanisms can affect the PV device's operation considerably. The most important recombination mechanisms are three: radiative, Auger, and Shockley-Read-Hall (SRH) recombination.

Radiative recombination arises from spontaneous emission events in the solar cell. The radiative recombination rate (r_{sp}) can be expressed as the photon flux of the solar cell treated as a biased black body, as seen in equation (2.10). The use of the absorption coefficient (α) derives from the fact that the matrix element for optical transitions from ground to excited state and from excited to ground state must be identical (so the emission coefficient, $\epsilon = \alpha$). F_a is a geometrical factor equal to π for emission from the cell surface, and n_s is the refractive index of the solar cell, arising from the dependence on Snell's law and the total internal reflection. $\Delta\mu$ is referred to as the "chemical potential of radiation" and it corresponds to the difference on quasi-Fermi energy of holes and electrons in the p- and n-side of the junction, respectively.

$$r_{sp} = b_e(E,\Delta\mu)\alpha(E) = \frac{2n_s^2 F_a}{h^3c^2}\frac{E^2}{e^{E-\Delta\mu/k_BT} - 1}\alpha(E) \tag{2.10a}$$

$$\Delta\mu = E_{F_n} - E_{F_p} = qV \tag{2.10b}$$

Auger and SRH recombination are non-radiative recombination processes. In Auger recombination two charge carriers collide and one of them recombines across the bandgap, providing higher kinetic energy to the other. This excess kinetic energy is diffused to the lattice by thermalization.

SRH recombination involves defect or trap states in the bandgap, and is usually the most important recombination process in real solar cells. Carriers can relax to defect states, which are localized, and remain trapped until they are released by thermal activation, or they recombine with another carrier of opposite polarity that also relaxes to the defect state.

In order to improve the efficiency of solar cells it is key that photogeneration of carriers is as high as possible and that recombination processes are unlikely, so that the excited carriers can be extracted to provide power in the electrical circuit. As discussed next, the detailed balance principle provides a way to calculate the theoretical maximum PCE limit of a solar cell, in an ideal scenario where photogeneration is maximum and the recombination processes are minimized.

2.2.3 Detailed balance

The principle of detailed balance provides a method to calculate the maximum PCE limit of an ideal solar cell.[29] It is based on the fundamental law of conservation of energy and states that at equilibrium each elementary process is in equilibrium with its reverse process.[30] Thus, as well as absorbing solar radiation, the solar cell exchanges thermal radiation with its surroundings.[22] The method was originally proposed by Shockley and Queisser in 1961, when it was used to calculate the so-called Shockley-Queisser limit of single junction solar cells.[31]

Although modifications to the detailed balance model have been proposed (f.e. by including free carrier absorption and Auger recombination in addition to radiative losses), in this section the most simple case is presented.[32] The detailed balance model makes some assumptions about the ideality of the solar cells:[33]

- The reflectivity of the solar cell is zero.
- All photons with energy higher than the bandgap are absorbed to create one electron-hole pair. All photons with lower energy are not absorbed.
- The electron and hole populations relax to form separate distributions in quasi thermal equilibrium with the lattice at a temperature $T_c = T_a$ (cell temperature, which is equal to the ambient temperature) and with quasi Fermi levels separated by $\Delta\mu = qV = E_{Fn} - E_{Fp}$. This makes up the thermalization loss in the solar cell.
- The carriers have infinite mobility, and they are extracted at the chemical potential (defined by the quasi Fermi level).

- The only loss (except thermalization) is radiative recombination (spontaneous emission).
- All carriers that do not radiatively recombine are collected.

Due to conservation of energy, the power provided by the solar cell to the external circuit depends on the solar and ambient radiant energy absorbed, and on the energy lost by thermalization and spontaneous emission. However, it is easier to analyze the detailed balance in terms of currents instead of power. In this regard, the photogenerated current density due to absorption of photons coming from the sun (J_L) is given by equation (2.11a), with the external quantum efficiency (EQE) defined by equation (2.11b) (where $a(E)$ refers to the absorbance). Based on the assumptions of the detailed balance for an ideal solar cell, the EQE is 1 for photons with energy above the bandgap, and 0 for the photons with lower energy. So, J_L can be calculated as shown in equation 2.11c. The spectral photon flux incident from the sun can be obtained from the AM1.5G standard, or by modelling the Sun as a blackbody.

$$J_L = q \int_0^\infty b_s(E) EQE(E) dE \tag{2.11a}$$

$$EQE = (1 - R(E))a(E) \tag{2.11b}$$

$$J_L = q \int_{E_g}^\infty b_s(E) dE \tag{2.11c}$$

Additionally, the solar cell receives photons from the thermal radiation of the ambient, which create a current density related to the ambient (J_{amb}), as given by equation (2.12). F_a is a geometrical factor with a value of π, accounting for the fact that the ambient radiation comes from the whole upper hemisphere of the solar cell, with temperature T_a.

$$J_{amb} = q \frac{2F_a}{h^3 c^2} \int_{E_g}^\infty \frac{E^2}{e^{\frac{E}{k_B T_a}} - 1} dE \tag{2.12}$$

The solar cell provides some current density to the external circuit ($J(V)$), but it also loses some current to radiative recombination or spontaneous emission (J_{rad}). This is given by equation (2.13a), which is a generalized form of Planck's radiation law that considers that under illumination part of the electrons have raised electrochemical potential energy, and the system has developed a chemical potential $\Delta\mu > 0$ (equal to the difference in electron and hole quasi-Fermi levels of the n- and p-side of the junction). It also takes into account the energy loss due to thermalization, as the cell temperature T_c equals the ambient temperature T_a. Only photons with energy above the bandgap will be emitted. Again, F_e is a

geometrical factor which considers that the solar cell can emit to the whole upper hemisphere. Additionally, the refractive index of the solar cell medium (n_s) is related to the dependency of the emission on the available photon state density. However, accounting for total internal reflection above certain angles due to Snell's law, the $n_s^2 F_e$ factor can be substituted by π, assuming that the cell emits to air ($n = 1$).

$$J_{rad} = q\frac{2n_s^2 F_e}{h^3 c^2}\int_{E_g}^{\infty}\frac{E^2}{e^{\frac{E-\Delta\mu}{k_B T_a}}-1}dE \tag{2.13a}$$

$$\Delta\mu = qV = E_{f_n} - E_{f_p} \tag{2.13b}$$

One can consider all the current densities described (which are equivalent to an energy flux if multiplied by the bandgap energy), to calculate the current density provided by the cell to the external circuit ($J(V)$), as seen in equation (2.14). For the discussion of the detailed balance calculations of multibandgap solar cells, it is convenient to express the current as a function of the energy range in which the cell can absorb and emit (E_g to ∞, in this case) and the chemical potential of the electrons in the cell (i.e., qV), as expressed in equation (2.14c).

$$J_L + J_{amb} = J(V) + J_{rad} \tag{2.14a}$$

$$J(V) = J_L + J_{amb} - J_{rad} \tag{2.14b}$$

$$J(E_g, \infty, qV) = \int_{E_g}^{\infty}\left[qb_s(E) + q\frac{2\pi}{h^3c^2}\frac{E^2}{e^{\frac{E}{k_B T_a}}-1} - q\frac{2\pi}{h^3c^2}\frac{E^2}{e^{\frac{E-qV}{k_B T_a}}-1}\right]dE \tag{2.14c}$$

Finally, taking into account that the charge carriers are extracted at the chemical potential, one can calculate the power density provided by the cell.

$$P = V \cdot J(V) \tag{2.15}$$

Following the detailed balance model, the maximum PCE limit of a single junction solar cell under non-concentrated light is 33.77%, which corresponds to a cell with 1.34 eV band gap (also known as the Shockley-Queisser limit).[34] As previously mentioned, third generation solar cells present concepts that can go beyond this limit, which are treated in Section 2.3.

2.2.3.1 Comparison with the diffusion-drift model

One can apply the Boltzmann approximation in equation (2.14c), assuming that the equivalent in energy of the operating voltage of the solar cell (qV) is considerably lower than the energy gap of the semiconductor, in comparison to the thermal ambient energy; i.e. $(E - qV) \gg k_B T_a$. Thus, the expression describing the current provided by the solar cell can be simplified as shown in equation (2.16). This gives the same formula that is reached from the diffusion-drift model (see equation (2.6)).

$$J(E_g, \infty, qV) \simeq q \int_{E_g}^{\infty} b_s(E)dE - q\frac{2\pi}{h^3c^2} \int_{E_g}^{\infty} E^2 e^{\frac{-E}{k_B T_a}} dE \cdot (e^{\frac{qV}{k_B T_a}} - 1) \quad (2.16a)$$

$$J_{sc} = q \int_{E_g}^{\infty} b_s(E)dE \quad (2.16b)$$

$$J_0 = q\frac{2\pi}{h^3c^2} \int_{E_g}^{\infty} E^2 e^{\frac{-E}{k_B T_a}} dE \quad (2.16c)$$

$$J(E_g, \infty, qV) \simeq J_{sc} - J_0(e^{\frac{qV}{k_B T_a}} - 1) \quad (2.16d)$$

2.3 Multibandgap solar cells

Multibandgap solar cells include concepts with more than one bandgap capable of absorbing photons. The energy of the photons can be better utilized if they are absorbed by a cell with a bandgap close to its energy. This reduces the loss by thermalization. Therefore, it is convenient to have different bandgaps to absorb photons with different energies. This not only reduces thermalization loss, but it decreases the loss by transmission (or non-absorption) of photons with low energy.

Figure 2.6 shows a possible system for utilizing different bandgaps, where sunlight is split by dichroic mirrors and directed to cells with different bandgaps.[22] Nevertheless, efficient spectral splitting is hard to achieve, and the most common strategies for multibandgap exploitation include the tandem solar cell and the intermediate band solar cell (IBSC). Although there are other third generation solar cell concepts (such as the impact ionization and the hot-carrier cells), the focus of this section will be on cells with multiple bandgaps, particularly tandem cells and IBSCs.

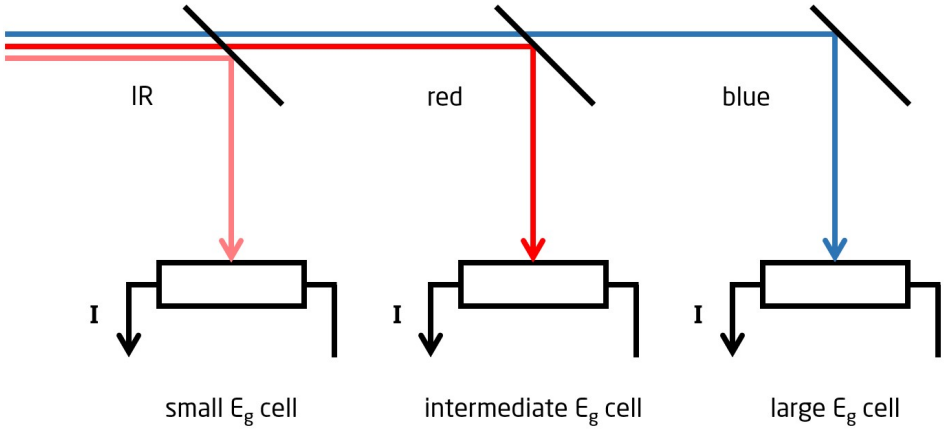

Figure 2.6: Preferential absorption of different wavelengths in solar cells with distinct bandgaps by spectral splitting of the incident light using dichroic mirrors. Adapted from [22].

2.3.1 Tandem solar cell

The tandem solar cell consists of multiple single junction solar cells built on top of each other. There are different possibilities to construct and interconnect the complete cell. Regarding the connection, in the 2-terminal (2T) device the current across all junctions must be matched, as they are connected in series (see Figure 2.7). On the other hand, the 4-terminal (4T) device consists of independently connected solar cells, enabling the separate optimization of their operation point. There are also 3-terminal (3T) devices, which are an in-between case that has been demonstrated experimentally, but not considered in this project.[35, 36, 37]

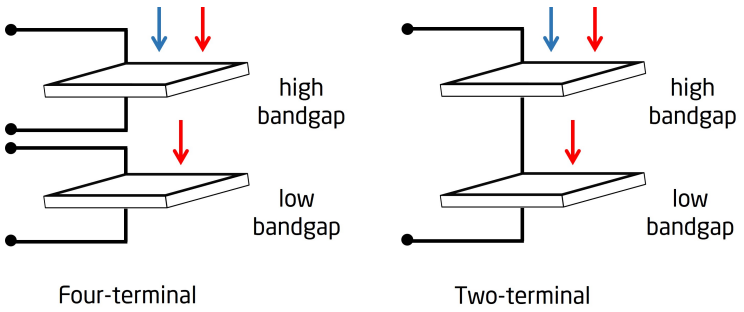

Figure 2.7: 2-terminal and 4-terminal tandem solar cell configuration with 2 subcells. In both cases, the top cell absorb short wavelength photons preferentially, while the bottom cell absorbs the longer wavelength photons. Adapted from [22].

Although both 2T and 4T tandem cells have been researched, the latter supposes a more complicated interconnection scheme. In principle, 4T tandems could provide the best power production, but in practice this is mitigated by losses associated with the more complex interconnection requirements and shading losses due to the need of lateral transport of carriers between cells.[36] Thus, the 2T devices, which are simplest to interconnect, have achieved the highest efficiency

(47.6% with a four-junction cell under concentrated light) and widest spread so far (with pilot manufacturing plants announced).[7, 8] In both cases, the junction with wider bandgap material is placed on top, so that non-absorbed less energetic photons transmit to the material with narrower bandgap below.[22]

2.3.1.1 Detailed balance in Tandem solar cells

As the solar cell concept of the tandem cell differs from the previously explained single junction solar cell, the assumptions made for the detailed balance calculation of the maximum PCE limit have to be revised. Generally, all the ideality conditions listed are maintained, but one is added in particular: the photons are absorbed in the bandgap with the highest energy as possible. This ensures that the thermalization loss is minimized, and higher energy photons are not "wasted" in lower energy absorption processes.[33]

In a 2-terminal device, the current through both junctions must be matched, and the voltage of both subcells is summed. Therefore, the maximum power density achievable by this configuration is given by equation (2.17a). The subindex 2 corresponds to the upper (wider bandgap) subcell, which absorbs and emits photons with energy $E > E_{g_2}$, whereas the bottom subcell absorbs and emits photons with $E_{g_2} > E > E_{g_1}$. The current matching condition is stated in equation (2.17b).

$$P_{max,\,2T} = (V_1 + V_2) \cdot J(E_{g2}, \infty, qV_2) \tag{2.17a}$$

$$J(E_{g2}, \infty, qV_2) = J(E_{g1}, E_{g2}, qV_1) \tag{2.17b}$$

In a 4 terminal tandem, both subcells can operate at their optimal operation point, without current matching. So, its maximum achievable power is described by equation (2.18).

$$P_{max,\,4T} = V_2 \cdot J(E_{g2}, \infty, qV_2) + V_1 \cdot J(E_{g1}, E_{g2}, qV_1) \tag{2.18}$$

The detailed balance calculation of the 2T device gives a maximum PCE of 45.3% under AM1.5G irradiant spectrum, with $E_{g_1} = 0.94eV$ and $E_{g_2} = 1.61eV$. The 4T device can theoretically achieve a slightly higher PCE of 45.7%, with $E_{g_1} = 0.95eV$ and $E_{g_2} = 1.74eV$.[38]

2.3.2 Intermediate band solar cell

The following section was reworked from the author's specialization project [39]:

The intermediate band solar cell has been proposed as a means of enhancing the energy conversion of first generation single junction solar cells.[11] According to detailed balance calculations by Luque et al., an ideal IBSC would have an efficiency limit of 63.1% under full sun concentration, instead of the 40.7% Shockley-Queisser model limit for single-junction solar cells (both calculated assuming blackbody radiation). This limit of IBSCs matches the theoretical maximum efficiency for ideal two-terminal three-junction tandem solar cells.[11, 38] Under non-concentrated AM1.5G illumination, the PCE limit of the IBSC is 49.4% according to the work by Bremner et al.[40]

An intermediate band (IB) material is characterized by the presence of a band of allowed electronic states within the semiconductor fundamental band gap (E_g) separated by a zero density of states gap from the valence band (VB) and the conduction band (CB); that is, it has an intermediate band. This gives two additional subbandgaps for absorption, E_{high} and E_{low}, as depicted in Figure 2.8. E_{high} refers to the largest of both subbandgap.[41].

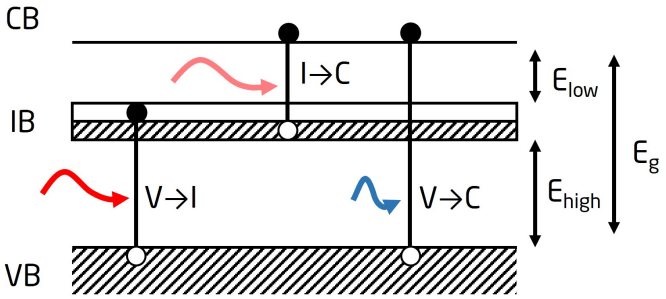

Figure 2.8: Simplified band diagram of an IB material. The three bands (VB, IB and CB), three bandgaps (E_g, E_{high} and E_{low}), and the three possible interband transitions are indicated. Adapted from [41], Copyright © 2014, IEEE.

Photons with energy higher than these subbandgaps can excite electrons from the VB or the IB, pumping them to the IB or the CB, respectively, causing transitions labelled $V \rightarrow I$ and $I \rightarrow C$ in Figure 2.8. Transition $V \rightarrow C$, from the VB to the CB, is possible by absorption of supra-bandgap energy photons.[41]

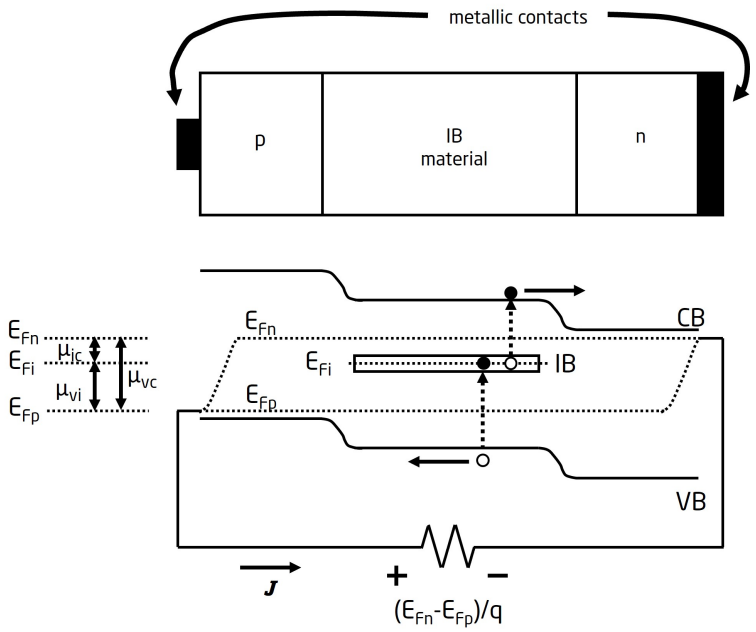

Figure 2.9: (Top) Schematic drawing of the cross section of an IBSC. (Bottom) Simplified band diagram of an IBSC under operation, with the production of the two-step subbandgap photocurrent and the splitting of the 3 quasi-Fermi levels illustrated. Adapted from [41], Copyright © 2014, IEEE.

A sketch of an IBSC under illumination is given in Figure 2.9, formed by an IB material sandwiched between a p-doped and a n-doped semiconductor, with metallic ohmic contacts in the extremes. The p- and n-semiconductors act as selective contacts for holes and electrons, respectively, allowing the collection of photogenerated carriers through the metallic contacts. Apart from the electrons excited directly from VB to CB, those pumped in a two-step process passing through the IB are also collected and contribute to the photocurrent, generating the two-photon subbandgap photocurrent.[41] As indicated in Figure 2.9, the band diagram of the IBSC in operation presents three quasi-Fermi levels, one for electrons in each band. For them to exist, the different bands must be thermally isolated and only coupled by optical transitions. The voltage of the IBSC is determined by the quasi-Fermi level split of electrons and holes in CB and VB.

In comparison with first generation single junction solar cells (SJSCs), IBSCs present potential to achieve a higher efficiency mainly due to two reasons. First, with the use of different bandgaps they are able to absorb and make use of a wider range of photons in the solar spectrum. That is, they reduce transmission losses. Second, as the absorbed photons have energies closer to the minimum necessary for the transition, less energy is lost in the thermalization processes of the photogenerated carriers.

As for the realization of IBSCs, different approaches have been investigated, divided into 4 main groups: i) nanostructures (such as quantum dots); ii) highly mismatched alloys (semiconductor alloys where bands are formed by adding oxygen or nitrogen on II-VI or III-V semiconductors, respectively); iii) semiconductor bulk materials containing a high density of deep-level impurities; and iv) organic

semiconductor molecules.[41, 42] So far, IBSCs have presented lower PCE values than their single junction counterparts, with 18-19% reported record efficiency under non-concentrated light against up to 29.1% PCE for SJSCs.[5, 9, 10] However, research is focused on finding new IB materials.[43] In this context, the Solar Cell Physics group at NTNU is currently studying Cr and N implanted TiO_2 as a candidate material for application in IBSCs.

2.3.2.1 Detailed balance in Intermediate Band Solar Cells

As the physics of the IBSC differs from that of the tandem cell and the SJSC concepts, the approximations made for the detailed balance model to calculate its maximum PCE limit need to be changed. All the ideality assumptions used for the SJSC are maintained. Likewise, as in the case of tandem cells, it is assumed that photons are absorbed in the bandgap with highest energy as possible. However, there are two additional assumptions, which state that the IB has a single energy value for all the states and that the 3 quasi-Fermi levels are thermally isolated but optically connected. This means there can be radiative transitions between them, but no non-radiative recombination processes, so that carriers achieve independent thermal equilibrium in the 3 bands. This requires that the energy gaps in the band structures are large compared with the maximum phonon energy. In addition, a selective contact should be made to the conduction band and the valence band, but not to the intermediate band, because electron populations in both IB and CB (or IB and VB) would be brought to thermal equilibrium otherwise.[22, 33]

In the IBSC, the current through both subbandgaps must be matched, as shown in equation (2.19b). In addition, the sum of the voltage across both subbandgaps must equal the voltage across the main bandgap. That is, the quasi-Fermi level difference between VB and CB is the same as the sum of the difference between quasi-Fermi levels from VB to IB, and from IB to CB, as stated by equation (2.19c). Therefore, the maximum power of the IBSC is given by equation (2.19a).

$$P_{max,\,IBSC} = (V) \cdot (J(E_g, \infty, qV) + J(E_{High}, E_G, qV_{High})) \tag{2.19a}$$

$$J(E_{High}, E_G, qV_{High}) = J(E_{Low}, E_{High}, qV_{Low}) \tag{2.19b}$$

$$qV = qV_{High} + qV_{Low} \quad \text{or} \quad \mu_c - \mu_v = (\mu_c - \mu_i) + (\mu_i - \mu_v) \tag{2.19c}$$

Now that the working principle and the detailed balance calculations of the single junction, tandem and intermediate band solar cell have been introduced, the next section deals with colour, its relevance in PV devices, and its inclusion in the detailed balance analysis.

2.4 Colour

In this section, the theoretical concepts necessary to understand the colour of solar cells and modules are briefly introduced. For that purpose, it is necessary to first define what colour is. Deane B. Judd defined color as: "*that aspect of the appearance of objects and lights which depends upon the spectral composition of the radiant energy reaching the retina of the eye and upon its temporal and spatial distribution thereon*".[44] According to the Encyclopædia Britannica, colour (or color) is "*the aspect of any object that may be described in terms of hue, lightness and saturation*".[45] The perception of colour depends on light, vision and individual interpretation, and its understanding therefore involves physics, physiology and psychology, respectively.

An object appears coloured because of the way it interacts with light, which is the concern of the physics of colour. The physiology of colour involves the eye's and the brain's response to the incoming light. Third, the psychology of colour plays a role when the mind processes visual data, compares it with memories, and interprets it as a colour.[45]

Regarding physics, color originates when the wavelengths constituting white light are absorbed, reflected, refracted, scattered, or diffracted by matter on their way to human eyes; alternatively, a non-white distribution of light may be emitted by some system.[46] 15 specific physical or chemical mechanisms concerning colour have been gathered on the books *The Physics and Chemistry of Color* and *The Science of Color*.[44, 46]

Regardless of the mechanism behind the modification of the radiation, it is the spectral composition of the light reaching the retina which will activate more or less the physiological mechanisms responsible for sensing light and colour. Thus, the focus of this section will be set on the relationship between the perceived colour and the spectral composition of the light. For the sake of simplicity, the notion "reflected" light will be employed in order to name light that has been modified by absorption, reflection, refraction, scattering, or diffraction by matter on the way to the eye.

2.4.1 Spectral composition of light and colourimetry

Most of the natural light on Earth comes from the Sun. Therefore, the starting point to study the spectral composition of light can be the AM1.5G spectrum already presented in Section 2.1.2. The human eye perceives this spectral composition as the white colour. There is a wide variety of other illuminating standards that can be used. For example, the International Commission on Illumination (CIE) D65 illuminant corresponds roughly to the solar illumination in Western and Northern Europe at noon, with a correlated colour temperature of ca. 6500 K; the D50 illuminant, with a correlated colour temperature of ca. 5000 K, approximates "warm daylight" or "horizon light", and is broadly employed in graphic arts and printing.[18, 20, 47, 48, 49, 50]

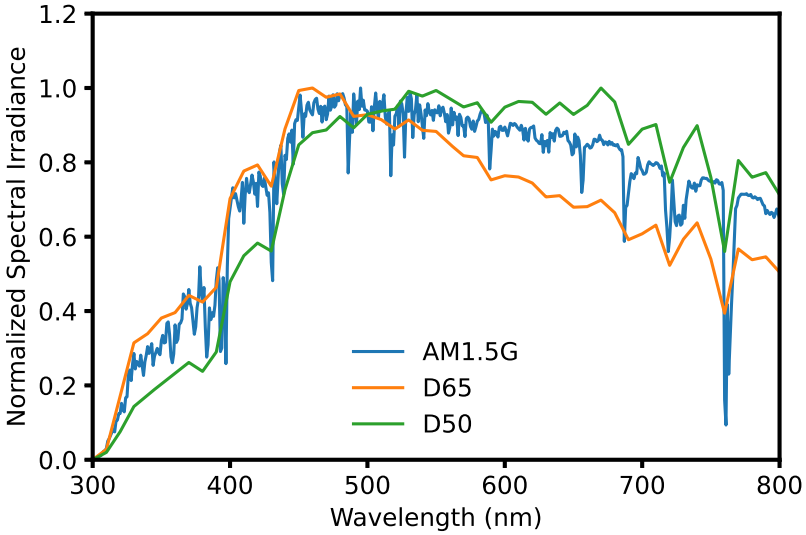

Figure 2.10: Normalized spectral irradiance of different illuminants (AM1.5G, D65 and D50) in the 300-800 nm wavelength range. Data from [24, 49, 51].

The normalized spectral irradiance of the mentioned illuminants are shown in Figure 2.10. Once the light is "reflected" by an object, its spectral composition changes, so it is perceived as a different colour to the standard white. It must be emphasized that colour is a perception, so it is not measurable by instruments. Metrology can only access the stimulus that causes the perception. Therefore, "CIE colorimetry is the metric of the psychophysical color stimulus".[52]

Colorimetry is the science that quantifies and describes human colour perception, by relating the power distribution of the electromagnetic spectrum in the visible range and the colours physiologically perceived by human vision.[16, 53] For that purpose, standardised models of the response of the human eye are used, denominated the colour matching functions (CMFs) of the CIE 1931 standard 2° colorimetric observer ($\bar{x}(\lambda)$, $\bar{y}(\lambda)$, and $\bar{z}(\lambda)$), displayed in Figure 2.11.[52] These are derived from the spectral sensitivity of the three cone types of the human eye in the short, medium, and long wavelength range of the visible spectrum (the portions of the spectrum corresponding closely to blue, green, and red, respectively).[16] Cones are the daylight receptors of the human visual system.[54] It must be stated that the $\bar{x}(\lambda)$, $\bar{y}(\lambda)$, and $\bar{z}(\lambda)$ CMFs derive from the earlier $\bar{r}(\lambda)$, $\bar{g}(\lambda)$, and $\bar{b}(\lambda)$ CMFs.[52]

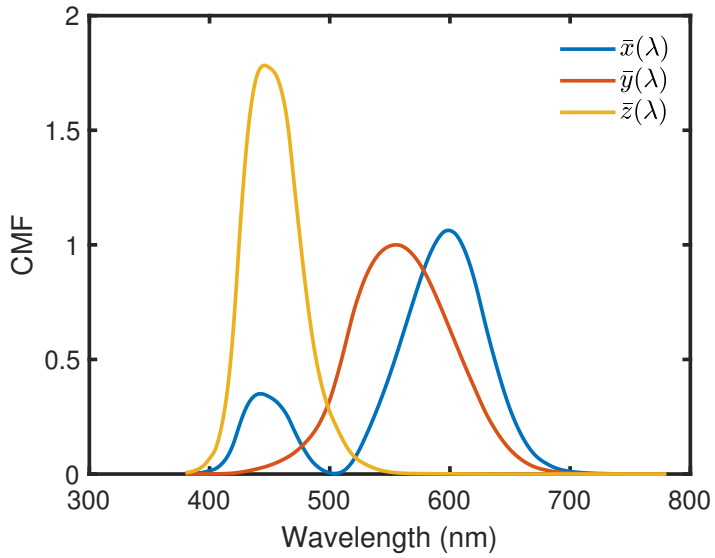

Figure 2.11: $\bar{x}(\lambda)$, $\bar{y}(\lambda)$, and $\bar{z}(\lambda)$ CIE colour matching functions. Data from [55].

2.4.2 XYZ tristimulus values

Based on the mentioned CMFs and equations (2.20), the CIE 1931 XYZ standard describes colour stimuli with X, Y and Z tristimulus values.[20, 56] The spectral irradiance of the illuminant (L) can be AM1.5G (as reported in works dealing with coloured PV cell efficiency), or a CIE standard illuminant, as recommended by CIE.[20, 52] R is the spectral reflectance of the object in question, f.e. the solar cell or module.

The XYZ tristimulus values are normalized with the maximum Y coordinate possible. The normalized Y has values between 0 (a black solar cell with complete absorption) and 1 (a white solar cell with complete reflection of all the visible light). The Y coordinate is also named relative luminosity or average visible reflectance (AVR), because the colour matching function $\bar{y}(\lambda)$ equals the photopic luminosity function (eye sensitivity).[20, 18] In equation (2.20), the visible spectrum is defined to range from 360 nm to 830 nm. However, different ranges have been proposed in the literature.[18] For example, according to the work by Lunt, while there is some visual response in the ranges from below 435 nm and above 670 nm, it is notably limited, so that these wavelengths do not contribute significantly to the overall human color perception.[57] Thus, the range of 435-670 nm is sufficient to cover over 99% of the visible light.[47, 57]

$$X = \frac{\int_{360nm}^{830nm} R(\lambda)L(\lambda)\bar{x}(\lambda)d\lambda}{\int_{360nm}^{830nm} L(\lambda)\bar{y}(\lambda)d\lambda} \tag{2.20a}$$

$$Y = \frac{\int_{360nm}^{830nm} R(\lambda)L(\lambda)\bar{y}(\lambda)d\lambda}{\int_{360nm}^{830nm} L(\lambda)\bar{y}(\lambda)d\lambda} \tag{2.20b}$$

$$Z = \frac{\int_{360nm}^{830nm} R(\lambda)L(\lambda)\bar{z}(\lambda)d\lambda}{\int_{360nm}^{830nm} L(\lambda)\bar{y}(\lambda)d\lambda} \tag{2.20c}$$

2.4.2.1 Chromaticity coordinates and chromaticity diagram

A color stimulus can be fully described by the XYZ tristimulus values. However, sometimes it is convenient to deal with chromaticity coordinates, as defined by equation (2.21), which focus on the relative magnitude of the tristimulus values. As their sum is unity ($x + y + z = 1$), it is enough to describe the chromaticity with two coordinates, usually x and y. However, a color stimulus can be described only with three characteristic quantities. Thus, if x and y are used, Y must be given too.[52] This defines the CIE xyY space.

$$x = \frac{X}{X + Y + Z} \tag{2.21a}$$

$$y = \frac{Y}{X + Y + Z} \tag{2.21b}$$

$$z = \frac{Z}{X + Y + Z} \tag{2.21c}$$

In this system, two attributes of colour are distinguished: brightness and chromaticity. For example, white is a bright color, while grey is a less bright version of that same white. So, their chromaticity is the same (x and y), but the brightness (Y) differs. By plotting the x, y chromaticity coordinates in a rectangular coordinate system the CIE 1931 chromaticity diagram from Figure 2.12 is obtained.[52] There are some peculiarities to this diagram, which can be found in many books of reference for colour science (see for example [58]).

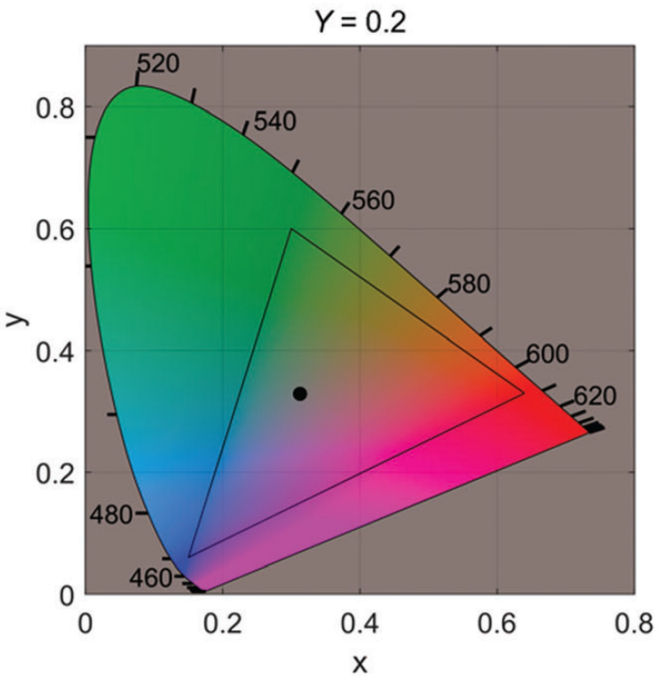

Figure 2.12: The CIE 1931 colour space xy chromaticity diagram, displaying colours with Y = 0.2. The curved edge corresponds to spectral colours product of monochromatic light, while the "purple line" at the opposite edge of the diagram consists of linear combinations of colours from the red and purple ends of the visible spectrum. The triangle marks the sRGB colour space and the black dot indicates the coordinates of the CIE D65 standard illuminant, i.e. the coordinates of achromatic grey colours. Adapted with permission from [20].

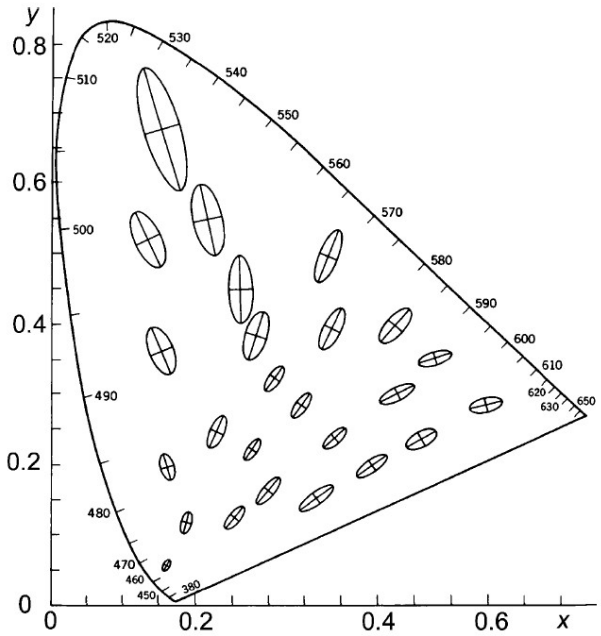

Figure 2.13: Ten times just noticeable chromaticity differences according to MacAdam's determination, showing the perceptual non-uniformity of the CIE xy chromaticity diagram. Reproduced with permission from [52].

If one observes the CIE 1931 xy chromaticity diagram from Figure 2.12, it can be noticed that the rate of colour change varies in different areas of the diagram. Figure 2.13 shows the work by David MacAdam, who studied how the distance corresponding to a just noticeable colour difference varies in the xy chromaticity diagram.[52, 59]

2.4.3 CIELab Colour Space

The practical use of colorimetry often requires information about whether two samples will be indistinguishable by visual observation or not. For that purpose, many attempts have been made to transform the xy diagram to a more perceptually uniform system (so that the MacAdam ellipses would become circles), but no perfect transformation is available.[52] Additionally, as colour stimuli are three dimensional, this requirement should extend to the three dimensions, not only the two represented in the chromaticity diagrams.

In that chase for perceptual uniformity the CIELAB Colour Space has been defined, based on equations (2.22). X, Y and Z are the tristimulus values of the test object colour stimulus considered, and X_n, Y_n and Z_n are the tristimulus values of a specified white achromatic reference illuminant (f.e., D65 or D50).[52]

$$L^* = 116 f(Y/Y_n) - 16 \tag{2.22a}$$

$$a^* = 500[f(X/X_n) - f(Y/Y_n)] \tag{2.22b}$$

$$b^* = 200[f(Y/Y_n) - f(Z/Z_n)] \tag{2.22c}$$

$$\text{where} \quad f(X/X_n) = (X/X_n)^{1/3} \ \text{ if } \ (X/X_n) > (24/116)^3 \tag{2.22d}$$

$$f(X/X_n) = (841/108)(X/X_n) + 16/116 \ \text{ if } \ (X/X_n) \leq (24/116)^3 \tag{2.22e}$$

$$\text{and} \quad f(Y/Y_n) = (Y/Y_n)^{1/3} \ \text{ if } \ (Y/Y_n) > (24/116)^3 \tag{2.22f}$$

$$f(Y/Y_n) = (841/108)(Y/Y_n) + 16/116 \ \text{ if } \ (Y/Y_n) \leq (24/116)^3 \tag{2.22g}$$

$$\text{and} \quad f(Z/Z_n) = (Z/Z_n)^{1/3} \ \text{ if } \ (Z/Z_n) > (24/116)^3 \tag{2.22h}$$

$$f(Z/Z_n) = (841/108)(Z/Z_n) + 16/116 \ \text{ if } \ (Z/Z_n) \leq (24/116)^3 \tag{2.22i}$$

In the CIELAB color space the a^* axis points more or less in the direction of red color stimuli for positive values and in the direction of green stimuli for negative values. The positive b^* axis points approximately in the direction of yellow stimuli,

and the negative in the direction of blue stimuli. Finally, L^* is related to the luminance of the stimulus, so it is directly correlated with lightness.[52] So, one can build approximate correlates of the perceived attributes lightness, chroma, and hue as shown in equation (2.23) and Figure 2.14.[52]

$$\text{CIE 1976 lightness: } L^* \tag{2.23a}$$

$$\text{CIE 1976 a,b chroma: } C^*_{ab} = (a^{*2} + b^{*2})^{1/2} \tag{2.23b}$$

$$\text{CIE 1976 a,b hue angle: } h_{ab} = arctan(b^*/a^*) \tag{2.23c}$$

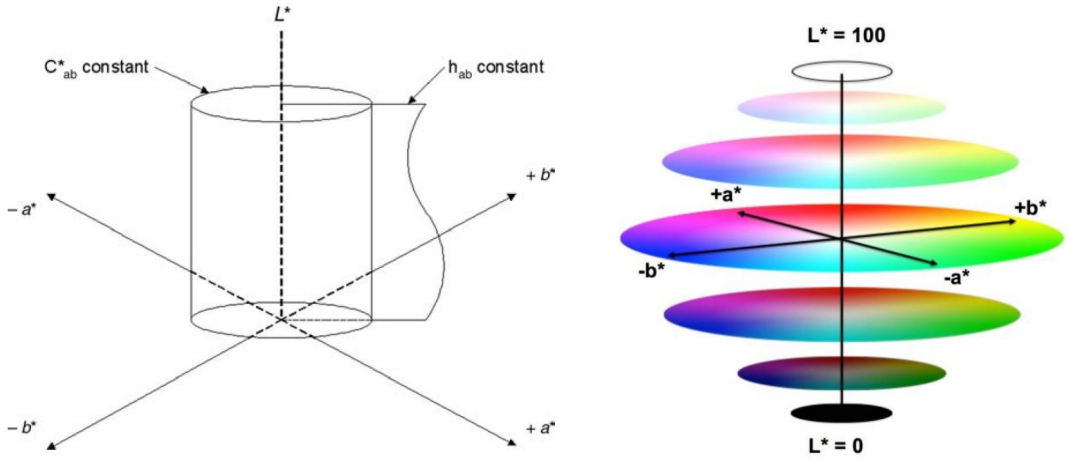

Figure 2.14: (a) A three dimensional representation of the CIELAB space showing a cylinder of constant chroma, C^*_{ab}, and a plane of constant hue angle, h_{ab}. (b) Coloured representation of the CIELAB color space. Reproduced from [52] and [60], respectively.

In fact, the International Energy Agency mostly employs the CIELAB colour space in their theoretical colour efficiency analysis on the report published as part of the Photovoltaic Power Systems Programme task 15, named *Coloured BIPV: Market, Research and Development.*[61]

2.4.3.1 Colour difference CIEDE2000

The "euclidean distances in the CIELAB color space can be used to represent approximately the perceived magnitude of color differences between object color stimuli" (see equation (2.24)).[52] However, this space is not perceptually uniform either. Many formulas have been proposed to define the difference between two colour stimuli with a numerical value and in a consistent way concerning perceptual changes. The color difference formula CIEDE2000 is the generally recommended

one nowadays, given in equation (2.25). K_L, K_C and K_H are parametric factors that depend on the experimental conditions (1 for reference conditions). The rest of variables derive from transformations of the L^*, a^* and b^* values (one can find the full derivation in [52] or [62]).

$$\Delta E^*_{ab} = \sqrt{(\Delta L^*)^2 + (\Delta a^*)^2 + (\Delta b^*)^2} \tag{2.24}$$

$$\Delta E_{00} = \sqrt{\left(\frac{\Delta L'}{K_L S_L}\right)^2 + \left(\frac{\Delta C'}{K_C S_C}\right)^2 + \left(\frac{\Delta H'}{K_H S_H}\right)^2 + R_T \left(\frac{\Delta C'}{K_C S_C}\right)\left(\frac{\Delta H'}{K_H S_H}\right)} \tag{2.25}$$

In this section, the CIEXYZ and CIELAB colour spaces and the corresponding tristimulus values have been mostly discussed, because they are of most relevance during the discussion of the methods and the results of this thesis. Nevertheless, other colour coordinates have also been developed and are found in the literature.[18, 52]

It is important to highlight, however, that there are only three types of cones to sample the entire visible spectrum range (VIS), so it is possible for two different spectral energy distributions to produce the same three cone signals. Thus, different spectral distributions can have the same XYZ or Lab values. In such cases the human visual system is unable to distinguish between the color sensations evoked, and the spectral energy distributions are said to be metamers.[54] This fact will be important when optimizing coloured solar cells, as different reflectance spectra will have to be considered for the same coloured solar cell, in order to find the optimal solution with highest PCE. That is, the reflectance spectra will also have to be optimized. In the coming section, coloring technologies applied to PV solar cells and modules in the industry and research will be briefly introduced.

2.4.4 Coloured PV technologies

As mentioned in Chapter 1, in the past years the research of coloured PV cells and modules has grown considerably. Although both coloured semi-transparent and coloured opaque solar modules can be found in the literature and the market, this section will focus on the latter, as they are the concern of the analysis performed in this thesis.

In the most basic scenario, a colour can be generated in two main ways. On the one hand, there are absorptive colours, which are based on absorbing part of the incident irradiance spectrum, showing the colour corresponding to the irradiance that is not absorbed. This is the case of traditional inks and pigments. On the other hand, the so called structural colours are created by certain optical structures on the surface of objects, which present spectrally selective scattering of light, giving the object a specific colour appearance.[63]

2.4.4.1 Colour efficiency

As mentioned before, it is important to make the colour of solar cells in the most efficient way. Several theoretical studies have been carried out about it in recent years. Peharz et al. defined colour efficiency as the ratio between the sum of the XYZ tristimulus values and the lost photocurrent due to the colour of the solar cell as compared to the black cell (see equation (2.26)).[64]

$$C_{eff} = \frac{X + Y + Z}{J_{black\ cell} - J_{coloured\ cell}} \tag{2.26}$$

Some other authors, on the contrary, have related the colour efficiency to just the Y tristimulus value, which is the relative luminosity of the colour. Røyset et al. defined their own colour performance index (CPI), as the ratio between the Y of the colour of the solar cell, and its relative power loss with respect to the black cell (P_{loss}), as shown in equation (2.27).[18]

$$CPI = \frac{Y}{P_{loss}} \tag{2.27}$$

In a similar fashion, Halme et al. studied the theoretical efficiency limit of single junction solar cells with the colors of the Macbeth ColorChecker chart, and they found a direct correlation between the maximum PCE achievable and the Y of the colour.[20]

In these studies it is demonstrated that the most efficient refletance spectra of the solar cells consist of rectangular shaped reflectance peaks, so-called pillbox spectra, with 100% reflectance in the bands. Halme et al. demonstrated that the most efficient spectra contain two rectangular reflectance bands centered around the maxima of the CMFs in the VIS.[20] It is known from colour science that any colour can be presented as a linear combination of two monochromatic colours.[65] However, current available PV colouring technologies are far from providing these pillbox reflectance spectra, and include losses because of absorption of the colouring layers, as discussed next.

2.4.4.2 Available PV colouring approaches

Different technological strategies for customizing the colour of opaque solar modules have been reported.[15, 47, 17] A first general classification of the possibilities can be made based on the position in the module where colour is introduced, as seen in Figure 2.15.[17]

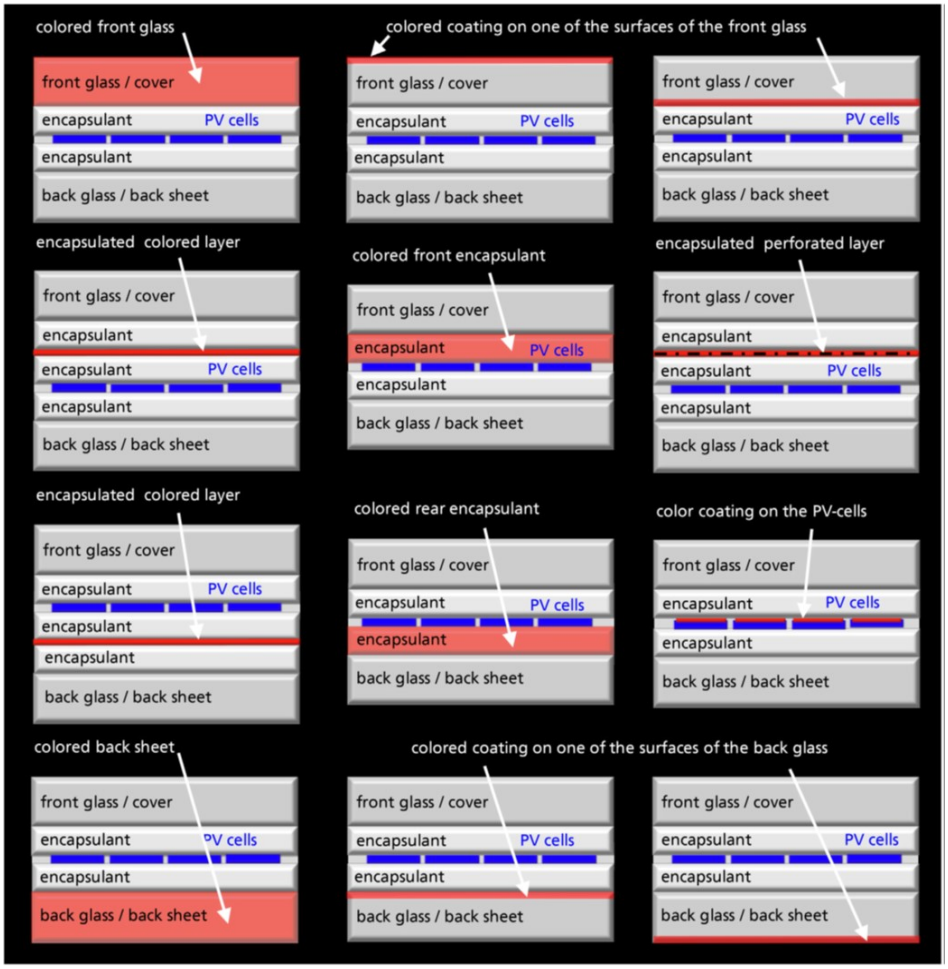

Figure 2.15: Colored PV module strategies, with technical design options sorted from outside to inside, with the outer layer on top. The colored layer or surface is highlighted in red. Reproduced from [66].

The colour can be introduced in the back of the solar cells, by modifying the encapsulant or backsheet. In thin-film modules, a coloured transparent encapsulant in the back affects transmission and reflection between the cells. With opaque wafers, the coloured layer only affects the area between the cells, which is typically minimized. Therefore, the effect is limited, yet easy to achieve.[17] The rest of modifications that follow inevitably trade efficiency against appearance, as colour results in the partial reflection of incident light that is lost for power conversion.[17]

One can modify the colour of the active material itself by properly selecting the absorber. This is the case of thin-film solar cells. Brownish-red colours can be obtained with amorphous Si (a-Si), CIGS and CdTe technologies. Other options like die sensitized, organic and perovskite solar cells (DSSC, OSC and PSC, respectively) offer a rich colour palette by varying the absorber material or the bandgap, but so far the PCE provided is low or they present short lifetime.[47] On the other hand, c-Si solar cells offer the opportunity of modifying the surface with anti-reflection coatings (ARCs), which consist of a Distributed Bragg Reflector (DBR) with multilayer films alternating high and low refractive index dielectrics.

Table 2.1: Summary of most common PV colouring technologies. Information extracted from [47].

Position	Layer	PV Tech	Strategy	Customization	PCE Loss
Below cell	Backsheet Encapsulant	c-Si	Colour area between cell	Little	None
		Thin film	Change transmission and reflection	Little	Small
In cell	Absorber	CIGS CdTe a-Si	Change absorber or thickness	Brown-red colours	None
		DSSC OSC PSC	Change composition	Many colours	Variable
	ARC	c-Si	DBR	Iridescent colours	Even <10%
Above cell	Encapsulant	All	Coloured semi-transparent layer	Large	Considerable
	Glass cover	All	DBR	Iridescent colours	Even <10%
			Print, coat or texture glass	Large	Considerable

Generally, for maximum efficiency the thickness of the ARC is selected so that the reflectance is zero near 600-700 nm in the VIS, and this involves some reflection in the blue, giving c-Si cells their characteristic appearance. However, the reflectance curve can be modified by varying the thickness, achieving alternative colours. The use of multiple layers can give even more colours. ARC dielectric layers suppose an acceptable PCE loss (<10% for most colors) and the method involves a simple integration in the current production line.[47] However, the ARC produces iridescent colours, which vary with view of angle and polarization of light.[15]

Above the solar cells and below the glass cover, a semitransparent coloured encapsulant film can be used as well.[15, 17] This can be intrinsically coloured, or printed with semi-transparent ink providing high customization potential (including patterns, f.e. brick-wall appearance). Another option in the front of the solar cell is modifying the cover glass. This can be done by deposition of a dielectric filter on the internal surface, which is called spectrally selective photonic crystal reflector or DBR.[47] In addition, the glass can be coated with painting technology adopted from the glass industry, and even textured to reduce glare or to give a different finishing: shining, matte or 3D-texture.[15, 47, 17] Both the coloured interlayer in front of the cells and the modification of the glass can hide the solar cells and provide high customization, but the effect on PCE reduction has to be considered.

Table 2.1 contains a summary of the reported PV colouring technologies. Only the most common and widely implemented strategies so far have been listed.

Some of the most efficient colouring technologies nowadays are the Kromatix and MorphoColor concept, which are based on a similar strategy.[67, 68] They combine a multi-layered coating deposited on the inner glass surface by low pressure plasma processes, with the structuring of the glass surface itself. Other PV

colouring schemes could be mentioned. However, in the following, the MorphoColor concept will be introduced shortly, as its reflectance spectrum will later be employed in the calculations of the thesis.

The MorphoColor is a PV colouring concept based on a photonic crystal structure inspired from the Morpho butterfly. It provides improved angular independent color effect, in addition to suitability for module integration and compatibility with industrial processes. Figure 2.16a shows the basic structure of the colouring dielectric multilayer deposited on top of a structured glass surface. Figure 2.16b, on the other hand, displays the appearance of the solar modules with different colors at different angles of incidence, showing the improved angular independent color effect.

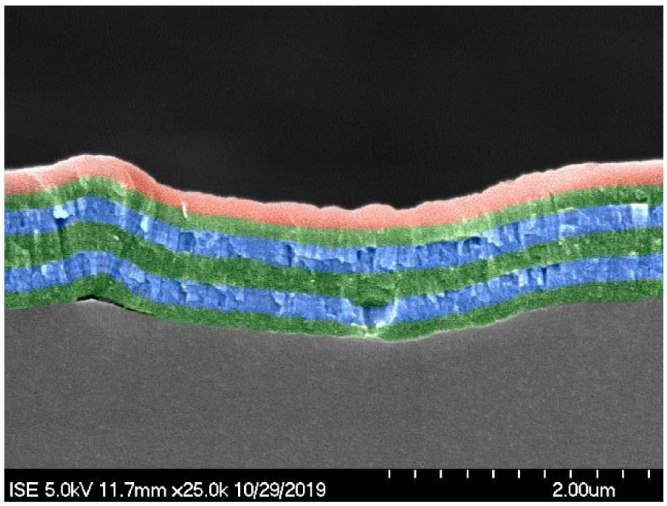

(a)

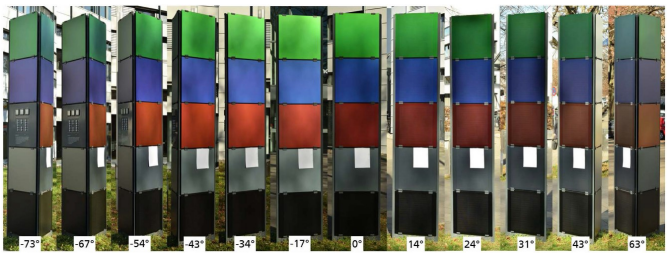

(b)

Figure 2.16: (a) SEM cross section of the layer stack deposited on the etched glass surface. The layer materials are indicated by false colors: green for SiN, blue for TiO2, and coral for SiO2. (b) Series of photographs of the demonstrator modules, taken from 12 different azimuth angles. Reproduced from [68].

Thanks to the precisely engineered layer structure, selecting the right materials in terms of refractive index, and depositing the right thicknesses, a reflectance spectrum with a sharp peak is obtained at the desired wavelength. This reflectance shape is caused by the the destructive interference of the light coming from the top and bottom of the different layers of the stack. Moreover, the use of a etched glass as a substrate with random rough surface permits a control of the angular distribution of the light, lowering the iridiscence of the color, by decreasing the

dependence of the reflectance on the angle of incidence of light. Reflectance spectra calculated by the transfer matrix method for different angles of incidence are shown in Figure 2.17, as reported by Bläsi et al. for a stack of materials switching refractive index between 2.45 and 2.01. The stack was designed to be perceived as green at a normal angle of incidence.[68]

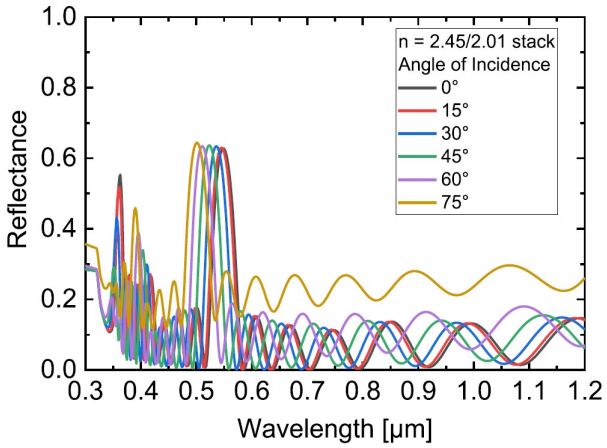

Figure 2.17: Angle dependent reflectance spectra for the module integrated 2.45/2.01 refractive index stack of the MorphoColor concept, calculated based on the transfer matrix method. Reproduced from [68].

However, newer alternative techniques have been reported. For example, the use of metal nanoparticles in different components of the modules can provide color by plasmonic scattering.[64] Dielectric nanoscatterers have also been proposed to produce bright scattering colors due to excitation of Mie resonances.[69] Another exotic example is the integration of a nanostructured optical cavity: a metal-semiconductor-metal sandwich can form a Fabry-Perot resonator, and by varying the thickness of the semiconductor different colours can be rendered.[70]

These new colouring strategies aim at minimizing undesired PCE loss (for example by reducing parasitic absorption, or reflection outside the VIS), but at the same time providing an economically feasible and highly customizable solution. As stated many times already, the introduction of colour requires reflection, reducing the amount of photons reaching the absorber and available for power production. This will have to be considered in the simulation of coloured multibandgap solar cells. Therefore, it is necessary to analyze how a non-zero spectral reflectance affects the detailed balance calculations, as explained in the coming section.

2.4.4.3 Modifications to detailed balance due to reflection

In order to present a colour other than black, a solar cell must have non-zero reflectance in the visible spectrum range. Therefore, the first of the ideality assumptions listed in Section 2.2.3 for the detailed balance model is cancelled. In terms of the equations, the modification is introduced by stating that EQE is not 1 for all the energies above the bandgap, but it depends on the reflectance as stated

previously in equation (2.11b). Assuming that the solar cell still presents ideal absorptivity above the bandgap energy ($a(E) = 1$ for $E > E_g$), the expressions for the generation and recombination currents are modified as shown in equations (2.28). It is important to highlight that the effect of reflectance must be included not only in the absorption of the incoming photons (both from the Sun and the ambient), but also in the loss by radiative emission, due to the principle of detailed balance.

$$J_L = q \int_0^\infty (1 - R(E)) b_s(E) dE \tag{2.28a}$$

$$J_{amb} = q \frac{2F_a}{h^3 c^2} \int_{E_g}^\infty (1 - R(E)) \frac{E^2}{e^{\frac{E}{k_B T_a}} - 1} dE \tag{2.28b}$$

$$J_{rad} = q \frac{2n_s^2 F_e}{h^3 c^2} \int_{E_g}^\infty (1 - R(E)) \frac{E^2}{e^{\frac{E-\Delta\mu}{k_B T_c}} - 1} dE \tag{2.28c}$$

To find the maximum achievable efficiency for each colour, it will be assumed that the solar cells present the right reflectance spectrum in the visible range, with no reflection in the ultraviolet (UV) or near-infrared (NIR) regions. Moreover, it will be considered that the colouring layers will cause no parasitic absorption, which would cause a lower PCE. This is an idealistic case, and the accepted assumptions will have to be compared with the characteristics achievable with current PV colouring technologies, in order to discuss how close to reality the calculated maximum PCE limits are.

CHAPTER 3

Previous work

In this chapter, the simulation methods and the codes implemented in previous work by others are explained. Performing detailed balance calculations inherently requires working with a model, so the models framed for the calculations will also be described.

The initial idea of the project was to base the developed model and code on the Master Thesis by Christer Linge in the Solar Cell Physics group, who implemented a model to perform detailed balance calculations of solar cells in MATLAB.[71] During the initial stages on the implementation of the colour of the solar cell in the model, Dr. Janne Halme from Aalto University was contacted, as he is one of the authors of the article "Theoretical efficiency limits of ideal coloured opaque photovoltaics".[20] Dr. Halme and Dr. Pearce, from the University of New South Wales (UNSW) Sydney, shared their Python code by making it public in Github, which they developed in collaboration with Dr. Ekins-Daukes (UNSW Sydney) and Dr. Jiang (UNSW Sydney).[55] They also provided help and feedback for the use of their code, as I was its first external user.

So, in this third chapter, the models created previously by Linge and Pearce et al. in MATLAB and Python, respectively, will be described. Afterwards, the modifications of the models and methods for their use in the present master thesis will be explained, but this will be introduced step by step in Chapter 4, together with the results caused by the modifications.

3.1 MATLAB Code

The program created by Linge in MATLAB can perform detailed balance calculations of tandems of IBSC-IBSC, IBSC-SJSC and SJSC-IBSC, both in 2T and 4T configuration, for different light concentration levels. It essentially computes the maximum PCE achievable with different bandgap combinations using the detailed balance model. However, for the implementation during this thesis, it is most interesting to study the basics of the code, which performs detailed balance calculations of SJSCs, 2T and 4T two junction tandem solar cells, and IBSCs, with non-concentrated light. This section first describes the inputs of the code, then the calculations performed based on the detailed balance model, and finally the output results provided for the solar cell types mentioned, which are summarized in Figure 3.1.

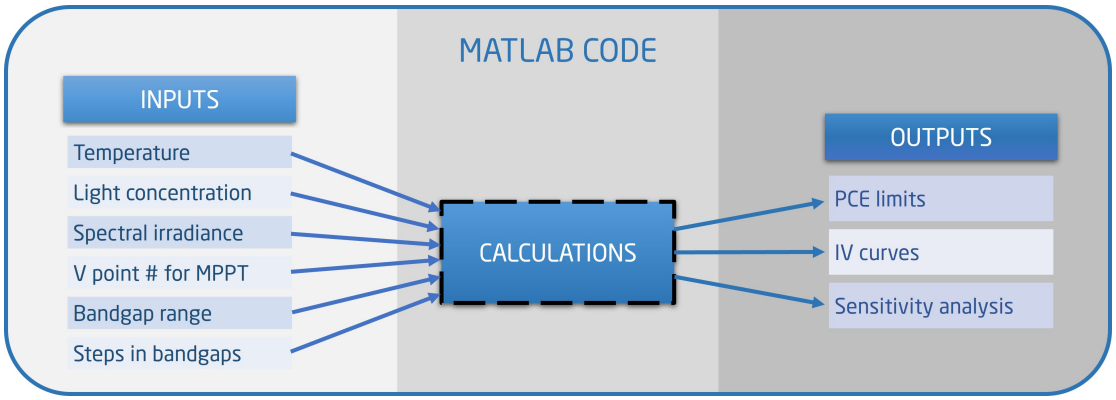

Figure 3.1: General overview of code implemented in MATLAB for detailed balance analysis of SJSCs, 2T- and 4T-tandems, and IBSCs.

3.1.1 Input

The model requires some basic input data and parameters regardless of the solar cell type, and some other that depend on the solar cell type. For all of them it is necessary to determine the temperature (300 K by default), the light concentration level (1 by default), the incident irradiance spectrum (ASTM G173-03 (2012) AM1.5G with 1 nm resolution by default), the number of voltage points (NVP) for MPP tracking with V sweep method (500 by default), and the step length in bandgaps calculated (0.05 eV by default).

For the SJSC, one must specify the bandgap range to study. For the 2T and 4T double-junction tandem cells the bandgap range of the bottom ($E_{g,bot}$) and top ($E_{g,top}$) cells must be stated. For the IBSC the bandgap range of the main bandgap (E_g) and the low subbandgap (E_{low}) must be specified (the low subbandgap is equal or smaller than half the main bandgap, i.e. it is always equal or smaller than the high subbandgap). Besides, for the 2T tandem and the IBSC, the maximum error tolerated in the current matching of the subcells or subbandgaps has to be determined.

3.1.2 Calculations

For the detailed balance calculations, the models implemented for the SJSC, tandem solar cell and IBSC are exactly the ones explained in Sections 2.2.3, 2.3.1.1 and 2.3.2.1, respectively.

3.1.2.1 Single junction solar cell

In the case of SJSCs, for every bandgap specified in the input (according to the bandgap range and step length stated), the same calculation is performed. A simple V sweep MPPT method is employed to find the MPP. First, the current of the cell is calculated in NVP divided by 10 equispaced voltage values between 0 V and the voltage corresponding to the bandgap energy, employing equation (2.14c). The lowest voltage point with a 0.0001% relative difference to the previous voltage point is set as the starting voltage for the MPPT. Then, the current and power density of the cell is calculated in some voltage points (NVP) equispaced between this starting voltage and the voltage corresponding to the bandgap energy, using equations (2.14c) and (2.15). Thus, the MPP is selected for each bandgap value. A simplified diagram of the calculation algorithm is represented in Figure 3.2.

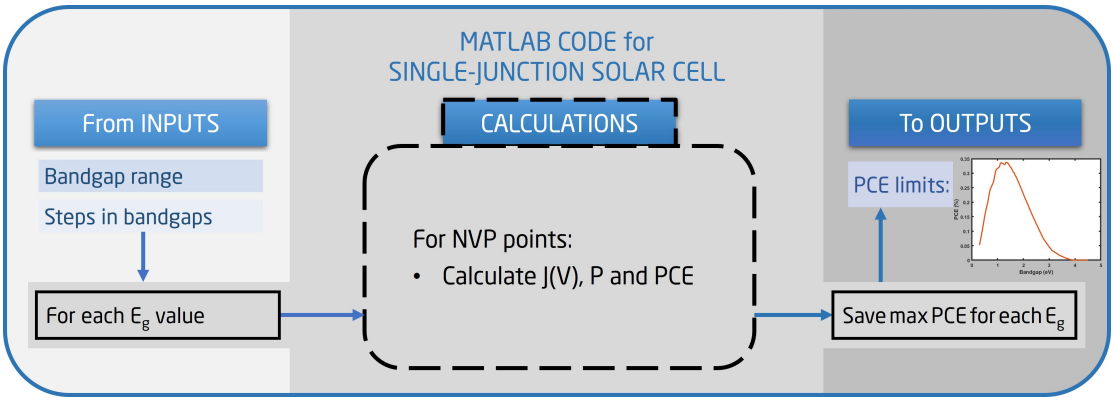

Figure 3.2: Simplified diagram of the calculations based on the detailed balance model for SJSCs implemented in MATLAB.

3.1.2.2 4T double junction tandem solar cell

For the 4T double junction (2J) tandem solar cells, the process is similar. For every top and bottom bandgap combination specified in the input (according to the bandgap range and step length stated), the same calculation is employed. Without going into details about the exact coded algorithm, the current and power provided by the 4T-tandem is calculated for different voltage values in both subcells. Equations (2.14c) and (2.18) are employed for that purpose, applying the same MPP algorithm as described for the SJSC but for each subcell of the tandem. Then the MPP is selected for each bandgap combination. A simplified diagram of the calculation method is represented in Figure 3.3

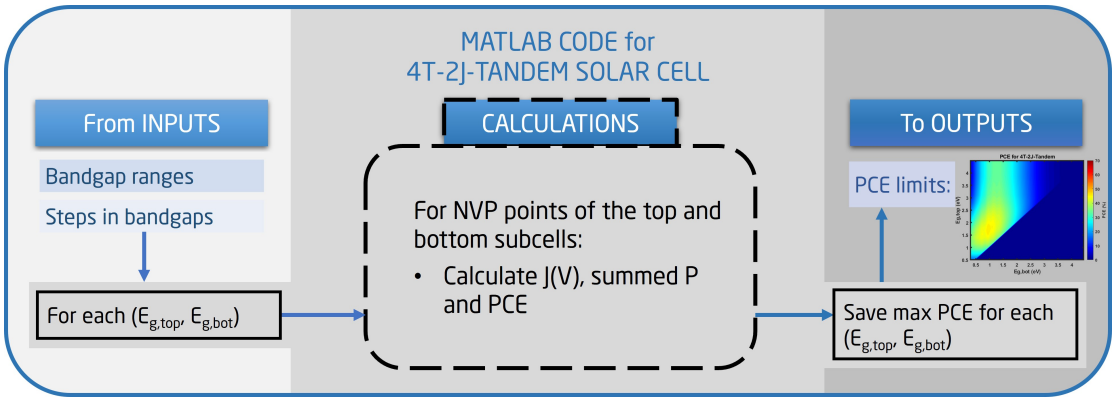

Figure 3.3: Simplified diagram of the calculations based on the detailed balance model for 4T double junction tandem solar cells implemented in MATLAB.

3.1.2.3 2T double junction tandem solar cell

In the 2T double junction tandem there's the added requirement of the current matching of both subcells. For every top and bottom bandgap combination specified in the input (according to the bandgap range and step length stated), the same calculation is employed. The current provided by each of the subcells is calculated for different voltage values, using equation (2.14c) (with the corresponding integration limits) and the same MPP algorithm as described for the SJSC. For every possible value of the current density, the voltages of the subcells are checked, to calculate the total power density provided by the 2T tandem for every value of current density, employing equation (2.17a). Thus, the MPP is selected for each bandgap combination. A simplified diagram of the calculation method is represented in Figure 3.4.

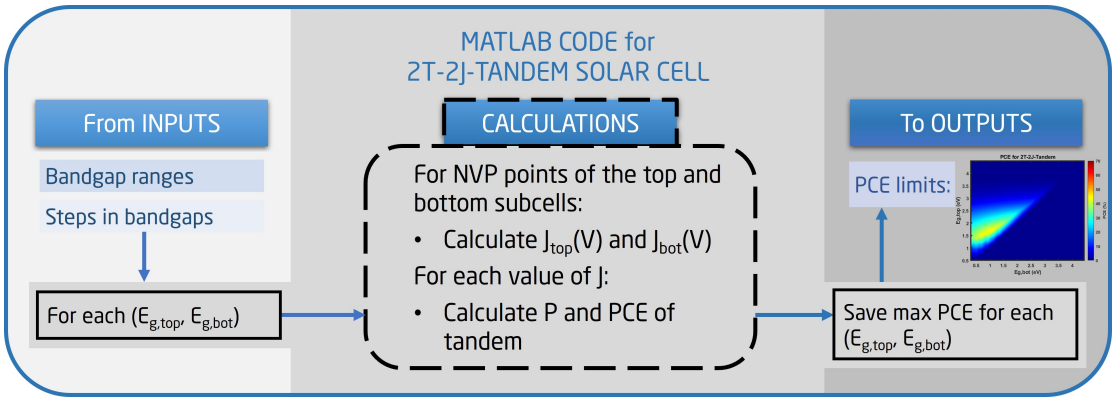

Figure 3.4: Simplified diagram of the calculations based on the detailed balance model for 2T double junction tandem solar cells implemented in MATLAB.

3.1.2.4 IBSC

For the IBSC there's also the requirement of the current matching across the low and high subbandgap. For every main bandgap and low subbandgap combination specified in the input (according to the bandgap range and step length stated), the same calculation is employed. First the current density provided by the IBSC for different voltage values is calculated, using equation (2.14c) and the same MPP algorithm as described for the SJSC. For each voltage value of the main bandgap, the current density provided by the two subcells is calculated at different positions of the quasi-Fermi energy levels, finding the positions that give current matching via a bisection method. The current density provided by the subbandgaps (so-called two-photon subbandgap photocurrent) is added to that generated by the main bandgap. Afterwards, the power density provided by the IBSC for different voltage values is calculated, employing equation (2.19a). Thus, the MPP is selected for each combination of main bandgap and low subbandgap. A simplified diagram of the calculation algorithm represented in Figure 3.5.

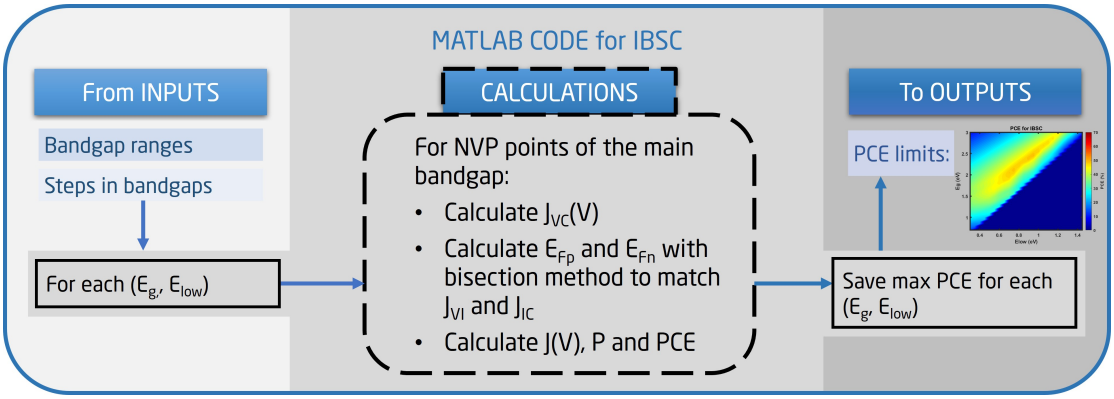

Figure 3.5: Simplified diagram of the calculations based on the detailed balance model for IBSCs implemented in MATLAB.

3.1.3 Output

The program developed by Linge provides a variety of results that can be analyzed for all the solar cell types considered.[71] First, the maximum PCE limit achievable with each studied bandgap or bandgap combination can be plotted. This gives a 2D diagram with an efficiency curve (PCE vs E_g) in case of the single junction cell, while for the rest of the cell types it is a 3D diagram with an efficiency surface (PCE vs E_{g1} and E_{g2}), as shown in Figure 3.6a. It is also possible to perform a sensitivity analysis, displaying the bandgap range that gives 90% of the maximum efficiency, as represented in Figure 3.6a. Finally, as a V sweep MPPT method has been employed for each bandgap or bandgap combination, the current density and voltage values can be employed to show the JV curve of the solar cell in question for a specific bandgap or bandgap combination, as seen in Figure 3.6b.

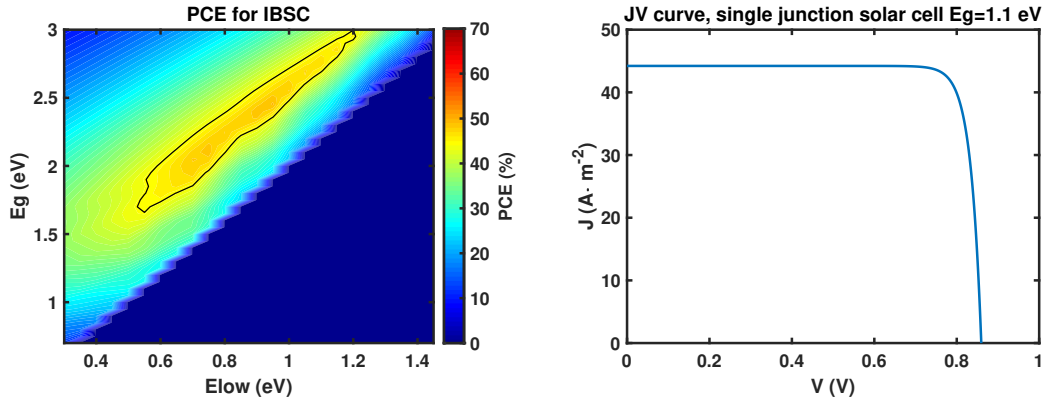

(a) (b)

Figure 3.6: (a) Maximum PCE limit surface for different (E_g, E_{low}) combinations of an IBSC, with a black contour line indicating combinations with 90% of the maximum PCE. (b) JV curve of a single junction solar cell with 1.1 eV.

3.2 PYTHON Code

Dr. Pearce et al. have published the Python code they developed for the ECoPV project on Github.[55] This presents many capabilities involving the calculation of the efficiency of coloured 2T tandem solar cells. For the purpose of this project the most relevant feature of the code is the optimization of the bandgaps and the reflectance spectra of series connected multijunction solar cells, in order to find the maximum PCE achievable with a n-junction 2T tandem cell and a specific colour. As done for the MATLAB code, this section presents the input of the Python code, the calculations it performs, and the output provided. The explanation that follows is meant for the part of the code that optimizes both the bandgaps of the solar cell and the reflectance spectrum at the same time, even though the program developed in the ECoPV offers other posibilities.

3.2.1 Input

The code requires many inputs related to the modeled solar cell, the optimized reflectance spectra, and the optimization method. One can choose the number of junctions of the series connected tandem. The incident light for efficiency calculations is ASTM G173-03 (2008) AM1.5G by default, and the visible energy range considered for calculations related to colours is 380-780 nm. One must define the xyY coordinate values of the target colour of the solar cell, and the shape of the optimized reflectance spectra (rectangular or Gaussian peaks, with fixed or variable height, the number of peaks, and the baseline of the reflectance). There's also the possibility of optimizing a black cell, in which case the reflectance spectra is set to 0. The code by default makes the calculation for the 24 colours of the Macbeth ColorChecker Color Rendition Chart, with a reflectance spectrum formed by 2 rectangular peaks of height 1 in some parts of the VIS, and baseline 0 for the

rest of wavelengths.[72] Another parameter to define is the resolution in wavelength for the spectral calculations (0.1 nm by default). Regarding the optimization, as briefly explained later, the code uses a Multi-Objective Evolutionary Algorithm based on Decomposition (MOEAD), and the parameters for this algorithm have to be defined.

3.2.2 Calculations

In this section, the calculations performed by the program developed by Dr. Pearce et al. are presented, separated into three main parts: i) the calculation of the maximum PCE with a certain bandgap combination and reflectance spectrum, ii) the generation of reflectance spectra, and iii) the evolutionary algorithm used for optimization.

3.2.2.1 Maximum PCE

For a given bandgap combination of the n junctions of the tandem and a certain reflectance spectrum, the code calculates the maximum power density achievable applying some assumptions and simplifications to the detailed balance analysis. The starting point are the detailed balance equations for the generated and lost current densities, with reflectance incorporated, introduced in Section 2.4.4.3. In the current section, the equations employed for the SJSC will be introduced initially, later to broaden it to 2T n-junction tandem cells.

First, for the current loss due to radiative recombination and for the current gained due to absorption of ambient radiation, the Boltzmann approximation is applied. As explained before, this applies when the energy of the transitions considered is much higher than the thermal energy ($E - qV >> k_BT$). So, the expressions in equations (2.28b) and (2.28c) are approximated to those shown in equations (3.1a) and (3.1b).

$$J_{amb} \sim q\frac{2\pi}{h^3c^2}\int_{E_g}^{\infty}(1-R(E))E^2e^{\frac{-E}{k_BT_c}}dE \tag{3.1a}$$

$$J_{rad} \sim q\frac{2\pi}{h^3c^2}e^{\frac{\Delta\mu}{k_BT_c}}\int_{E_g}^{\infty}(1-R(E))E^2e^{\frac{-E}{k_BT_c}}dE \tag{3.1b}$$

It must be stated here that the original code posted by Dr. Phoebe et al. does not consider the effect of reflectance in the current generation by absorption of thermal ambient radiation and in the current loss due to radiative recombination, so that the previous expressions are modified, as seen in equations (3.2a) and (3.2b).

$$J_{amb} \sim q\frac{2\pi}{h^3c^2}\int_{E_g}^{\infty} E^2 e^{\frac{-E}{k_B T_c}} dE \tag{3.2a}$$

$$J_{rad} \sim q\frac{2\pi}{h^3c^2} e^{\frac{qV}{k_B T_c}} \int_{E_g}^{\infty} E^2 e^{\frac{-E}{k_B T_c}} dE \tag{3.2b}$$

Instead of performing the integrals, it uses the analytic solution (i.e., the indefinite integral or antiderivative), as shown in equations (3.3a) and (3.3b). If the reflectance is included and it has rectangular shape, just changing the limits of the integration is enough, in order to integrate along the energies where the reflectance is not 1 (as proposed by Phoebe et al. for the correction of their original code).

$$J_{amb} \sim q\frac{2\pi}{h^3c^2} \cdot k_B T_c e^{\frac{-E_g}{k_B T_c}} (E_g^2 + 2E_g k_B T_c + 2(k_B T_c)^2) \tag{3.3a}$$

$$J_{rad} \sim q\frac{2\pi}{h^3c^2} e^{\frac{qV}{k_B T_c}} \cdot k_B T_c e^{\frac{-E_g}{k_B T_c}} (E_g^2 + 2E_g k_B T_c + 2(k_B T_c)^2) \tag{3.3b}$$

Regarding the current generation due to absorption of sunlight, the code performs a discrete summation of the AM1.5G spectrum, starting from the wavelength corresponding to the bandgap energy, down to 280 nm (below that wavelength there are nearly no photons to absorb according to the ASTM G173-03 (2008) standard), excluding those wavelengths where the reflectance is 1. The summation is performed with the wavelength step ($\Delta\lambda$) defined in the input, as seen in equation (3.4).

$$J_L = \sum_{\lambda=280nm}^{\lambda_{E_g}} b_s(\lambda) \cdot (1 - R(\lambda)) \cdot \Delta\lambda \tag{3.4}$$

Then, the current provided by the cell is calculated with equation (3.5).

$$J(V) = J_L + J_{amb} - J_{rad} = J_L - J_0(e^{\frac{qV}{k_B T_c}} - 1) \tag{3.5a}$$

$$J_0 = q\frac{2\pi}{h^3c^2} \cdot k_B T_c e^{\frac{-E_g}{k_B T_c}} (E_g^2 + 2E_g k_B T_c + 2(k_B T_c)^2) \tag{3.5b}$$

In order to find the MPP of the solar cell, the analytic formula to find the MPP voltage (V_{MPP}) of SJSCs is employed, which is presented in equation (3.6a), with $\Re W$ representing the real part of the Lambert W function. This derives from the

expressions for the current and the power of the solar cell (equations (3.5a) and (2.15)), explained in detail in reference [73].

$$V_{MPP} = \frac{k_B T_c}{q} ln \left[\Re \left(W \left(e \frac{J_L + J_0}{J_0} \right) \right) - 1 \right] \tag{3.6a}$$

$$Y = X e^X \Leftrightarrow X = W(Y) \tag{3.6b}$$

The program then calculates the current and the power at the MPP, with equations (3.7) and (3.8), as well as the efficiency of the solar cell (employing equation (2.8)).

$$J_{MPP} = J_L - J_0 (e^{\frac{qV_{MPP}}{k_B T_c}} - 1) \tag{3.7}$$

$$P_{MPP} = J_{MPP} \cdot V_{MPP} \tag{3.8}$$

Tandem cells

When it comes to series connected 2T n-junction tandem cells in the ECoPV program, the maximum PCE calculation is similar to the case of the SJSC. In the computation of the currents (equations (3.2a), (3.2b) and (3.4)) the integration and summation limits are changed, so that each bandgap only absorbs and emits in its corresponding energy range.

The biggest change is in the MPP calculation. First, the V_{MPP} and J_{MPP} for each subcell are calculated independently (using equations (3.6a) and (3.7)). Then it is assumed that the current at the MPP of the tandem is the same as the smallest J_{MPP} of the individual subcells ($J_{MPP,\,min}$). They base this assumption on a previous publication by Pusch et al., where it is stated that: "This approximation works well close to current matching but it becomes worse away from current matching where it becomes possible to increase the overall efficiency of the cell by increasing the current in the limiting junction".[74]

Then the voltage of the n subcells $V_{MPP,\,i}$ is recalculated based on equation (3.5a), where the voltage is isolated, as seen in equation (3.9).

$$V_{MPP,\,i} = \frac{k_B T_c}{q} ln \left(\frac{J_{L,\,i} - J_{MPP,\,min}}{J_{0,\,i}} + 1 \right) \tag{3.9}$$

Thus, the voltage and the power of the tandem at the MPP can be finally calculated, with the expressions shown in equations (3.10) and (3.11).

$$V_{MPP,\,Tandem} = \sum_{i=1}^{n} V_{MPP,\,i} \tag{3.10}$$

$$P_{MPP,\,Tandem} = J_{MPP,\,min} V_{MPP,\,Tandem} \tag{3.11}$$

3.2.2.2 Optimized reflectance spectra

Apart from the bandgap combination, it is necessary to optimize the reflectance spectrum of the solar cell, so that it has the specific colour targeted and at the same time achieves the maximum PCE possible. Due to the aforementioned metamerism phenomenon, there is more than one reflectance spectrum that can give the same colour perception under certain illumination. Therefore, the shape of the reflectance spectrum is another factor to consider in the optimization.

By default, the ECoPV program includes a 24 colour palette, which is the Macbeth ColorChecker chart (see Figure 3.7).[72] Their xyY coordinates are presented in Table 3.1, as reported in reference [75]. These are converted to XYZ tristimulus values by the program, considering D50 as illuminant.

Figure 3.7: Representation of the colours of the Macbeth ColorChecker chart. The xyY coordinates from [75] have been transformed to XYZ and to sRGB employing CIE D50 as illuminant. The colours displayed in the screen are produced based on the sRGB coordinates.

Under a certain illuminant, there are many reflectance spectra that could provide the desired XYZ coordinates. As reported in the work by Halme et al., the

Table 3.1: The CIE xyY coordinates of the 24 colours of the Macbeth ColorChecker chart under D50 illuminant, reproduced from the "BabelColor Avg." xyY data from [75].

Colour name	**x**	**y**	**Y**
dark skin	0.4336	0.3787	0.1029
light skin	0.4187	0.3749	0.354
blue sky	0.2757	0.2996	0.1849
foliage	0.3688	0.4501	0.1329
blue flower	0.3016	0.2871	0.2328
bluish green	0.2856	0.3905	0.4175
orange	0.5291	0.4081	0.3106
purplish blue	0.2335	0.2157	0.1136
moderate red	0.5002	0.3295	0.1989
purple	0.3316	0.2544	0.0639
yellow green	0.3986	0.5002	0.444
orange yellow	0.496	0.4426	0.436
blue	0.2042	0.1676	0.057
green	0.3262	0.504	0.2297
red	0.5734	0.3284	0.1262
yellow	0.4693	0.473	0.6072
magenta	0.4175	0.2702	0.1998
cyan	0.2146	0.3028	0.1889
white 9.5	0.3486	0.3625	0.9094
neutral 8	0.3451	0.3593	0.585
neutral 6.5	0.3447	0.3588	0.3571
neutral 5	0.3433	0.3586	0.1912
neutral 3.5	0.3425	0.3577	0.0887
black 2	0.3436	0.3562	0.0317

most efficient reflectance spectrum for a coloured single junction solar cell has two rectangular 100% reflectance bands, centered around the maximum points of the $\bar{x}(\lambda)$, $\bar{y}(\lambda)$, and $\bar{z}(\lambda)$ CMFs, with 0 reflectance in the rest of the wavelengths.[20] The position and width of the reflectance bands vary depending on the target colour (see Figure 3.8). In this way, the loss of incident photons for colour stimulation is minimum, maximizing the photocurrent. Actually, two reflectance bands are enough to render any colours achievable under AM1.5G illumination.[20] This is due to the colorimetric fact that "any colour can be presented as a linear combination of two monochromatic colours."[20, 65]

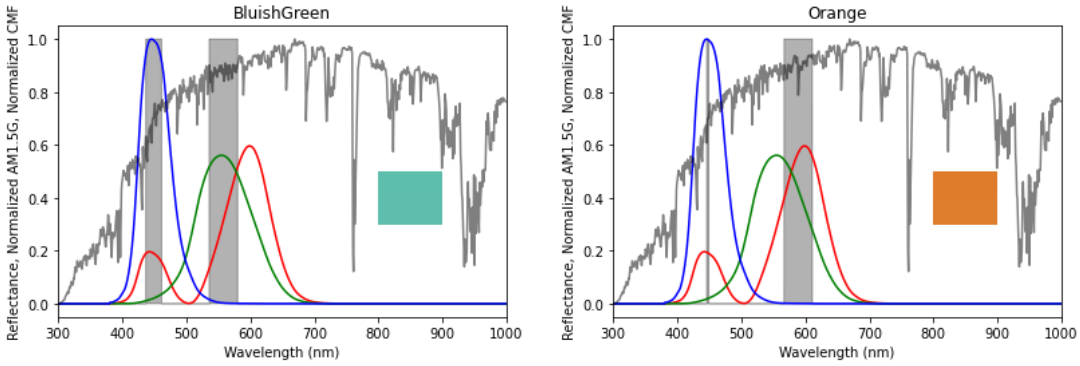

(a) **(b)**

Figure 3.8: Examples of the optimized reflectance spectra output by the ECoPV program for SJSCs: a) Bluish Green, and b) Orange. The reflectance spectra are shown as grey bands. In addition, the normalized CMFs (red $\bar{x}$, green $\bar{y}$, blue $\bar{z}$, normalized to the maximum of $\bar{z}$) and the normalized AM1.5G spectral irradiance (dark grey line) are shown.

So, the ECoPV program has the capability of generating optimized reflectance spectra, with two 100% reflectance bands and 0% baseline, so that the maximum PCE for a SJSC with a certain colour appearance can be calculated. The program offers other capabilities, such as: increasing the number of reflectance bands, varying their reflectance value and the value of the baseline, or optimizing for other reflectance peak shapes, such as Gaussian peaks. However, during this thesis the reflectance spectra considered will consist on the default two 100% reflectance bands, with 0% baseline.

Once an optimal reflectance spectrum is generated to render a certain colour, its XYZ tristimulus values are calculated, employing equation (2.20). The ECoPV program developed by Dr. Pearce et al. employs the AM1.5G spectrum as illuminant for this calculation. However, it can be more convenient to calculate the XYZ values of the generated optimum reflectance spectrum with D50 illuminant as reference white. This is because the XYZ values of the optimized spectrum are compared with the XYZ values of the target, so they should have the same illuminant. The relative difference in each of the 3 tristimulus values is calculated, and the highest of the differences is employed to accept the optimized reflectance spectrum as close enough to the target, in case it is below a defined threshold, as shown in equation (3.12).

$$max\left(\frac{\Delta X}{X}, \frac{\Delta Y}{Y}, \frac{\Delta Z}{Z}\right) < \text{Threshold} \tag{3.12}$$

Moreover, the colour difference ΔE_{00} between the optimized colour and the target colour is calculated via equations (2.22) and (2.25). Therefore, it is necessary that the tristimulus values of both colours are based on the same standard illuminant (i.e., D50).

3.2.2.3 Multi-Objective Evolutionary Algorithm based on Decomposition

In the previous two subsections, it has been explained how the ECoPV program calculates the efficiency and the difference to the target colour of a coloured opaque solar cell with a certain bandgap and reflectance spectrum. However, the optimization process of both the bandgap and the reflectance spectrum for each colour has not been discussed yet. The program developed by Dr. Pearce et al. employs a Multi-Objective Evolutionary Algorithm based on Decomposition (MOEAD) for that purpose. The basics of this algorithm will now be introduced based on the optimization problem concerning the thesis, but without going deep into the details of the algorithm, as a proper study of this method could involve a hole thesis in itself. For a more exhaustive explanation, the reader is referred to the work by Zhang et al.[76]

The optimization of coloured solar cells represents a multi-objective optimization problem, because it includes two objectives: the PCE of the solar cell is to be maximized, and the difference between the colour of the solar cell and the target colour has to be minimized. The mathematical formulation of the problem is presented in equation (3.13), where $f_1(\vec{x})$ and $f_2(\vec{x})$ are the objective functions to minimize: the negative of PCE must be minimized, and the colour difference must be minimized. $\vec{x}$ is the decision vector, which consists of all the decision variables, and it must be inside the feasible set of decision vectors X.

$$\min_{\vec{x} \in X}(f_1(\vec{x}), f_2(\vec{x})) \tag{3.13}$$

For the problem in question, the decision variables are the values of the bandgap or bandgaps of the solar cell (depending on if it is a single junction or multibandgap solar cell), and the centers and widths of the reflectance bands. In principle, the variables could take any real positive value, but one can set some boundaries to the centers and widths of the reflectance bands so that they are contained inside the visible region. In a similar fashion, instead of considering all possible positive bandgaps, the ECoPV program limits the bandgap values between 0.5 and 4.0 eV.

The MOEAD provides a pathway to find the values of the decision variables that come close to the minimum of the objective functions. A schematic representation of the algorithm is shown in Figure 3.9. The MOEAD algorithm employed in the ECoPV program consists of an archipelago, formed by a certain number of islands (10, by default). In each of the islands, there is a certain population size, which represents the number of decision vectors contained in the island. Each of the decision vectors in a population of an island is called an individual.

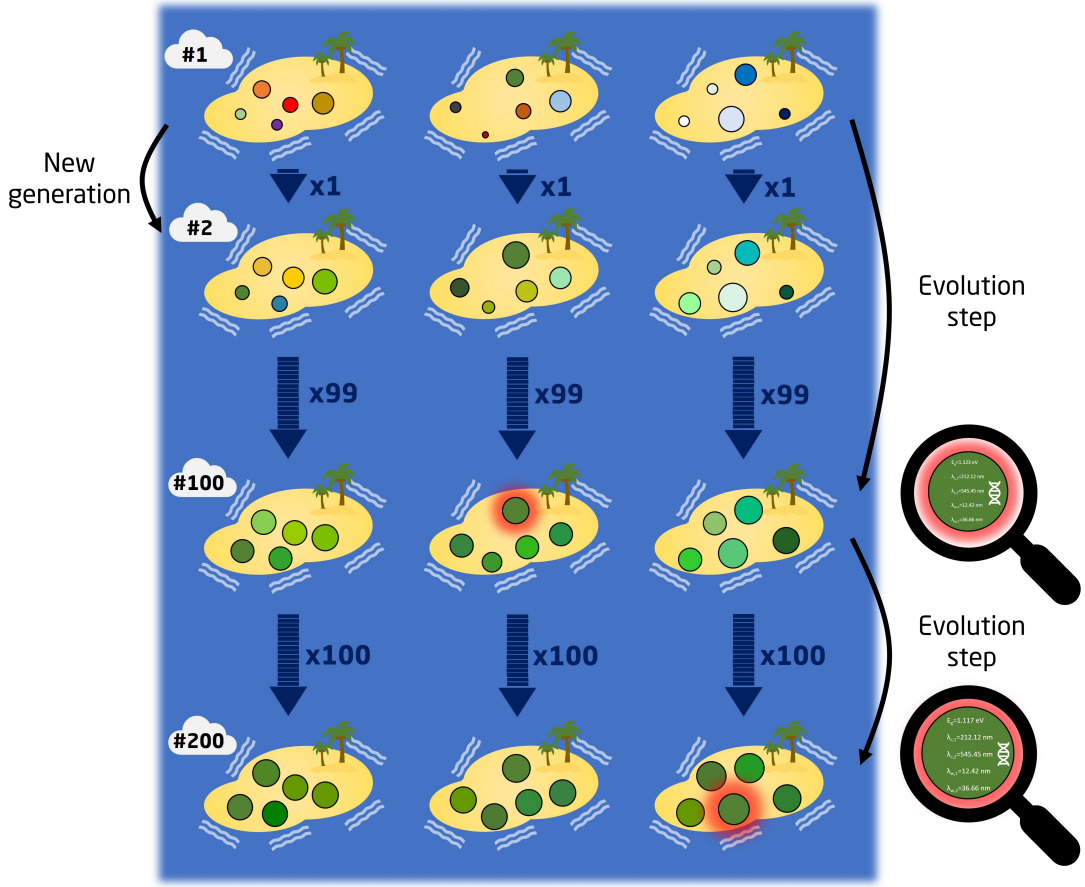

Figure 3.9: Schematic illustration of the MOEAD. The individuals are represented by circles, whose size symbolizes their maximum PCE and whose colour represents the colour obtained with the optimized reflectance spectrum. The objectives in the illustrated optimization are maximizing the PCE and producing a certain green colour.

When the MOEAD is initialized, all the individuals of all the islands are given some decision variable values at random (bandgaps and reflectance band centers and widths), inside the preset boundaries. Then, the fitness of each individual is calculated. This is a numeric value, which indicates how good that individual is as a solution to the optimization problem.

Once the individuals of the populations of the islands are initialized, the evolution steps run. In each evolution step, a certain number of iterations or generations occur. Each new generation of an island is a new population, which is created based on the previous population of that island, by combining the decision variables of the individuals depending on the fitness.

The evolution steps take place in each island independently, which gives the possibility to run the calculations in parallel. After each evolution step (consisting of a certain number of generations), the most fit individual of each island is checked for the values of its optimization functions. The most fit individual of all the islands is compared to the most fit individual of the previous evolution step. If the change in fitness has been bigger than a certain threshold, the evolution has

not converged yet and another evolution step is run. This is repeated until the change in fitness of the best individual is smaller than the preset threshold. In that moment, the MOEAD stops, and it is considered that the bandgap values and reflectance peak centers and widths found are close enough to the optimum of the studied problem.

In short, the populations of the different islands evolve, making the individuals more fit in every generation, improving the bandgap combinations and the reflectance spectra. In every evolution step, it is checked if the evolution has converged or not. Once it converges, the most fit individual and its decision variable values are taken as the solution to the multi-objective optimization problem.

In the explanation of the algorithm, some details have been skipped, for the sake of clarity. For example, one has to choose the weight or the importance of each optimization function in the fitness. Besides, one can decide the amount of variation from generation to generation, and the randomness degree in the creation of each new generation. However, it must be stated that the parameters concerning the MOEAD algorithm have been set the same as the original values of the ECoPV program. The value of all the parameters can be found in the Github repository of the ECoPV project.[55]

As a final note, one should be aware that the detailed balance calculations to find the maximum PCE limit for a certain bandgap combination and reflectance spectrum are performed for every individual of every island, for every generation of every evolution step. Therefore, it is convenient that these calculations can be done in a computationally fast and efficient way, in order to decrease the runtime of the MOEAD.

3.2.3 Output

The program developed by Dr. Pearce et al. offers a variety of possibilities for the calculations to perform and the results to obtain. However, for the work of this thesis, the most important output values of the optimizations are four:

- Maximum PCE limit for a solar cell with the desired colour.
- Bandgap or bandgap combination (depending on the solar cell type) to obtain the maximum PCE limit.
- 100% reflectance peak centers and widths of the solar cell to obtain the maximum PCE limit.
- ΔE_{00} colour difference between the target and the found optimized colour for the maximum PCE limit case.

CHAPTER 4

Results and Discussion

In the development of this thesis, the models and codes developed in previous work have been modified in order to perform detailed balance analysis of coloured opaque SJSCs and IBSCs. This chapter presents and discusses the results obtained during the thesis. The first section collects the results concerning the detailed balance analysis of SJSCs for both black and coloured cells. Then, it moves on into the detailed balance analysis of IBSCs, again starting with the ideal black cell, later to introduce colours in the model. Finally, the chapter concludes by analyzing the difference between the optimum rectangular-like reflectance spectra generated and the reflectance spectrum reported for the MorphoColor PV colouring concept, in terms of the maximum PCE achievable.

4.1 Single Junction Solar Cell

In this section, the results obtained in the simulation of single junction solar cells are presented and discussed. First, the model employed in the detailed balance analysis of the PCE limit of the SJSCs is validated. Different approaches to simplify and accelerate the calculations are also explained, as well as their effect on the accuracy of the PCE values. Second, the results obtained with the model when introducing reflectance are given, depending on how the reflectance is introduced (i.e. in which components of the current density calculation). Finally, the model is employed to calculate the maximum PCE limit, the optimum bandgap and the best reflectance spectrum of solar cells with the colours of the Macbeth ColorChecker chart. Additionally, the repeatability of the optimization method employed is studied.

4.1.1 Validation of the model

To begin with, the detailed balance model implemented for single junction solar cells in Linge's MATLAB program is validated. The maximum PCE achievable for solar cells with bandgaps between 0.3 and 4.5 eV (with 0.01 eV steps) calculated based on the model are compared to the results reported by Rühle et al, as shown in Figure 4.1.[34]

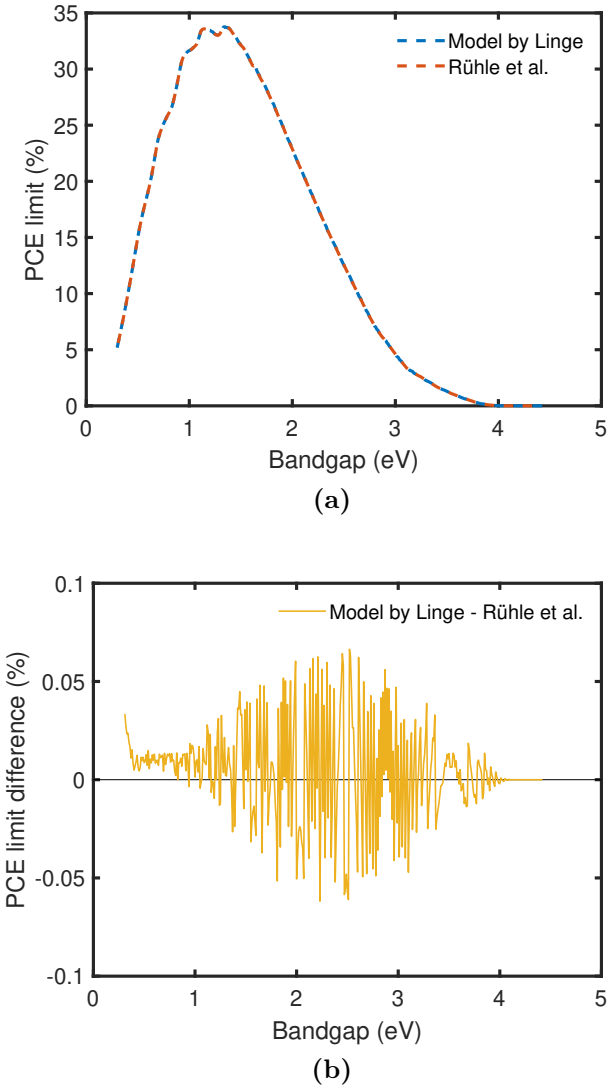

Figure 4.1: (a) Maximum PCE limit calculated with detailed balance model implemented in Linge's program for a SJSC under AM1.5G illumination, for energy gap ranging between 0.3 and 4.5 eV with 0.01 eV steps, and results reported by Rühle et al.[34] (b) Difference between results obtained with Linge's program and the results reported by Rühle et al.

The maximum PCE limits calculated with the detailed balance model in question are the same as those reported in the literature, with an absolute difference smaller than 0.1 % for all bandgap combinations. Therefore, it is concluded that the model is valid for calculating the maximum PCE limit of SJSCs.

4.1.2 Runtime acceleration approaches

The calculation of all the PCE limits from Figure 4.1a with Linge's program takes $75 \pm 4\ s$ (mean and standard deviation of 5 runs with an Intel® Core™ i7-6500U CPU at 2.50GHz). This is a considerably long runtime if the code is to be implemented in the PCE calculation for the optimization function of the MOEAD. As the MOEAD requires running a lot of calculations (for all the individuals in all the islands, for every generation in each evolution step), it is convenient to make the calculation of the maximum PCE achievable with a certain bandgap faster. For example, the ECoPV program developed by Dr. Pearce et al. includes some approximations and simplifications, in order to accelerate the calculations.

In this section, the inclusion of different approximations and simplifications in the code is considered and tested. For that purpose, one has to analyze the original code implemented in Linge's program. For a solar cell with a certain bandgap, it basically calculates the efficiency for different voltage values, with a 500 point voltage sweep MPPT method. For every voltage value, it calculates the photogenerated current due to the absorption of photons from the sun (J_L) and from the ambient (J_{amb}), and the current loss because of radiative recombination (J_{rad}), with equation (2.14c). The former is calculated with a discrete summation of the AM1.5G spectrum, and the latter two by numerical integration.

Table 4.1 lists the approaches tested in this thesis that include approximations and simplifications in the calculation of the maximum PCE limit. Some changes concern the MPPT method (changing the amount of points in the voltage sweep, or using the analytical solution with the Lambert function), and others the calculation of the current generation and loss (applying the Boltzmann approximation, and using the indefinite integral instead of numerically integrating). A name is given to each of the approaches for simplicity in the discussion. The last of the approaches, named "Boltzmann-Lambert", is basically the calculation method used in the ECoPV program developed by Dr. Pearce et al.[55]

Table 4.1: Runtime acceleration approaches tested for detailed balance calculations of SJSCs, with their approximations and simplifications.

Name of approach	J_{rad} **and** J_{amb} **calculation**	**MPPT**
Linge	No Boltzmann approx. (eq. 2.14c)	500 point V sweep
Boltzmann	Boltzmann approx. (eq. 2.16)	500 point V sweep
Boltzmann 5000	Boltzmann approx. (eq. 2.16)	5000 point V sweep
Boltzmann-Lambert	Boltzmann approx. (eq. 3.5)	Analytical solution (eq. 3.6)

Figure 4.2a shows the maximum PCE achievable with solar cells with bandgap between 0.3 and 4.5 eV (with 0.01 eV steps), calculated employing the approaches listed in Table 4.1. In addition, Figure 4.2b displays the difference between the maximum PCE calculated with each approach with respect to the Boltzmann-Lambert approach (because this last one gives the highest value in all the energy range considered). Table 4.2 shows the runtime required to perform the necessary calculations for all the bandgaps considered, for every approach.

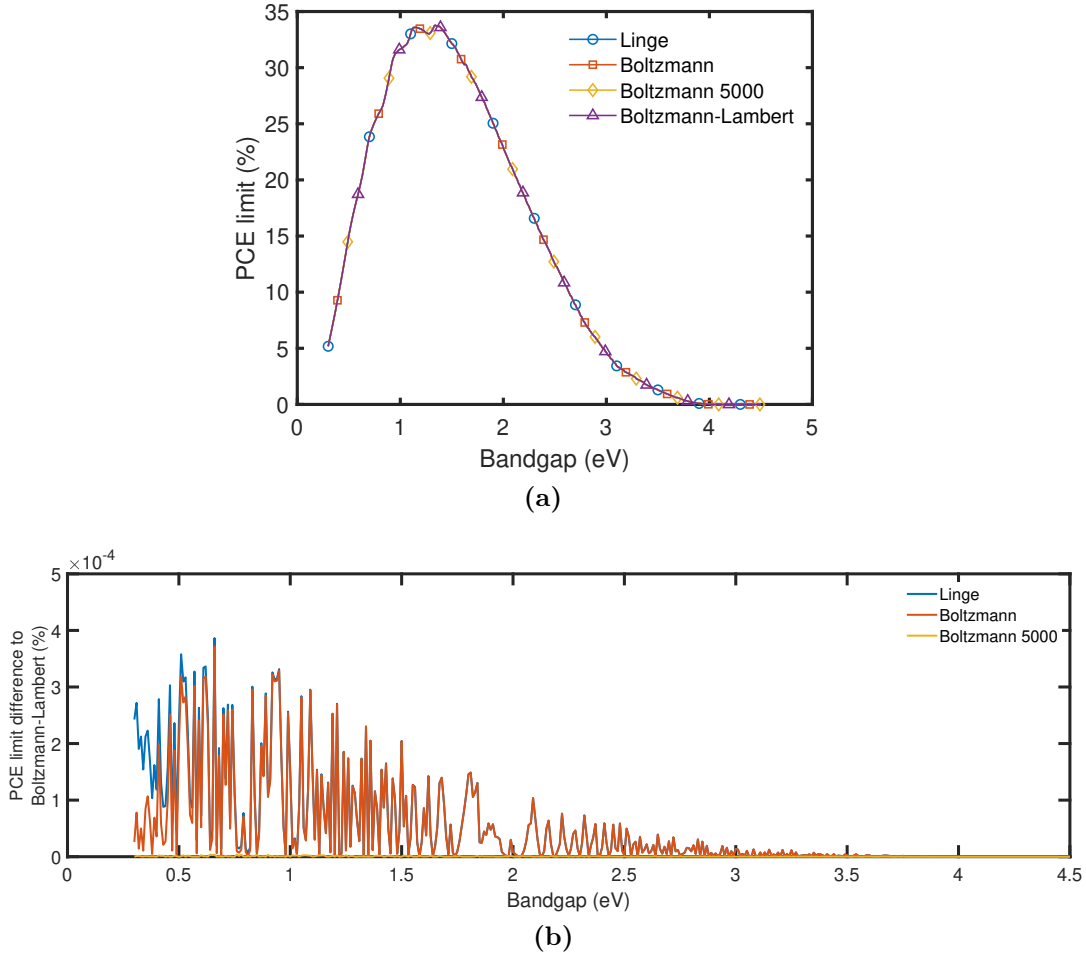

Figure 4.2: (a) Maximum PCE limit calculated with different approaches, for a SJSC under AM1.5G illumination, for energy gap ranging between 0.3 and 4.5 eV with 0.01 eV resolution, and results reported by Rühle et al.[34] (b) Difference in absolute percentage between maximum PCE calculated with first three approaches to the Boltzmann-Lambert approach (this last always gives the highest PCE).

Table 4.2: Runtime of the approaches for computing the PCE limits for energy gaps between 0.3-4.5 eV, with 0.01 eV steps.

Approach	**Runtime* (s)**
Linge	75 ± 4
Boltzmann	0.74 ± 0.04
Boltzmann 5000	2.32 ± 0.18
Boltzmann-Lambert	0.58 ± 0.06

*Average and standard deviation of 5 runs.

Discussion

At plain sight, in Figure 4.2a all of the approaches seem to give the same result for the range of energy gaps studied. The obtained maximum PCE limit corresponds to 33.78%, for an energy gap of 1.34 eV. This almost matches the maximum value of 33.77% for 1.34 eV reported by Rühle et al.[34]

For a thorough comparison of the approaches, Figure 4.2b displays the difference between the maximum PCE calculated with them. First of all, the PCE limit differences between all approaches are below 0.001% for all the energy gaps considered. So, the results reported by Rühle et al. have not been included in this comparison, because the published data only presented 2 decimal numbers.[34]

The deviations in the Linge and Boltzmann approaches present fluctuations (which are always positive, i.e. a lower PCE than with the Boltzmann-Lambert approach). These come from the inaccuracy of their MPPT method. For some bandgap values the 500 point voltage sweep method employed finds the V_{MPP} quite accurately, giving differences of almost 0 to approach "Boltzmann-Lambert", but for some other bandgaps the MPPT algorithm is less accurate. Therefore, the PCE limits found with the first two approaches are always lower. In addition, the fluctuations become bigger for low bandgaps, as finding the accurate voltage value becomes more relevant (because the same absolute error in voltage supposes a larger relative error). The Boltzmann 5000 approach also presents the fluctuations discussed (hardly visible in Figure 4.2b), but as it uses more points in the voltage sweep, it finds the V_{MPP} more accurately.

For low bandgap values in Figure 4.2b the results from the Linge approach start to deviate from approach Boltzmann-Lambert more than the results of the Boltzmann approach. This is due to the fact that in all approaches but Linge's the Boltzmann approximation is applied, assuming $E - qV >> kT$. This assumption becomes less correct for low bandgap values, which explains the deviation in question. It must be stated that the error due to the approximation is very small (in the order of 0.0002%) for the smallest bandgap considered (0.3 eV), which is a very non-optimal bandgap value as well (with around 5% PCE, as observed in Figure 4.2a).

Consequently, all the approaches give practically the same result (as discussed later, the error due to the approximations and simplifications is smaller than the variability of the MOEAD algorithm). However, the time required to perform the calculation with each approach is different, as seen in Table 4.2. Linge's method takes much more time because it calculates the integral in equation (**??** for every voltage value in the MPPT sweep. Applying the Boltzmann approximation accelerates the code, as the voltage gets out of the integral (see equation (2.16a)), reducing the runtime for the rest of approaches. The Boltzmann-Lambert approach is the fastest because it uses the analytic solution of equation (3.6) as MPPT. Besides, it uses the indefinite integral instead of performing numerical integrations.

To sum up, considering that all approaches have almost the same accuracy, one would probably opt for the fastest method for the calculation of PCE limits

of SJSCs. However, as it will be discussed later, when IBSCs are considered, the analytic solution with the Lambert function for MPPT cannot be applied directly, as current and voltage matching across different subbandgaps has to be considered. In the following section, the introduction of the effect of the reflectance in the model for SJSCs is discussed.

4.1.3 Reflectance introduction in the model

As it has been explained in Section 2.4.4.3, the detailed balance model is modified to consider coloured opaque SJSCs, by introducing the reflectance spectrum in the calculation of the different components of the current density (J_L, J_{amb} and J_{rad}), and therefore in the maximum PCE limit computation. In this section, the effect of introducing the reflectance in the model is assessed.

For that purpose, an arbitrary reflectance spectrum is selected, which is shown in Figure 4.3. This consists of no reflectance in all wavelengths, except between 400 nm and 700 nm, where the solar cell is assumed to be perfectly reflecting. As it would reflect almost all the visible light, the solar cell would appear white under daylight illumination.

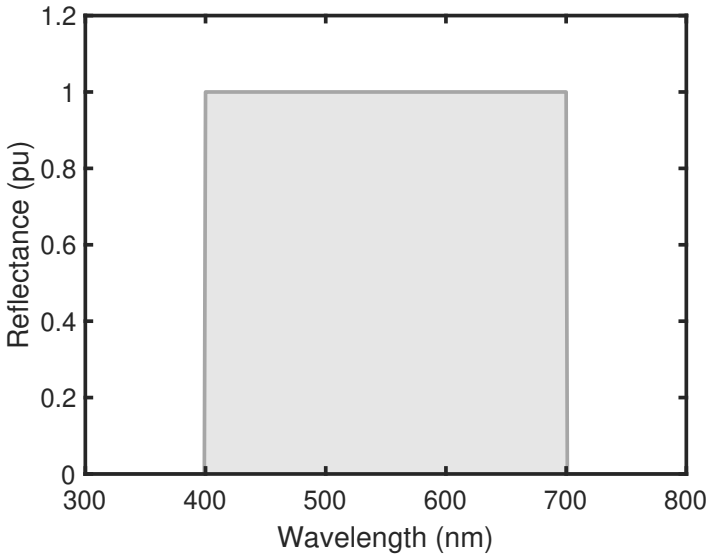

Figure 4.3: Arbitrary reflectance spectrum introduced for initial test of the detailed balance model for SJSCs including colour.

In a similar way to the previous section, there are different approaches or ways to introduce the reflectance in the model. Based on the Boltzmann-Lambert approach of the previous section, Table 4.3 lists three modifications (which are named "submodels") to include reflectance (R) in the calculations. The Sunlight-reflected submodel is included because it was the original one in the code of the ECoPV program, which disregarded the effect of reflectance in the calculation of J_{amb} and J_{rad}. The Absorption-reflected submodel is the same as the Sunlight-reflected one, but it considers the effect of reflectance in the variation of J_{amb}.

Table 4.3: Submodels based on different ways to introduce reflectance in the detailed balance model for SJSCs.

Name of submodel	Modifications to introduce the reflectance
Boltzmann-Lambert	No R introduced (see Table 4.1)
Complete	R introduced in J_L, J_{amb} and J_{rad} (eq. 3.4 and 3.1)
Complete-limited-V	R introduced in J_L, J_{amb} and J_{rad}, but V_{MPP} limited to E_g/q
Sunlight-reflected	R introduced in J_L, but not in J_{amb} and J_{rad} (eq. 3.4 and 3.2)
Absorption-reflected	R introduced in J_L and J_{amb}, but not J_{rad} (eq. 3.4, 3.1a and 3.2b)

Figure 4.4 shows the maximum PCE achievable with SJSCs with bandgap between 0.3 and 4.5 eV (with 0.01 eV steps) and perfect reflectance between 400 and 700 nm, calculated employing the submodels listed in Table 4.3.

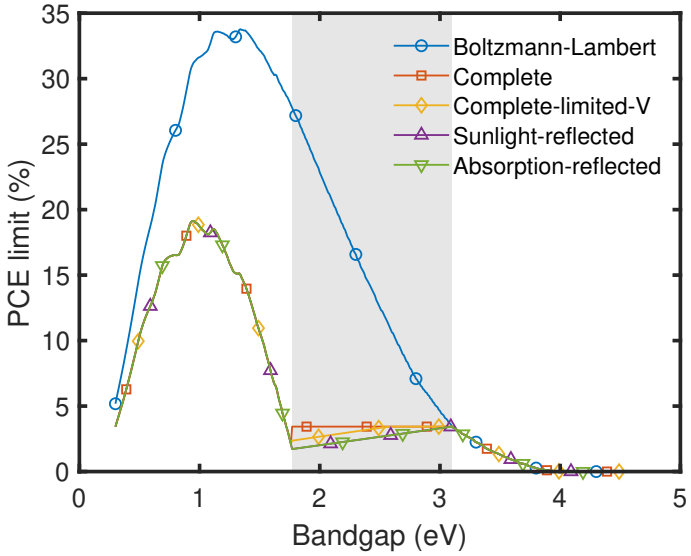

Figure 4.4: Maximum PCE limit calculated with submodels listed in Table 4.3, for a SJSC under AM1.5G illumination, for energy gap ranging between 0.3-4.5 eV with 0.01 eV resolution, with spectral reflectance R=1 between 400-700 nm (energy range shaded in grey).

Discussion

In general, Figure 4.4 shows that the introduction of reflectance lowers the efficiency with respect to the Boltzmann-Lambert submodel. This is mainly caused by absorption of less photons, which decreases both J_L and J_{amb}. The four submodels which include reflectance give the same maximum PCE of 19.13% at 0.95 eV bandgap value.

Their behaviour differs most considerably when the bandgap value is in the visible energy range. The Sunlight-reflected and Absorption-reflected submodels have the lowest PCE, because they do not include the reflectance in J_{rad}, having a higher J_{rad} and lower PCE. As both submodels give exactly the same result,

it is concluded that including reflectance in J_{amb} or not has very little effect, because the contribution of photons from the thermal radiation of the ambient is small. The efficiency of the two submodels discussed increases linearly with the bandgap, because a higher energy gap causes an increase in V_{MPP} without an increase in J_{rad}, and J_L remains constant (as only photons above the VIS range are absorbed). This behaviour is very similar to the reported results for perfectly transparent solar cells in the VIS range by Li et al., as seen in Figure 4.5 for single junction solar cells with 100% average visible transmittance (AVT).[47] In the work by Li et al. the non-absorbing band considered was narrower, from 435 nm to 670 nm, which causes their resulting PCE limits to be higher. In Appendix A the reflectance band is narrowed (435-670 nm) for the Sunlight-reflected submodel, in order to match the work by Li et al., and both plots are compared. This can be considered as validation of the introduction of reflectance in the detailed balance model employed in this thesis.

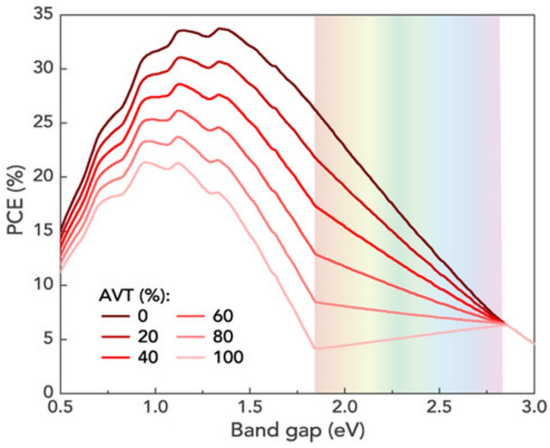

Figure 4.5: PCE limit of single-junction transparent photovoltaics as a function of the bandgap, calculated based on the work by Lunt.[57] Reproduced with permission from [47].

.

The "Complete" submodel has a step-like shape when the energy gap considered reaches the reflectance band, in Figure 4.4. From that point on, the maximum PCE limit remains constant until the bandgap increases beyond the reflectance band. The V_{MPP} value for all those bandgap values with constant PCE limit is invariable as well, with a value of 2.60 V. This can be surprising at first, because it is even higher than the bandgap energy for some considered cases.

The explanation behind this behaviour is on the introduction of reflectance, not only in the absorption of photons from the sun (J_L) and the ambient (J_{amb}), but also in the emission of photons due to radiative recombination (J_{rad}). Basically, the cell has no loss due to emission of photons with wavelength between 400 and 700 nm, because they are reflected back to the inside. This is an effect that could hypothetically be observed in an ideal solar cell, which would fulfil the assumptions of the detailed balance model (specially the fact that the only carrier loss mechanism is radiative recombination) and would have perfect reflectance in the considered wavelength range. The V_{MPP} has a constant value of 2.60 V. Above

that, the voltage gets close enough to the equivalent in energy for 400 nm, and it would cause a bigger loss by increasing emission of UV photons ($\lambda < 400nm$), than the gain in power due to a higher voltage. This is illustrated in Figure 4.6, which displays how the different components of the current density (J_L, J_{amb} and J_{rad}), the total current density (J) and the power density provided by the cell (P) vary with the voltage, for single junction solar cells with 2 eV and 3 eV bandgap, according to the "Complete" submodel. For both bandgap values the JV and PV characteritic diagrams are the same, and the MPP is limited by the sharp exponential increase in J_{rad} when the voltage gets close enough (higher than 2.6 V) to the equivalent in energy of the 400 nm edge of the reflection band ($3.1V$).

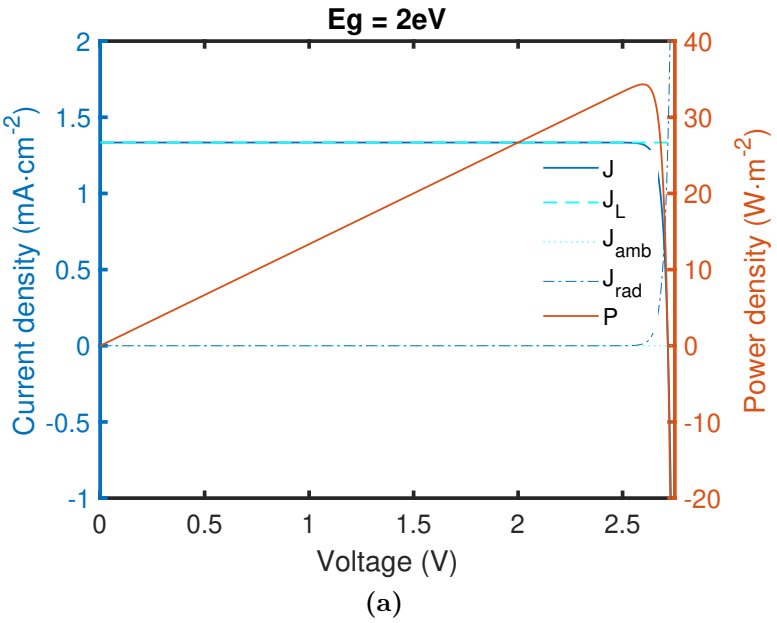

Figure 4.6: JV and PV characteristic of detailed balance model for SJSC with reflectance R=1 in 400-700 nm, for different bandgap values: (a) $E_g = 2eV$ and (b) $E_g = 3eV$.

Finally, looking back into Figure 4.4, the Complete-limited-V submodel has a similar behaviour to the Complete submodel, but the PCE in the low energy range of the VIS is lower, as the V_{MPP} is limited to the bandgap value.

So, the Complete submodel has been selected to introduce the reflectance and perform the optimizations in the next section. Even though the Sunlight-reflected submodel follows the reported results for completely transparent solar cells reported in the literature, it does not consider the effect of reflectance in J_{amb} and J_{rad}. Therefore, the reflectance has been included as explained for the Complete submodel, in the Boltzmann-Lambert approach of the detailed balance model. This combination is employed in the following section, were it has been applied to calculate the maximum PCE limit achievable of SJSCs with the colours of the Macbeth ColorChecker chart.

4.1.4 Application to Macbeth ColorChecker chart

Taking into account the knowledge acquired from the previous sections, the ECoPV program has been employed to calculate the maximum PCE limit of coloured opaque single junction solar cells. Particularly, the 24 colours of the Macbeth ColourChecker chart have been studied. For that purpose, the PCE calculation has been performed with the Boltzmann-Lambert approach (see Table 4.1) but with 0.1 nm intervals in discrete summations (as set by default in the ECoPV program), and the ECoPV code has been changed to introduce the reflectance in all the components of the current (J_L, J_{amb} and J_{rad}, as in the Complete submodel).

The results obtained with the MOEAD optimization algorithm are presented in the following figures. Figure 4.7a displays the target colour and the found optimized colour, whose XYZ tristimulus values have been calculated from the xyY coordinates and the reflectance spectrum, respectively, using D50 as standard illuminant. Then, the XYZ values have been transformed into sRGB, in order to display it on the screen. In contrast, Figure 4.7b gives the ΔE_{00} colour difference value between the target colour and the found optimized colour.

Figure 4.8a shows the maximum PCE limit achievable with each colour. The efficiency change as a function of the relative luminosity (Y) of the colour is also plotted (Figure 4.8b), as well as the the relative power loss (P_{loss}) with respect to 33.78 % (limit for an ideal black solar cell) depending on Y (Figure 4.8c). Figures 4.9a and 4.9b show the bandgap necessary to achieve the maximum efficiency for each colour and its variation with Y, respectively. Instead of employing the relative luminosity as the free variable, Figure 4.10 shows the variation of the PCE limit, the relative power density loss, and the optimal bandgap value, as a function of the perceptual lightness (L^*). Finally, the optimized reflectance spectrum for each colour is schematically represented in Figure 4.11, by indicating with colour stripes the position of the reflectance bands.

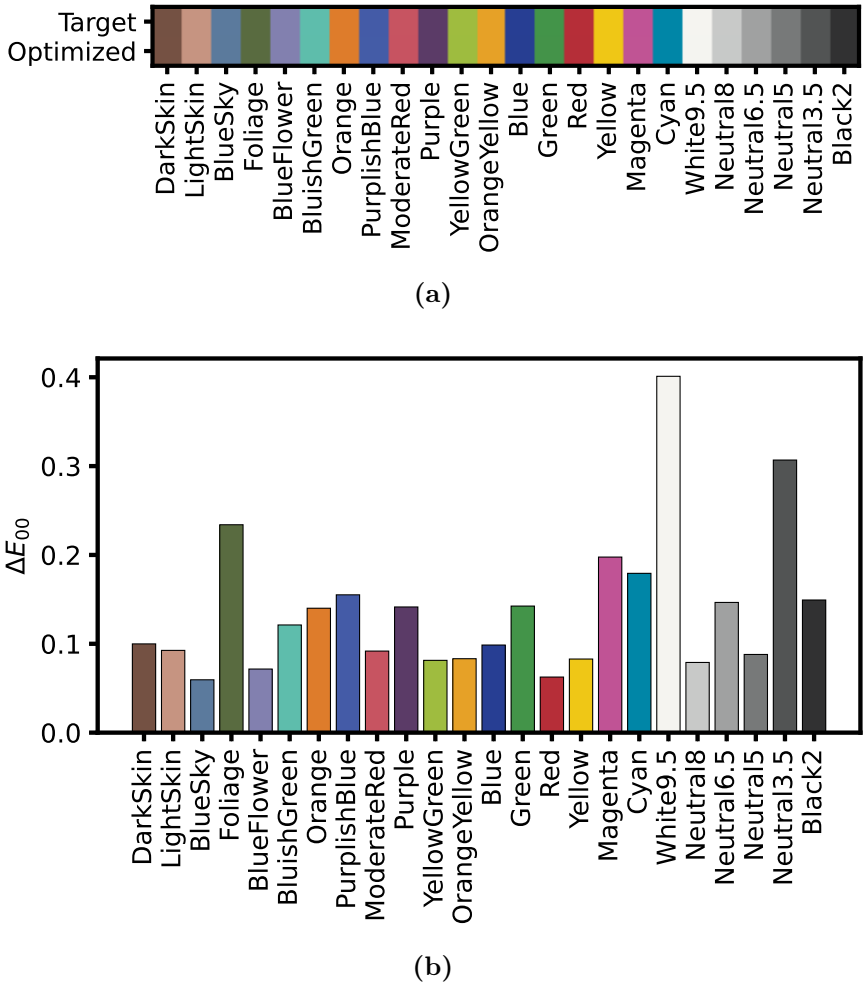

Figure 4.7: (a) Target (top half of rectangles) and optimized (bottom half) colours of the Macbeth ColorChecker chart, displayed based on their sRGB coordinates with D50 as illuminant. (b) ΔE_{00} between target and optimized colour, with D50 as illuminant.

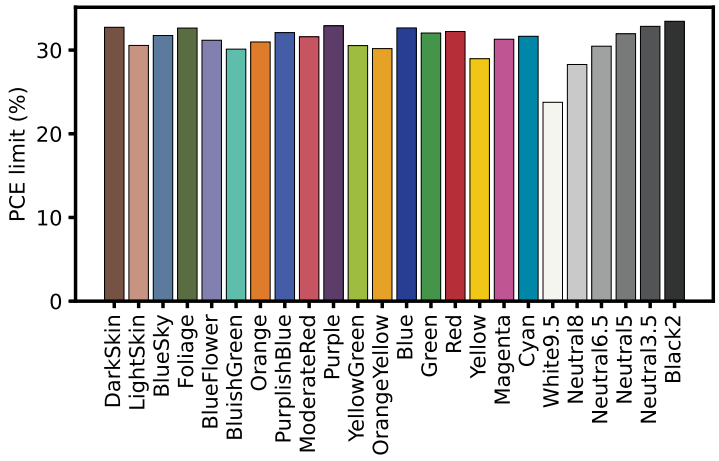

(a)

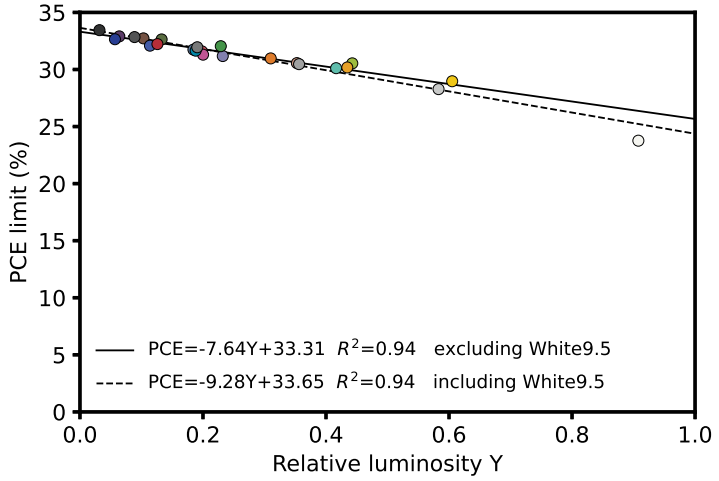

(b)

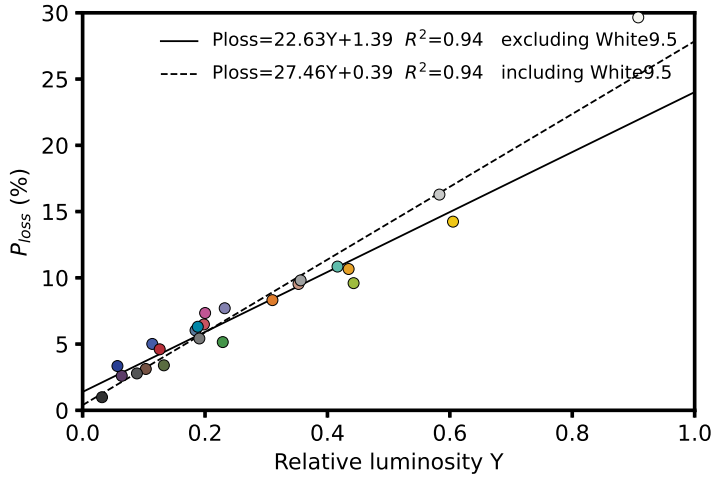

(c)

Figure 4.8: (a) PCE limit of optimized coloured SJSCs with colours of the Macbeth ColorChecker chart. (b) Obtained PCE limit and (c) P loss with respect to the optimal black cell, both as as a function of relative luminosity Y (the linear regressions excluding and including the White9.5 data point are shown).

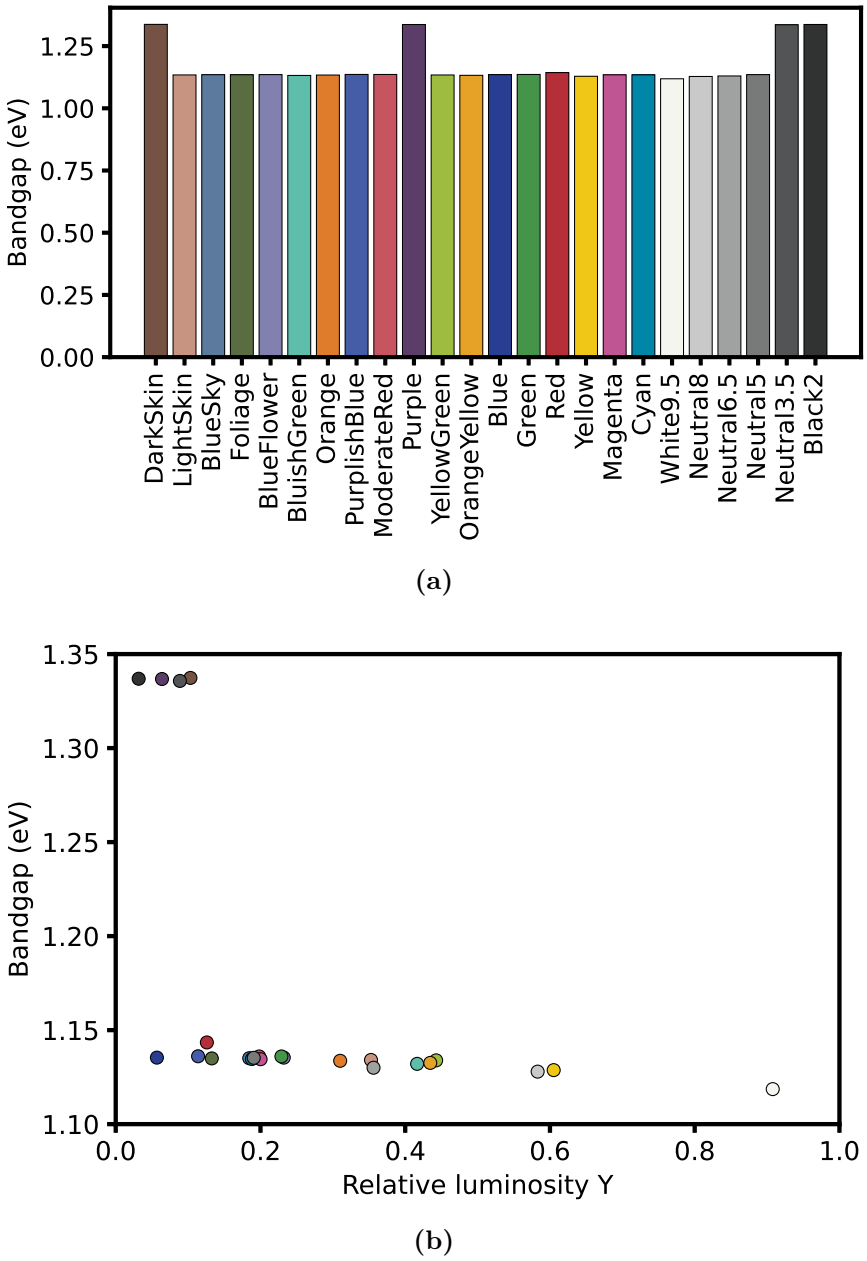

Figure 4.9: (a) Optimal bandgap coloured SJSCs with 24 colours of the Macbeth ColorChecker chart. (b) Optimal bandgap as a function of relative luminosity (Y).

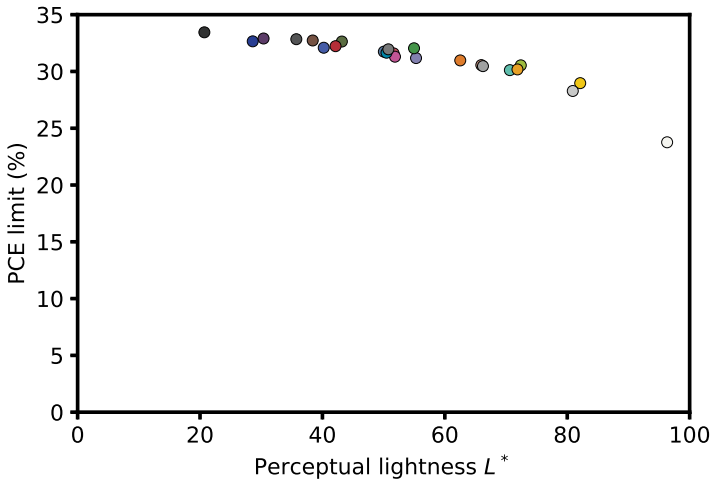

(a)

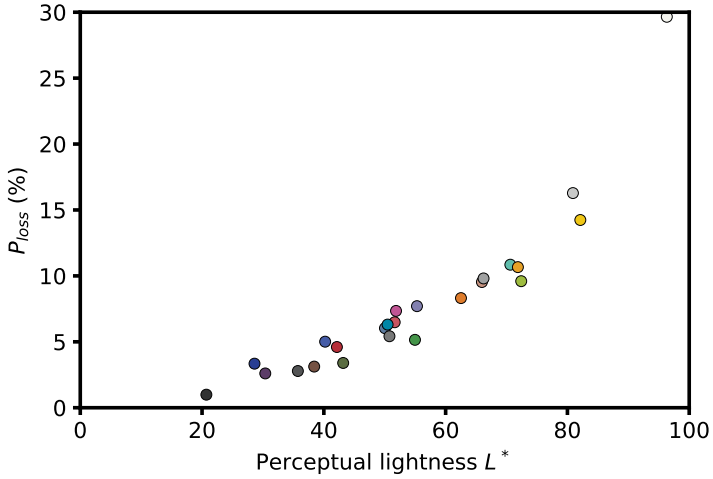

(b)

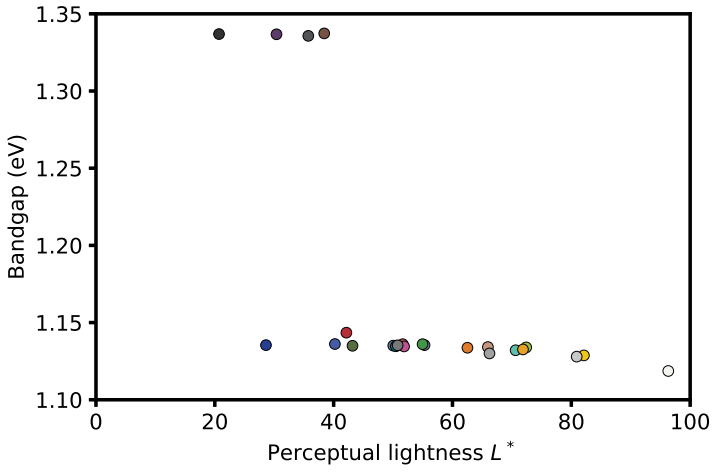

(c)

Figure 4.10: (a) PCE limit, (b) relative power density loss, and (c) optimal bandgap of coloured SJSCs as a function of L^*.

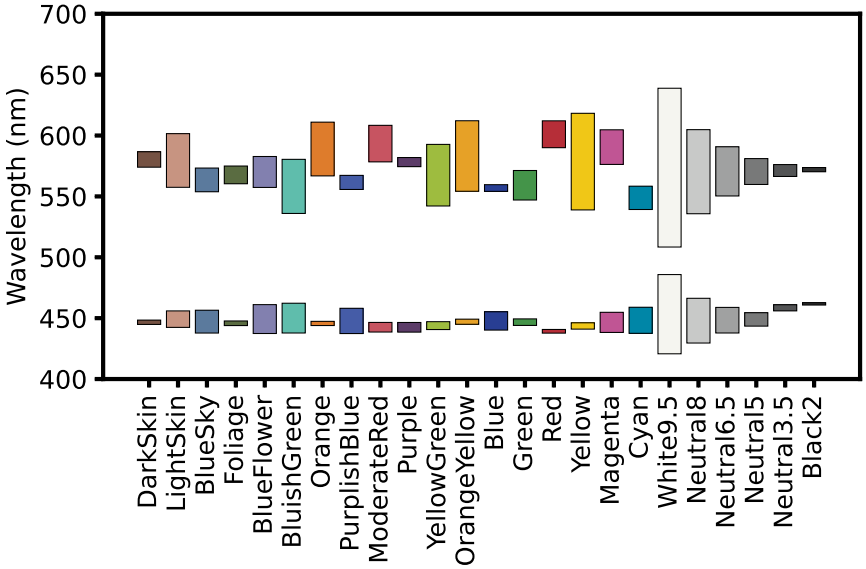

Figure 4.11: Illustration of reflectance spectra of optimized coloured SJSCs: the bar indicates the wavelengths were the reflectance value is 1, while the reflectance is 0 for the rest of wavelengths.

Discussion

In Figure 4.7a, the colour patches displaying the sRGB of the target colour and the optimized reflectance spectra appear indistinguishable. In order to give an objective metric of the colour difference, their ΔE_{00} is given in Figure 4.7b, as a reference for possible comparison with other results that may be reported in the future.

As for the maximum PCE limit, all the considered colours give a lower value than that of the ideal black single junction solar cell. This result was predictable, as colour involves reflection of photons that are not absorbed and are lost for contributing to the power conversion of the incident irradiance. In Figure 4.8b, the efficiency decreases almost linearly with the increasing value of Y, and then drops non-linearly at high Y. The linear regression study of the data points shows how the result for the White9.5 colour does not follow the linear trend. This behaviour was reported by Hanne et al., including the explanation behind it: "The efficiency limits first decrease roughly linearly with Y, then drop non-linearly at higher Y values. This non-linearity comes from the shape of the colour-matching functions: at the lowest relative luminosity limit, the two reflectance bands are narrow and located at wavelengths where the colour matching functions take their highest values at the correct ratio. When Y is increased, the bands widen, which decreases the average value of the colour-matching functions within them, leading to more photons being consumed to generate the same colour chromaticity."[20] However, as explained in Appendix B, the PCE limit values obtained differ slightly from the results reported by Halme et al., because they employed the AM1.5G spectrum to calculate the XYZ tristimulus values out of the optimized reflectance spectra (instead of using the D50 illuminant, which is more convenient to compare to the target colours, as discussed in Section 3.2.2.2).

Additionally, from the dispersion of the results around the linear trend in Figure 4.8b one can reach the conclusion that the PCE limit values depends not only on the Y of the colour, but on other factors as well. Halme et al. saw that the yellow-green colored SJSCs have a higher PCE limit than those with blue-red hue, for the same value of Y.[20] They reached that conclusion by calculating the PCE limit of the colours of the Macbeth ColorChecker chart for varying Y, but keeping the xy chromaticity coordinates, as shown in Figure 4.12. As for the cause of this phenomenon, they suggested that red and blue colours requires some reflectance in the red and blue wavelength regions of the VIS, where photopic sensitivity is lower than in the yellow-green region. In Figure 4.8b, it seems that the colours with yellow-green hue are above the linear regression line, while those with red-blue hue are below. This follows the results by Halme et al.[20]

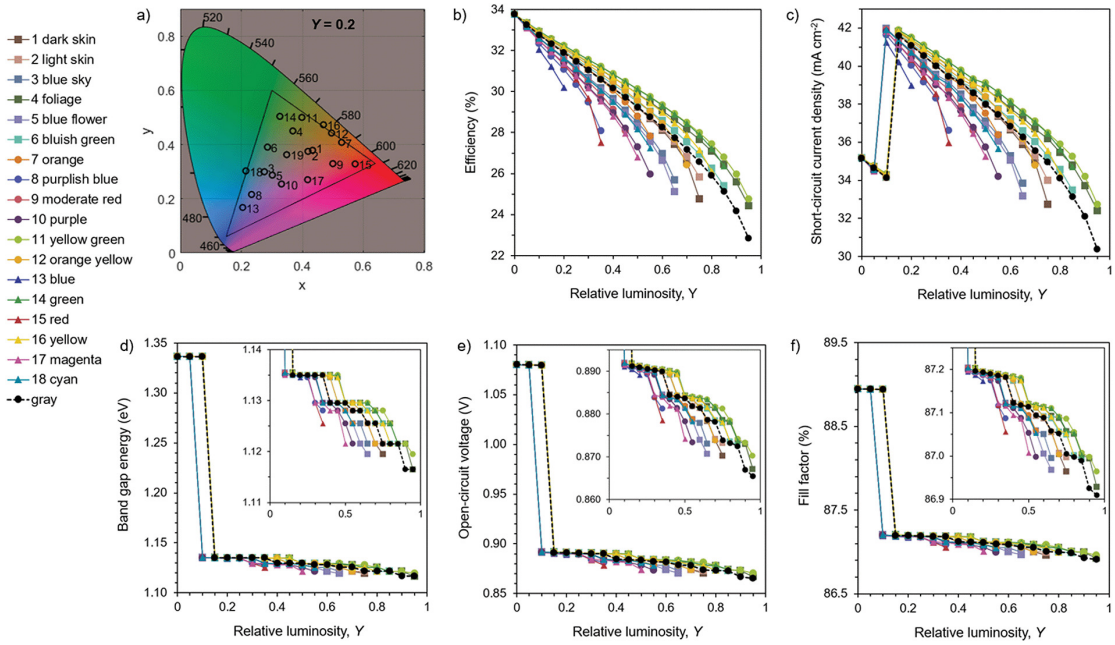

Figure 4.12: Results obtained by Halme et al. for SJCSs with varying Y for the Macbeth ColorChecker chart. The figure shows the effect of colour brightness (relative luminosity, Y) on the theoretical efficiency limits (b), optimal band-gap energy (d), and current–voltage characteristics (c, e and f) for 19 example colours distributed in the CIE chromaticity diagram as shown in panel (a). The relative luminosity Y was varied between 0 and 0.95 in 0.05 steps. Only colours that were produced with a relative error less than 0.5% are shown. Reproduced with permission from [20].

The power loss with respect to the ideal black cell follows the inverse trend. As the efficiencies presented in Figure 4.8b refer to idealistic solar cells, the relative power loss presented in Figure 4.8c may be more relevant for real solar cells, which will have considerably lower efficiencies for both the black and the colored devices. That is, it gives an idea about the minimum (best case) efficiency loss of a "real" coloured solar cell (with rectangular reflectance spectrum), compared to the black device.

Regarding the optimal bandgap values for each colour, it can be seen that they are around 1.13 eV or 1.34 eV. Figure 4.9b shows that ca. 1.34 eV is optimal for colours with low Y, and 1.13 eV eV becomes optimal at higher relative luminosity. There is an exception for the Blue colored solar cell, which has optimal bandgap of 1.13 eV although its Y is low. Again, the same results were reported and explained by Halme et al.[20] They stated that the change in optimal bandgap values is produced by local maxima in the efficiency vs bandgap graph (see Figure 4.1). These are caused by deeps in the AM1.5G spectrum due to atmospheric absorption, starting at around 930 nm and 1100 nm, as shown in Figure 2.1. The high bandgap option (1.34 eV) provides higher V_{oc}, but lower I_{sc}, in comparison with the low bandgap (1.13 eV) alternative, and one or the other turns out to be more efficient, depending on the amount of visible light reflected due to reflection. For low Y, the absorption of more visible light photons favours a higher bandgap, without the need to absorb more in the NIR region. On the contrary, for high Y, the absorption of visible photons is weaker, which favours the 1.13 eV bandgap, absorbing more NIR photons.[20] Besides, the commented exception of the Blue coincides with the results by Halme et al., because they showed that the tendencies with respect to Y depend on the hue too. The colours with red and blue hue tend to switch to a lower (1.13 eV) optimal bandgap at a lower Y, compared to the gray, green and yellow hue (see the results by Halme et al. in Figure 4.12.d).

In Figure 4.10 the dependency of PCE, the relative power loss and the optimal bandgap as a function of the perceptual lightness (L^*) can be seen. The tendency is similar to that against Y, but specially for the PCE and P_{loss} it has a less linear shape. This arises from the cubic relation in the conversion between Y and L^* for most Y values (see equation (2.22)). As suggested before, the PCE follows a linear tendency with respect to Y for low Y values, because the reflectance bands are positioned in the maxima of the CMFs.

Lastly, Figure 4.11 displays the positions of the reflectance bands for each studied colour. The bars mark the wavelength ranges where the solar cell is perfectly reflective ($R = 1$). These are the absolute optimal reflectance spectra for coloured opaque SJSCs, because they consist of rectangular reflectance peaks centered around the maxima of the CMFs, as already explained by Halme et al.[20] Therefore, the optimized reflectance peaks mostly have the same positions, around the maxima of the CMFs. It is interesting to discuss at this point what is the reproducibility of the utilized optimization algorithm. This is the subject of study of the coming section.

4.1.4.1 Repeatability of the optimization algorithm

As the MOEAD has randomness in its algorithm (f.e the starting populations are created randomly), the results obtained in the optimization of a certain coloured opaque SJSC with the employed method vary from run to run. Therefore, the repeatability of the used method is studied here. For that purpose, the Bluish Green colour was selected, because it has some "average" CIExyY coordinates. The same optimization was run from scratch and independently 100 times (with new random initial populations), in order to analyze the repeatability of the results.

The best result obtained has an efficiency of 30.117% for a bandgap of 1.130 eV, and R=1 reflectance bands between 437.4-461.9 nm, and 535.9-580.5 nm (the reflectance spectrum is given in Figure 4.13). Figure 4.14a displays the distribution of the optimized efficiency results, while Figure 4.14b shows the distribution of the optimal bandgaps. On the other hand, the distribution of the optimal reflectance peak edge positions are given in Figure 4.15.

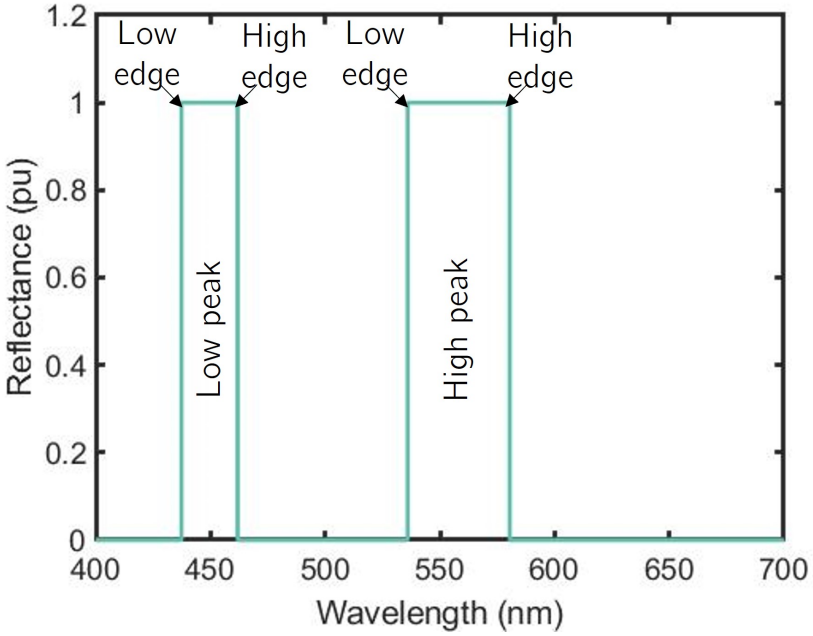

Figure 4.13: Reflectance spectrum of best optimized Bluish Green SJSC out of 100 runs. The labels are indications for Figure 4.15.

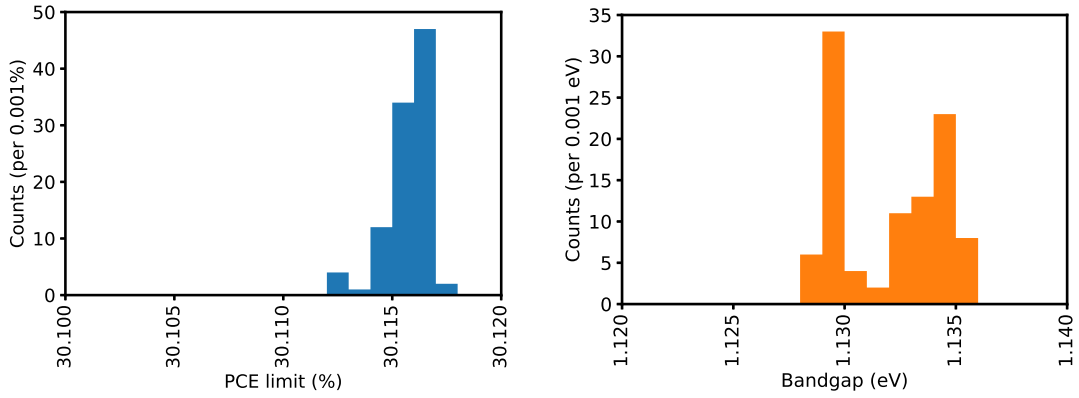

(a) **(b)**

Figure 4.14: Distribution of the results in the 100 optimization runs of the Bluish Green SJSC: (a) PCE limits and (b) optimal bandgaps.

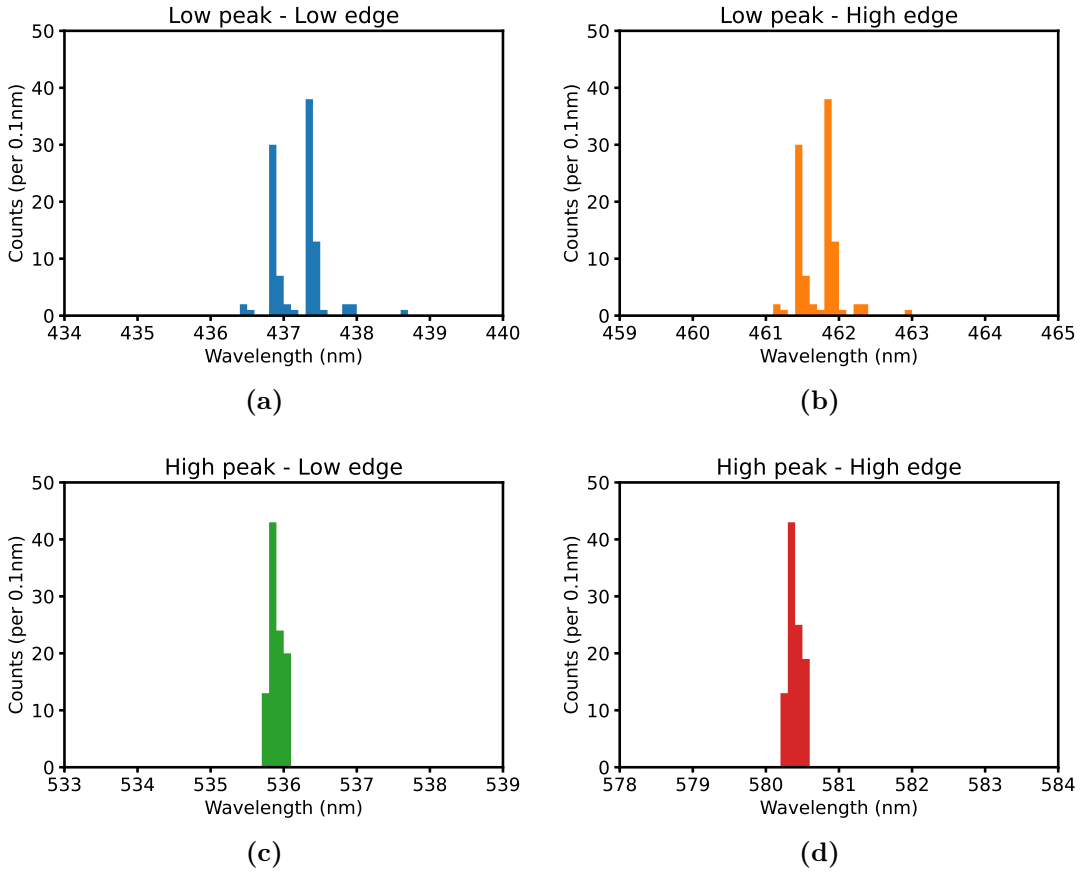

Figure 4.15: Distribution of the reflectance band edge positions in the 100 optimization runs of the Bluish Green single junction solar cell: (a) Low edge of low peak, (b) High edge of low peak, (c) Low edge of high peak, (d) High edge of high peak. The peak edge position labels are indicated in Figure 4.13.

Discussion

The histograms show approximately the accuracy of the optimization algorithm. All the 100 PCE results lie between 30.11% and 30.12%. The optimal bandgaps have values between 1.125 and 1.140 eV. The results seem to cluster around 2 bandgaps (1.1295 and 1.1345 eV). The explanation for this is given in Appendix C. In short, it comes from the resolution (0.1 nm) in the summation of AM1.5G to calculate the photocurrent due to absorption (J_L, see equation (3.4)).

Regarding the reflectance peak edges, it is observed that the position of the lower peak has more flexibility, as its edges move in the order of 2-3 nm. On the contrary, the higher peak is more fixed, with less than 0.5 nm of variability.

In general, it can be stated that the MOEAD method employed in the coloured opaque SJSC optimization gives repeatable results with an accuracy in the order of 0.01% for the maximum PCE limit and 0.01 eV for the optimal bandgap. Therefore, the errors due to the simplifications and approximations of the Boltzmann-Lambert approach can be disregarded (which were many orders of magnitude smaller, as seen in Section 4.1.2).

To sum up, in this section the results obtained for single junction solar cells have been analysed and understood. They have been compared to the work by Halme et al., proving that the results match if the same route is used for the calculation of the colour coordinates. Besides, it has been observed that the accuracy of the MOEAD is good enough to state that the found solutions for the coloured SJSCs are the optimal ones. In the following, the knowledge acquired will be used for optimization of coloured opaque IBSCs.

4.2 Intermediate Band Solar Cell

In this section, the results of the detailed balance analysis of intermediate band solar cells are presented and discussed, following the structure of the previous work on SJSCs. To begin with, the model employed in the calculation of the maximum PCE limit of the IBSC is validated by comparison with results from the literature. As it has been done for SJSCs, several approaches to simplify and accelerate the calculations are also considered for the code of IBSCs, together with their accuracy. Then, the results obtained when introducing the reflectance in the model are given. Finally, the model is utilized to calculate the maximum PCE limit, the optimum bandgap and subbandgaps, and the best rectangular reflectance spectrum of IBSCs with the colours of the Macbeth ColorChecker chart. Additionally, the repeatability of the optimization method employed is studied.

4.2.1 Validation of the model

First, the detailed balance model implemented in Linge's MATLAB program for IBSCs is validated. This was already done during Linge's master thesis, so it will be briefly reproduced here.[71] The maximum PCE achievable is calculated for IBSCs with main bandgap between 0.7 and 3 eV and low subbandgap between 0.3 eV and half of the main bandgap, with 0.01 eV steps in both cases. The results are displayed in Figure 4.16. Remember that $E_{low} < E_{high}$ by definition, so the cases with E_g and $E_{low} > E_g/2$ have not been calculated.

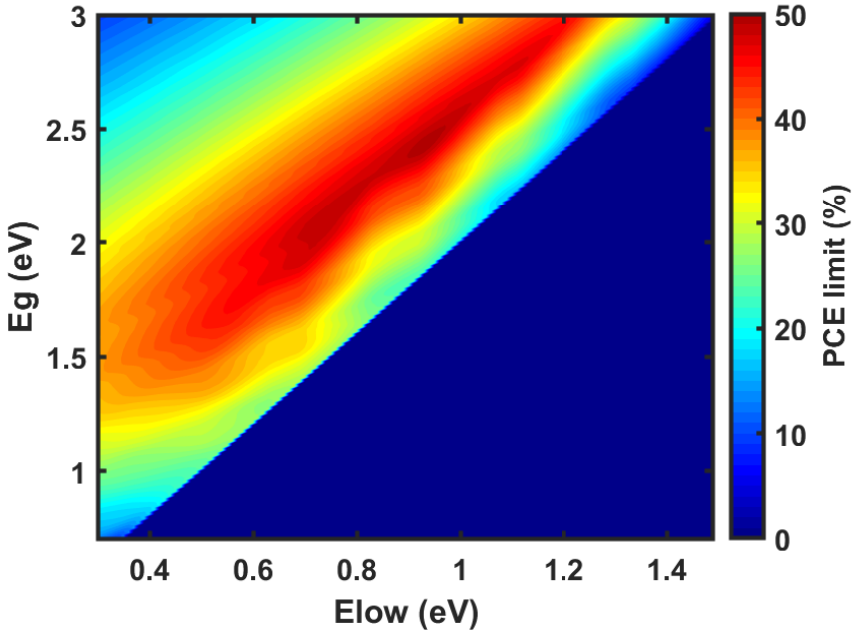

Figure 4.16: Maximum PCE limit calculated with detailed balance model implemented in Linge's program for an IBSC under AM1.5G illumination, for E_g between 0.7 and 3.0 eV and E_{low} between 0.3 eV and $E_g/2$ with 0.01 eV steps.

The maximum PCE limit of 49.5544% is achieved with a 2.42 eV main bandgap (E_g), and a low subbandgap (E_{low}) of 0.93 eV. In the thesis by Linge, these results were compared to the work by Bremner et al.[40] The maximum PCE limit, its bandgap-subbandgap combination, and the appearance of the maximum PCE map (the one shown in Figure 4.16) were checked and compared. According to Linge: "The similar traits for the contours [in the PCE limit map] and an error of only 1.04% in the maximum efficiencies makes the model viable for simulating the intermediate band solar cell with the use of the AM1.5 spectrum".[71]

4.2.2 Runtime acceleration approaches

The calculation of all the PCE limits considered takes around 25 hours using the program developed by Linge (with an Intel® Core™ i7-6500U CPU at 2.50GHz). This is a very long runtime if the code is to be implemented in the PCE calculation for the MOEAD. It is convenient to make the calculation of the maximum PCE limit with a certain bandgap-subbandgap combination faster.

In this section, the inclusion of different approximations and simplifications in the code is considered and tested. In order to do so, the original code implemented in Linge's program for IBSCs must be analyzed. For an IBSC with certain bandgap and low subbandgap, it basically calculates the efficiency for different voltage values, with a 500 point voltage sweep MPPT method. For every voltage value, it calculates for the three absorption paths (VB to CB, VB to IB, and IB to CB) the current density due to the absorption of photons from the sun (J_L) and from the

ambient (J_{amb}), and the current loss due to radiative recombination (J_{rad}), with equation (2.14c) (changing the integration limits accordingly). For each value of the voltage sweep, the current matching across both subbandgaps is ensured by modifying the positions of the quasi-Fermi level energies of VB and CB (E_{Fp} and E_{Fn}) employing a bisection method. Actually, it must be said that before the 500 point voltage sweep, a "primer sweep" of NVP/10 times (Number of Voltage Points divided by 10, i.e. 50 times) is performed. This calculates the value of the current for the mentioned number of equidistant points, from the voltage corresponding to the energy of the lowest subbandgap, to the voltage corresponding to the main subbandgap. The starting voltage for the main voltage sweep (of 500 points) is set at the voltage where the current changes 0.001% relative to the previous voltage point in this "primer sweep".

Table 4.4 lists some approaches that include approximations and simplifications in the calculation of the maximum PCE limit. Some changes concern the MPPT method. For example, the amount of points of the main and "primer" voltage sweep can be changed (keeping the "primer sweep" with 10 times less points). Otherwise, a new approximated MPPT algorithm can be developed based on the analytical solution of the V_{MPP} for each bandgap/subbandgap, according to equation (3.6) (see the logical flow chart in Figure 4.17 for the explanation of the newly developed algorithm). It must be stated that this algorithm has not been reported yet and it has been developed for this thesis. Other approximations affect the calculation of the current generation and loss (applying the Boltzmann approximation, and using the indefinite integral instead of numerically integrating). A name is given to each of the approaches for simplicity in the discussion.

Table 4.4: Runtime acceleration approaches tested for detailed balance calculations of IBSCs with their approximations and simplifications.

Name of approach	J_{rad} **and** J_{amb} **calculation**	**MPPT**
Linge	No Boltzmann approx. (eq. 2.14c)	500 point V sweep
Boltzmann	Boltzmann approx. (eq. 2.16)	500 point V sweep
Boltzmann 5000	Boltzmann approx. (eq. 2.16)	5000 point V sweep
Boltzmann 50	Boltzmann approx. (eq. 2.16)	50 point V sweep
Boltzmann-New MPPT	Boltzmann approx. (eq. 3.5)	Approx. algorithm (Fig. **??**)

Figure 4.18 shows the maximum PCE achievable for IBSCs with main bandgap between 0.7 and 3 eV and low subbandgap between 0.3 eV and half of the main bandgap, with 0.01 eV steps in both cases, calculated employing the approaches listed in Table 4.4. In addition, Figure 4.19 displays the difference between the maximum PCE calculated with each approach with respect to the Boltzmann 5000 approach (because this last one gives the highest value in almost all the energy range considered). Finally, 4.5 shows the runtime required to perform the necessary calculations for all the bandgaps considered for every approach, together with the maximum PCE limit found and the corresponding E_g and E_{low}.

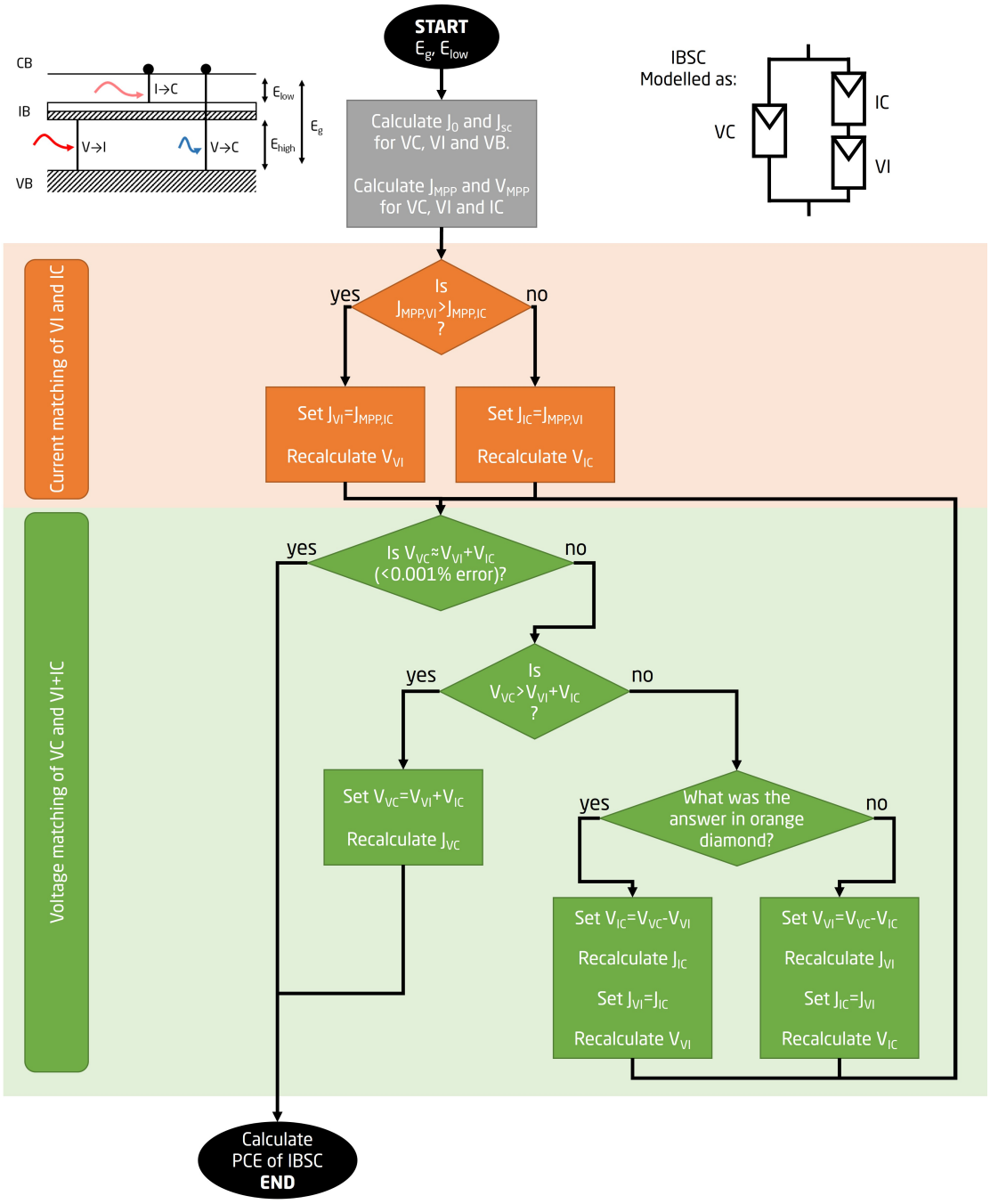

Figure 4.17: Logical flow chart explaining the developed new approximate MPPT algorithm for IBSC. The IBSC is modelled as two parallel strings of 1 and 2 solar cells (the first with E_g, and the latter with E_{low} and E_{high} bandgaps).

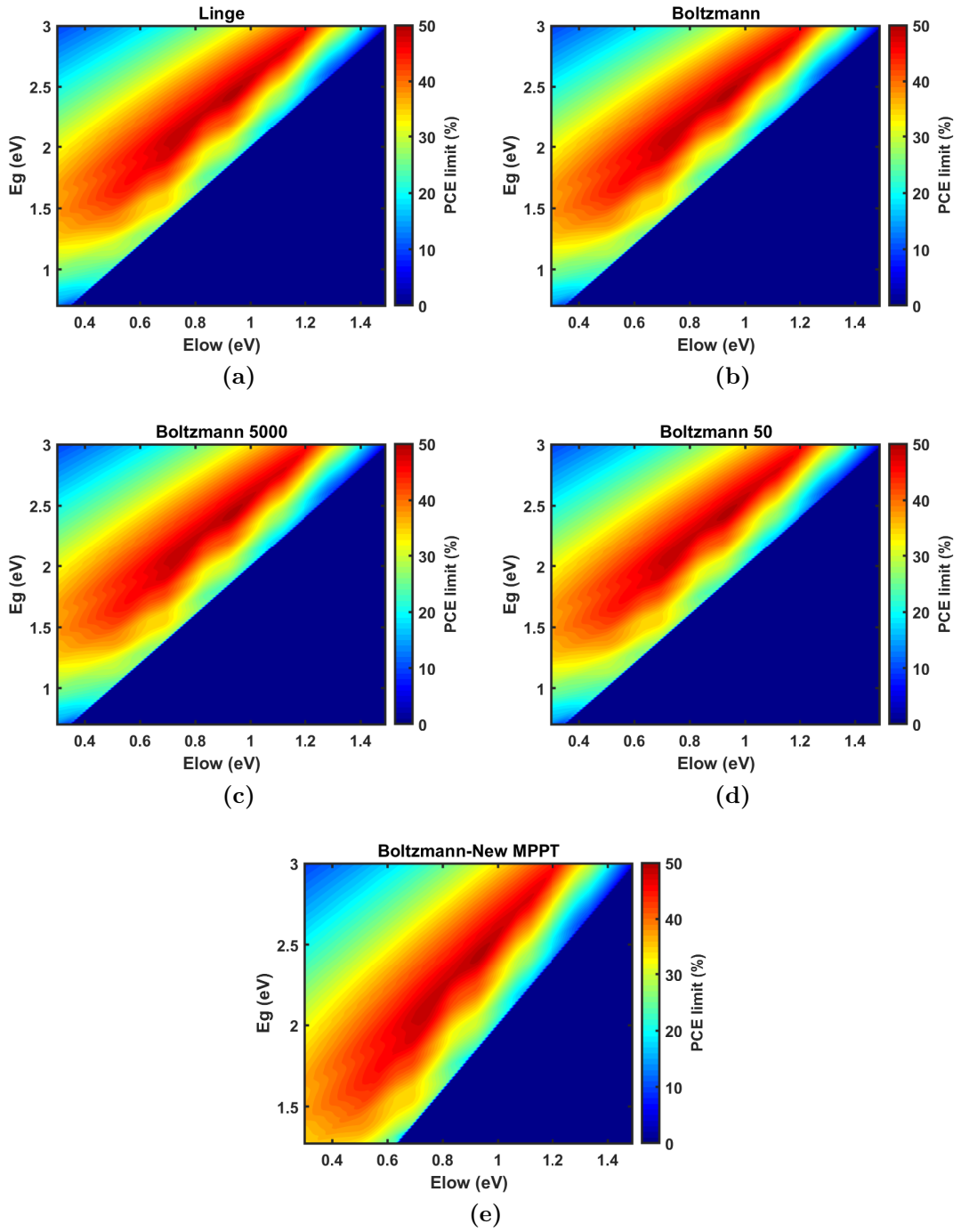

Figure 4.18: Maximum PCE limit calculated with different approaches, for an IBSC under AM1.5G illumination, for E_g between 0.7-3.0 eV and E_{low} between 0.3-$E_g/2$, with 0.01 eV resolution.

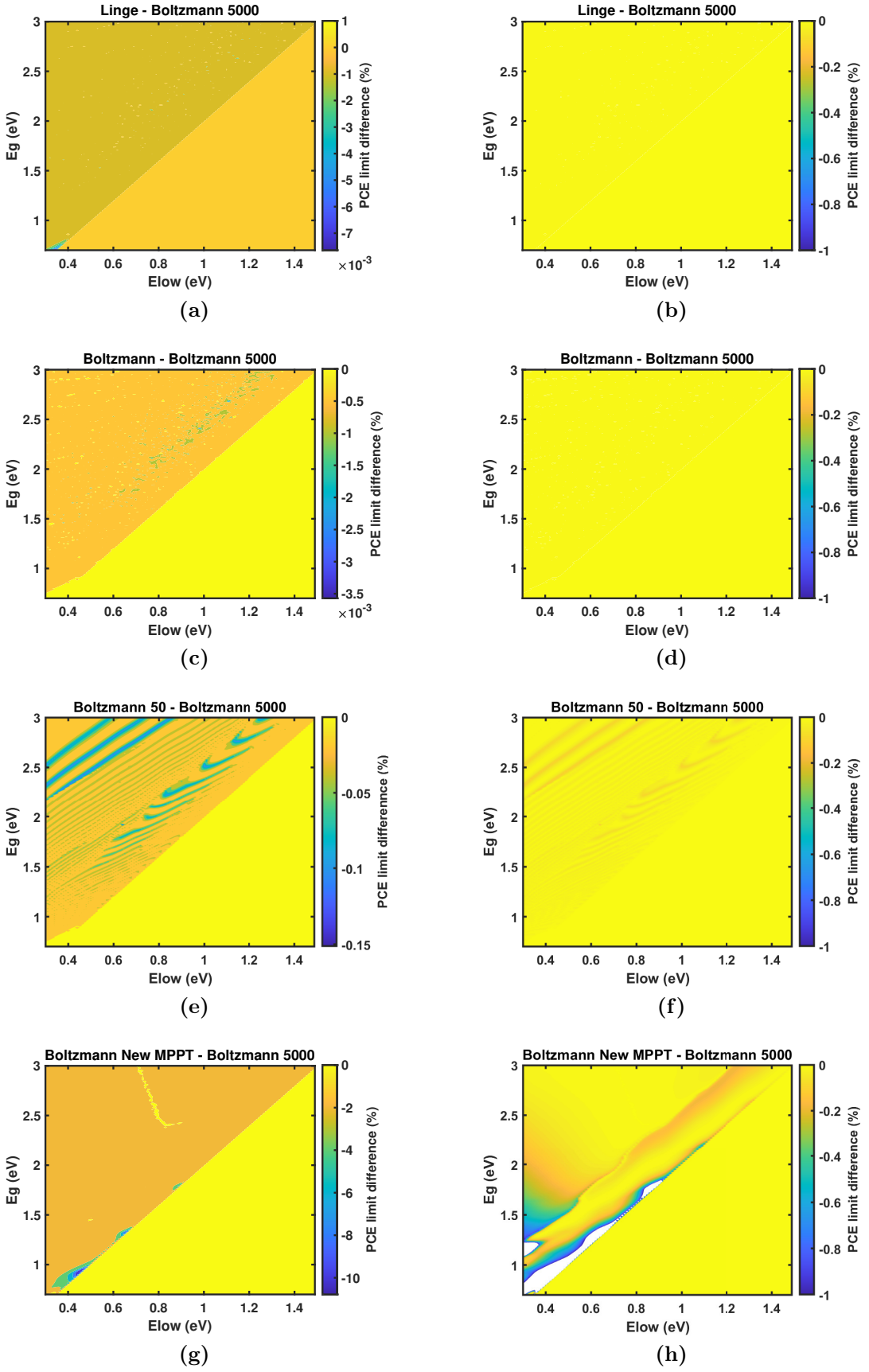

Figure 4.19: Difference in absolute percentage between maximum PCE calculated with different approaches to the Boltzmann 5000 approach (whose PCE is highest for all bandgaps). (b), (d), (f) and (h) have the same scale in the colorbar.

Table 4.5: Runtime for computing the PCE limit for IBSCs with E_g 0.7-3 eV and E_{low} between 0.3 eV and $E_g/2$, with 0.01 eV steps. The maximum PCE, and the corresponding E_g and E_{low} are included.

Approach	**Runtime* (s)**	**Max PCE (%)**	**E_g (eV)**	**E_{low} (eV)**
Linge	ca. 91000	49.5544	2.42	0.93
Boltzmann	63	49.5544	2.42	0.93
Boltzmann 5000	305	49.5545	2.42	0.93
Boltzmann 50	38	49.5532	2.42	0.93
Boltzmann-New MPPT	7	49.5167	2.43	0.93

*Runtime for a single try.

Discussion

In Figure 4.18, at plain sight it is difficult to tell much difference between the results of the approaches. The obtained maximum PCE limits, listed in Table 4.5 are very close to the reported value of 49.4% reported in the literature.[40] Besides, all the approaches give the maximum at the same E_g and E_{low} combination, except the Boltzmann-New MPPT approach, which finds the maximum at a 0.01 eV higher E_g.

For a thorough comparison of the approaches, Figure 4.2b displays the difference between the maximum PCE calculated with them, with respect to the Boltzmann 5000 approach. The left column of subfigures presents varying scales in the colorbar, whereas the right column presents the same scale for a better comparison between different approaches.

As for the Linge and Boltzmann approach, they give almost the same results as the Boltzmann 5000, with an error lower than 0.01% in absolute percentage for all bandgap and subbandgap combinations. In Figure 4.19a it can be seen that the difference between the Linge and Boltzmann 5000 approaches increases mostly for low E_g and E_{low} values (bottom left corner). This is again attributed to the fact that in all approaches but Linge's the Boltzmann approximation is applied, assuming $E - qV >> kT$. This assumption becomes less correct for low energy gap values, which explains the deviation in question. Concerning the Boltzmann approach, the scattered combinations with slightly higher error in Figure 4.19c (which has the appearance of noise) is caused by the lower accuracy of the 500 point V sweep of the MPPT. The same occurs in Figure 4.19a with the Linge approach, but the noise is less visible due to the higher difference at low bandgap values already commented before.

Regarding the Boltzmann 50 approach, its error is higher in general, with maximum PCE values almost 0.2% lower in absolute percentage compared to the Boltzmann 5000 approach. The error is probably caused by the inaccuracy of the MPPT with only 50 points. The wavy nature of the error (giving the zebra-like pattern) could be caused by areas where voltage matching between main bandgap and both subbandgap occurs or areas where current matching between

subbandgaps happens, and areas where it doesn't. However, the pattern and the variation of the current-voltage characteristics of the IBSC across it should be better analyzed to confirm this hypothesis.

Finally, the Boltzmann-New MPPT algorithm shows the highest error in some of the bandgap/subbandgap combinations, reaching a deviation of up to 11% in absolute percentage with respect to the Boltzmann 5000 approach. However, these large errors only occur in areas with very non-ideal bandgap combinations, where the voltage matching between the main bandgap and the subbandgaps is probably very bad, and the current matching between both subbandgaps is bad too. In contrast, in regions close to the bandgap combination giving the maximum PCE limit, the error is lower than 0.2 % for the most part. Furthermore, the maximum PCE limit falls in a very small error region, with an absolute error of 0.04%. It is interesting to observe the wave shaped diagonal line in Figure 4.19h. The maximum PCE limit of the Boltzmann-New MPPT approach falls exactly on the side of the diagonal with lowest error ($E_g = 2.43\ eV$ and $E_{low} = 0.93\ eV$). Besides, this wavy diagonal is also visible in the error of the Boltzmann 50 approach (it marks the boundary between the straight "zebra" lines, and the more curved error lines, in Figure 4.19e and 4.19f).

So, all the tested approaches give almost the same result for the maximum PCE bandgap/subbandgap combination (as discussed later, the error due to the approximations and simplifications is similar to the variability of the MOEAD algorithm). However, as it was the case for the approaches for SJSCs, the runtime of the calculations with each approximation is different, as shown in Table 4.5. Linge's method takes much longer because it calculates the integrals in equation (2.13) for every voltage value in the MPPT sweep. Applying the Boltzmann approximation accelerates the code, as the voltage gets out of the integral (see equation (2.16a)), reducing the runtime for the rest of approaches. The Boltzmann-New MPPT approach is the fastest because it uses the newly developed MPPT algorithm of Figure 4.17. In addition, it uses the indefinite integral instead of numerically integrating.

In conclusion, as all approaches have almost the same accuracy around the bandgaps with maximum PCE, one would probably opt for the fastest method for calculating efficiency limits of ISBCs, specially when applied in the MOEAD method. However, it is necessary to check if all the approaches still give similar results when the reflectance is introduced in the model, which is discussed in the following section.

4.2.3 Reflectance introduction in the model

As already explained in Section 2.4.4.3, the detailed balance model is modified to include coloured opaque PV cells, by introducing the reflectance in the computation of the different currents (J_L, J_{amb} and J_{rad}), and so in the maximum PCE limit calculation. In this section, the effect of introducing the reflectance in the model for IBSCs is studied.

For that purpose, as it has been done for SJSCs, an arbitrary reflectance spectrum is selected (see Figure 4.3 from Section 4.1.3). This consists of a null reflectance baseline, with a perfect reflection band between 400 nm and 700 nm. The solar cell would appear white under daylight illumination, because it would reflect almost all the visible light.

From Section 4.1.3 it has been concluded that it is necessary to include the reflectance in all the current components (J_L, J_{amb} and J_{rad}, although the effect in J_{amb} is negligible). Therefore, the study of introducing the reflectance in the different components or not will not be repeated for IBSCs. Instead, R will be introduced directly in the calculation of J_L, J_{amb} and J_{rad}, as shown in equations (3.4) and (3.1). This is done for all the different approaches presented in Table 4.4 (except for the Linge approach, because it has a long runtime, and it is basically the same as the Boltzmann approach). For those approaches that use a numerical integration of an integral to calculate the currents (i.e., using equation (3.1): Boltzmann, Boltzmann 5000 and Boltzmann 50), a discrete summation with 1 nm interval has been employed. On the contrary, if the indefinite integral is utilized (eq. (3.3), in Boltzmann-New MPPT approach), the different parts of the integral where the reflectance is 0 have to be summed. That is, the change in integration limits has to be taken into consideration.

Figure 4.20 shows the maximum PCE achievable with IBSCs with E_g between 0.7 and 3 eV and E_{low} between 0.3 eV and $E_g/2$, with 0.01 eV steps, and perfect reflectance between 400 and 700 nm, calculated employing the approaches listed in Table 4.4 (except the Linge approach). Besides, Table 4.6 shows the maximum PCE limit found and the corresponding E_g and E_{low}, for every approach. Finally, Figure 4.21 displays the difference between the efficiency calculated with the Boltzmann 5000 approach (which gives the maximum PCE for almost all the bandgap combinations considered) and the rest of approaches.

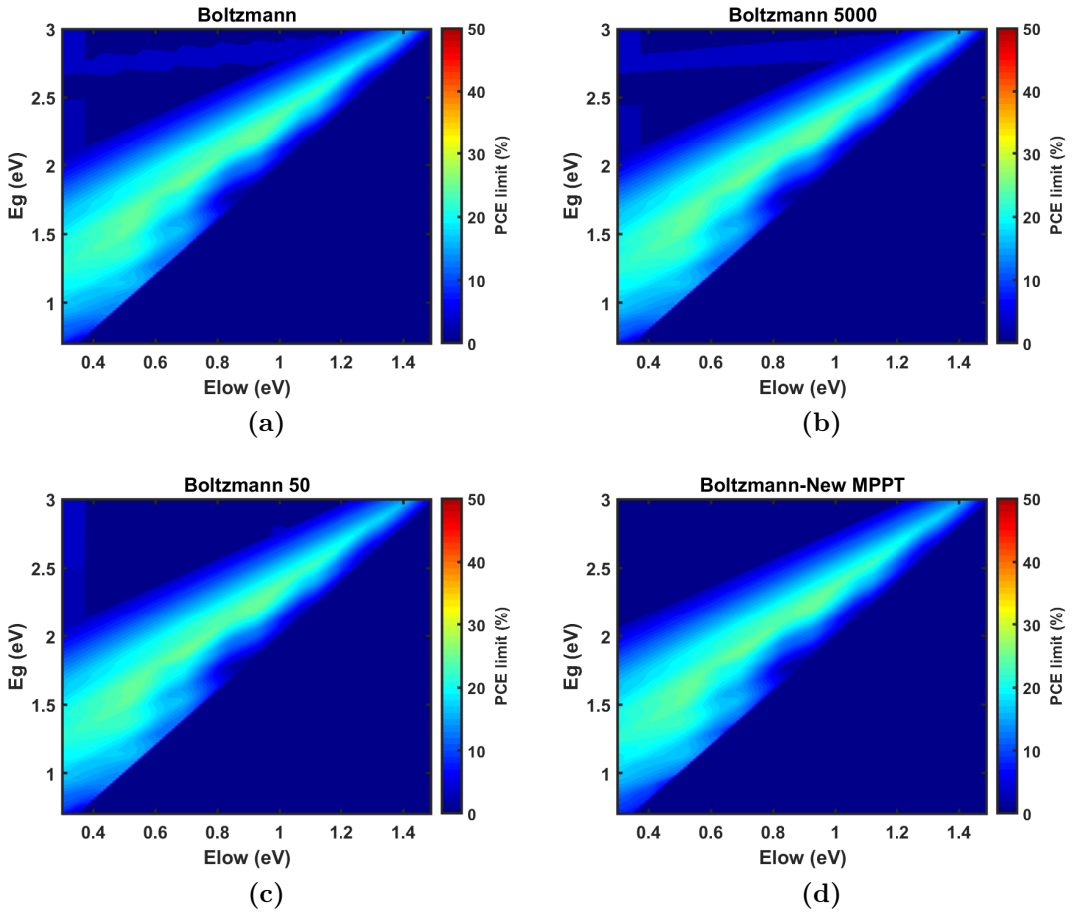

Figure 4.20: Maximum PCE limit calculated with different approaches, for an IBSC under AM1.5G illumination, for E_g between 0.7 and 3.0 eV and E_{low} between 0.3 eV and $E_g/2$, with 0.01 eV resolution, with spectral reflectance R=1 between 400-700 nm.

Table 4.6: Maximum PCE limit for IBSC with E_g between 0.7 and 3 eV and E_{low} between 0.3 eV and $E_g/2$, with 0.01 eV steps, for R=1 between 400 and 700 nm. The corresponding E_g and E_{low} are included.

Approach	**Max PCE (%)**	**E_g (eV)**	**E_{low} (eV)**
Boltzmann	25.2315	1.89	0.70
Boltzmann 5000	25.2316	1.89	0.70
Boltzmann 50	25.2290	1.89	0.70
Boltzmann-New MPPT	25.2065	1.90	0.70

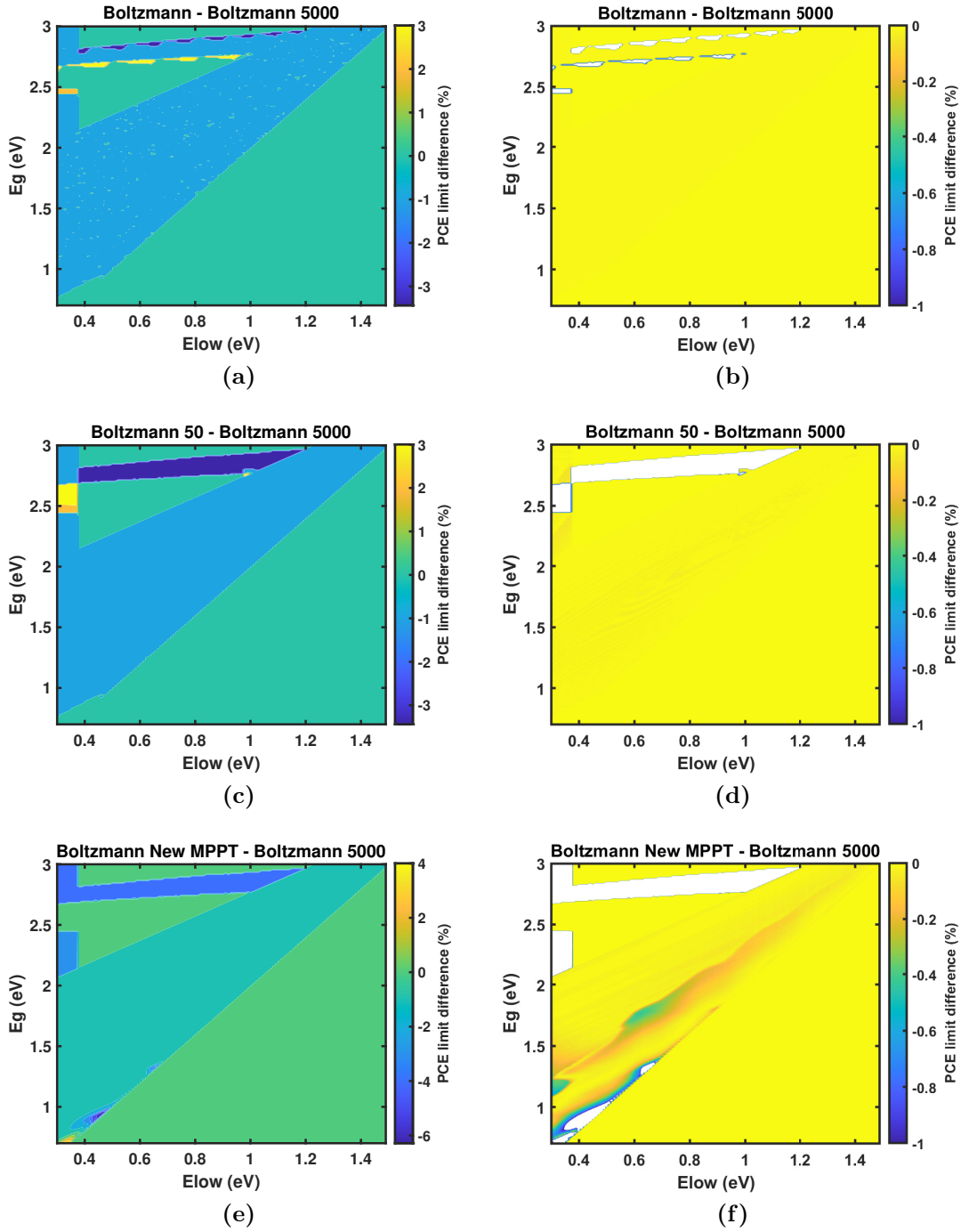

Figure 4.21: Difference in absolute percentage between maximum PCE calculated with different approaches to the Boltzmann 5000 approach (this last gives the highest PCE for almost all bandgap combinations), with reflectance included. (b), (d) and (f) have the same scale in the colorbar.

Discussion

At first sight, the colormaps displayed in Figure 4.20 seem quite similar in the high efficiency regions. However, there are some low efficiency areas that differ considerably from one approach to the other. In particular, this occurs in the

triangle shaped area in the top left position of the colormaps. The bandgap configurations in this area have the particularity that $(E_g - E_{low}) > 1.77eV$. $1.77eV$ is the lower energy edge of the reflecting band between 400-700 nm, the other edge (400 nm) corresponding to 3.1 eV. Therefore, those bandgap configurations with $(E_g - E_{low}) > 1.77eV$, but $E_g < 3.1eV$, have a E_{high} value such that it has no absorption (because all the photons it could absorb are reflected). So, the current generation through the intermediate band is disabled. Therefore, all the bandgap combinations in the discussed triangle should have the maximum PCE limit corresponding to a single junction solar cell with the bandgap equal to the main bandgap of the IBSC (which is given in Figure 4.4). Nevertheless, the developed approaches do not respond well to those cases where the current across the subbandgaps is zero, giving the visible artifacts (mostly because they try to impose current matching of both subbandgaps in their algorithm). So, these regions will be ignored, and only the bandgap combinations giving the higher efficiencies (with $(E_g - E_{low}) < 1.77eV$) will be discussed.

In the high efficiency areas, the conclusions that one can get when the reflectance is included are similar to those from Section 4.2.2, which did not consider any reflectance. Regarding the Boltzmann approach, as in the case without reflectance, it gives almost the same results as the Boltzmann 5000, with an error lower than 0.01% in absolute percentage for all bandgap and subbandgap combinations. The scattered combinations with slightly higher error in Figure 4.21a (which has the appearance of noise) are caused by the lower accuracy of the 500 point V sweep of the MPPT.

As for the Boltzmann 50 approach, again the error shows up like "zebra" patterns in the colormap in Figure 4.21d (although more faint than in the case without reflectance from Figure 4.19f), which is most probably attributed to inaccuracies in the MPPT due to the few V points of the sweep.

Finally, concerning the Boltzmann-New MPPT approach, the error has a similar form to the case without including the reflectance. It shows the highest error in some of the bandgap/subbandgap combinations, reaching a deviation of up to 6% in absolute percentage with respect to the Boltzmann 5000 approach (see Figure 4.21e). Furthermore, it gives up to 4% higher PCE for very small values of the low subbandgap. This is similar to the case of the Figure 4.19a, which compared the Linge and Boltzmann 5000 approaches without reflectance. In that case, the difference was attributed to the Boltzmann approximation in only one of the approaches. However, both Boltzmann 5000 and Boltzmann-New MPPT apply the Boltzmann approximation. Therefore, the positive difference in that area must be caused by some other error, which has not been found yet. However, these large errors only occur in areas with very non-ideal bandgap combinations, where the voltage matching between the main bandgap and the subbandgaps is probably very bad, and the current matching between both subbandgaps is bad too. Therefore, it is normal that the developed MPPT algorithm for IBSCs (seen in Figure 4.17) fails in those areas. In contrast, in regions close to the bandgap combination giving the maximum PCE limit, the error is lower than 0.4 % for the most part. Moreover, the maximum PCE limit falls in a very small error region, with an absolute error of 0.013%.

To ensure that the maximum PCE limit calculated with the Boltzmann-New MPPT approach always falls in a region of low error with respect to the more accurate Boltzmann 5000 approach, the calculation has been repeated for other reflectance spectra. The results are displayed in Table 4.7, and they show that the maximum efficiency calculated with the Boltzmann-New MPPT approach are close to the ones obtained using the most accurate Boltzmann 5000 approach (with an error below 0.1% for the tested reflectance spectra).

Table 4.7: Absolute percentage difference in maximum PCE limit for IBSC using Boltzmann 5000 and Boltzmann-New MPPT approaches with distinct reflectance spectra.

Wavelength range with R=1 (nm)	**PCE limit difference (%)**
400-700	-0.0251
600-700	-0.0427
400-500 and 600-700	-0.0735
438-459 and 535-580	-0.0397

In conclusion, all the approaches give a similar result for the maximum PCE bandgap/subbandgap combination, even when the reflectance is included in the model. As a consequence, the Boltzmann-New MPPT approach with the reflectance included has been chosen for the following section, were it has been applied to calculate the maximum PCE limit achievable with IBSCs with the colours of the Macbeth ColorChecker chart. This approach is chosen mainly due to its fast runtime, which is crucial for application in MOEAD. It has been concluded that the approximation and simplifications performed in the model with the Boltzmann-New MPPT approach give a result close enough to the optimum, so that it can be further applied on the optimization of coloured opaque IBSCs, by employing the MOEAD optimization.

4.2.4 Application to Macbeth ColorChecker chart

Considering the knowledge acquired in the previous sections, the ECoPV program has been modified to include the possibility to calculate the maximum PCE limit of coloured opaque IBSCs. For that purpose, the PCE calculation has been performed with the Boltzmann-New MPPT approach (see Table 4.4). In this case, the MOEAD algorithm has an additional decision variable in the decision vector, because the code for SJSCs only optimizes one bandgap value, but the program for IBSCs needs to optimize both E_g and E_{low} (the E_{high} value depends on these two).

The results obtained with the MOEAD optimization algorithm are shown in the figures below. In Figure 4.22a the target colour and the found optimized colour are displayed, following the coordinate conversion to sRGB explained in Section 4.1.4. The XYZ tristimulus of the former have been computed from the xyY coordinates, and the ones of the latter from the reflectance spectrum, employing

the D50 as standard illuminant. Afterwards, these have been converted into sRGB values, which are displayed on the screen. As an alternative, Figure 4.22b shows the ΔE_{00} colour difference between target and found optimized colours.

Figure 4.23a presents the maximum PCE limit achievable with each colour, considering the rectangular-shaped reflectance spectrum with two bands. Again, the PCE as a function of the relative luminosity (Y) of the colour is plotted in Figure 4.23b, and the power loss (P_{loss}, with respect to 49.5167%, the limit for an ideal black IBSC) is shown in Figure 4.23c. Figures 4.24a and 4.24b display the optimal bandgap and subbandgap values to achieve the maximum PCE for each colour, and their variation with Y, respectively. Instead of employing the relative luminosity as the free variable, Figure 4.25 shows the variation of the PCE limit, the P_{loss}, and the optimal bandgap values, as a function of the perceptual lightness (L^*). The optimized reflectance spectra for IBSCs with the colours of the Macbeth ColorChecker chart are shown in Figure 4.26, indicating the perfectly reflecting bands with colour stripes. Finally, Figure 4.27 shows the difference (in absolute percentage) of P_{loss} of optimized coloured SJSCs and IBSCs.

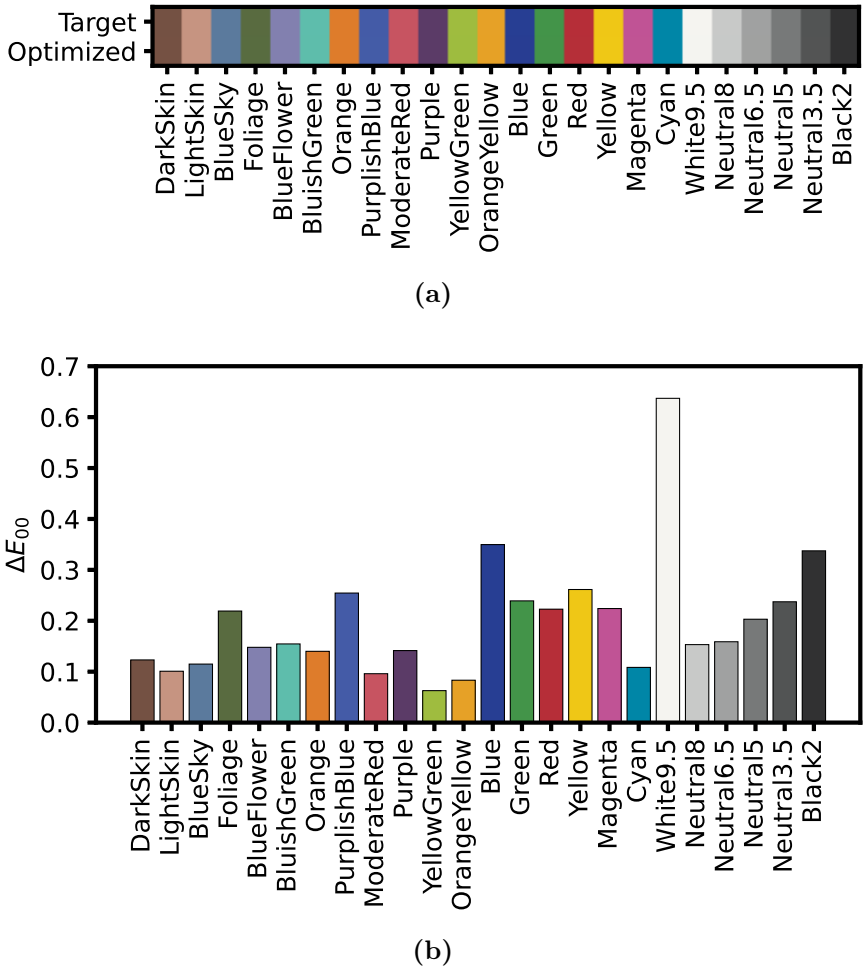

Figure 4.22: (a) Target (top half of rectangles) and optimized (bottom half) colours of the Macbeth ColorChecker chart, displayed based on their sRGB co-ordinates with D50 as illuminant, for the optimized IBSCs. (b) ΔE_{00} between target and optimized colour, with D50 as illuminant.

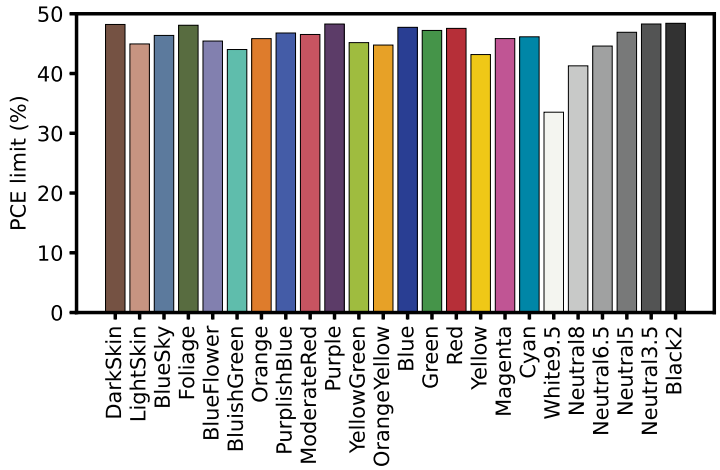

(a)

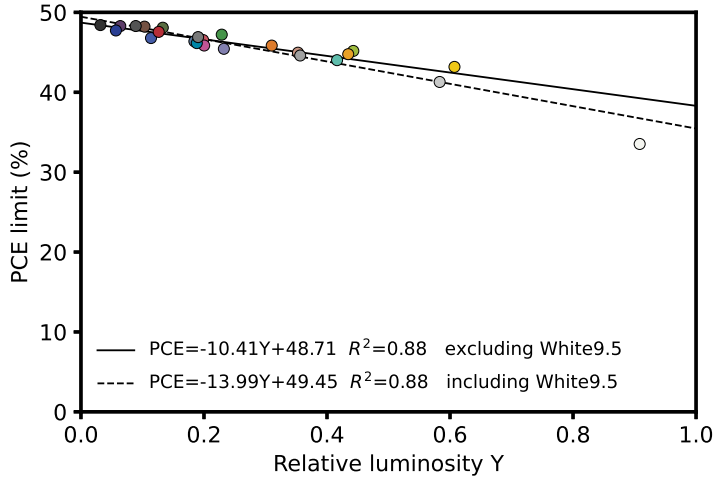

(b)

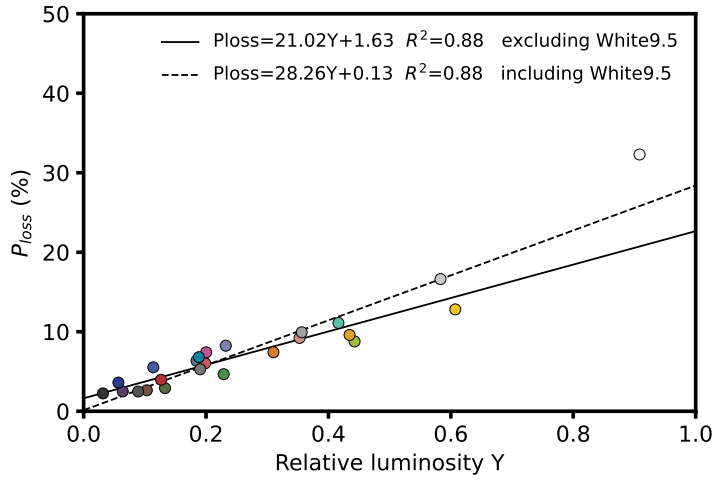

(c)

Figure 4.23: (a) PCE limit of optimized coloured IBSCs with colours of the Macbeth ColorChecker chart. (b) Obtained PCE limit and (c) P loss with respect to the optimal black cell, both as as a function of relative luminosity Y (the linear regressions excluding and including the White9.5 data point are shown).

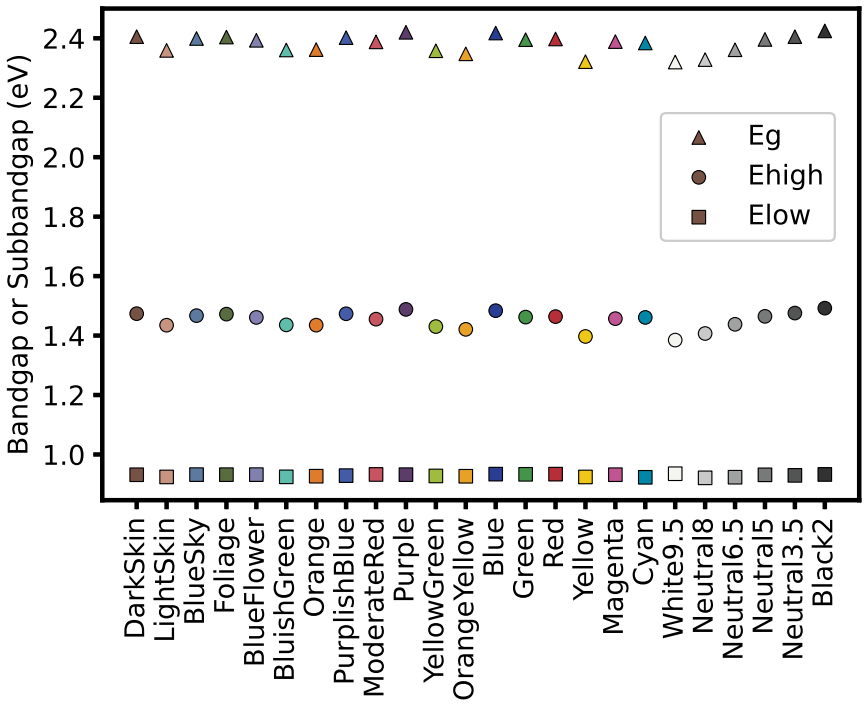

(a)

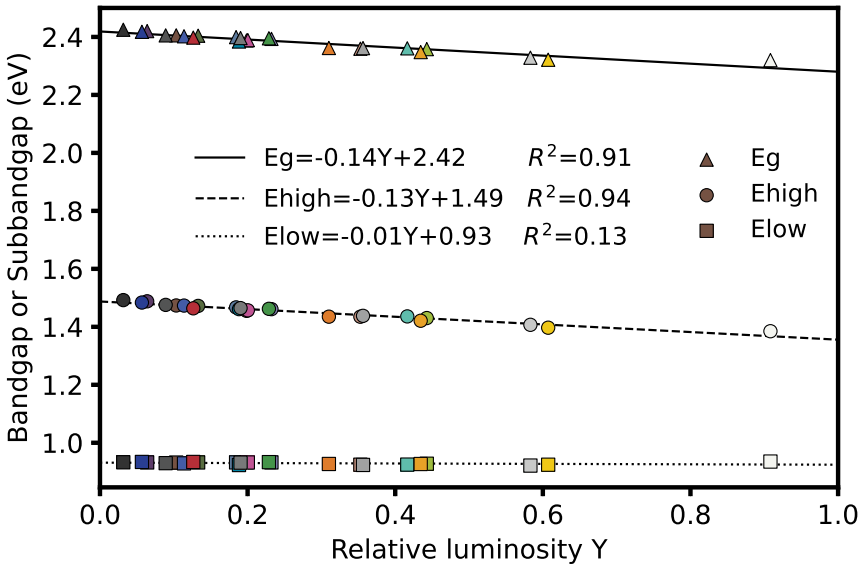

(b)

Figure 4.24: (a) Optimal bandgap and subbandgaps for coloured IBSCs with 24 colours of the Macbeth ColorChecker chart. (b) Optimal bandgap as a function of relative luminosity Y.

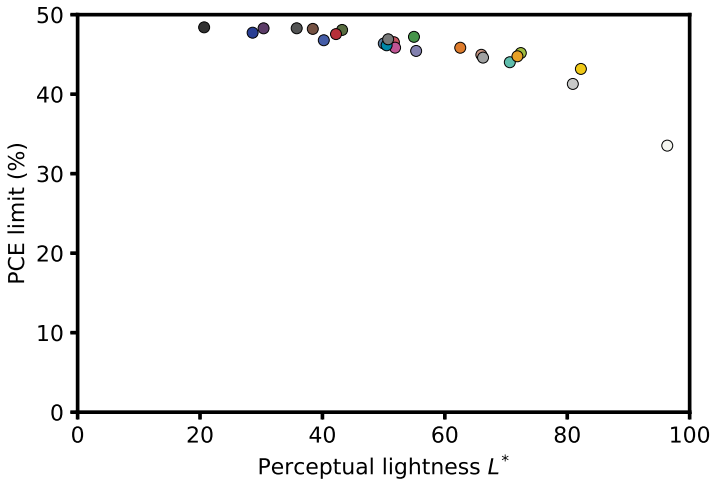

(a)

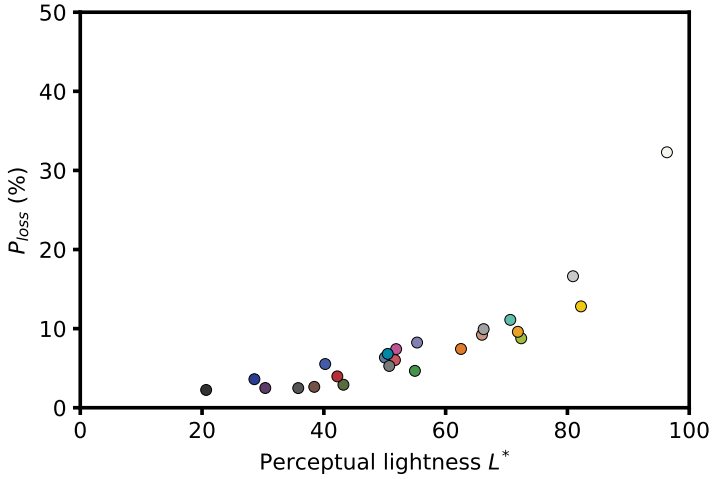

(b)

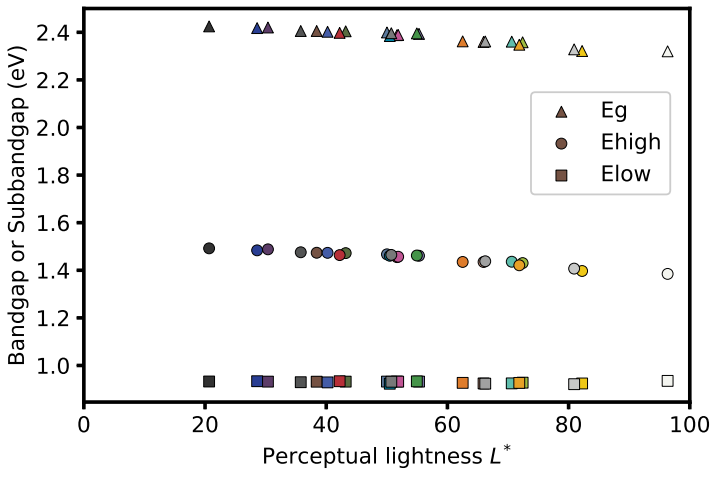

(c)

Figure 4.25: (a) PCE limit, (b) relative power density loss, and (c) optimal bandgap and subbandgaps of coloured IBSCs as a function of L^*.

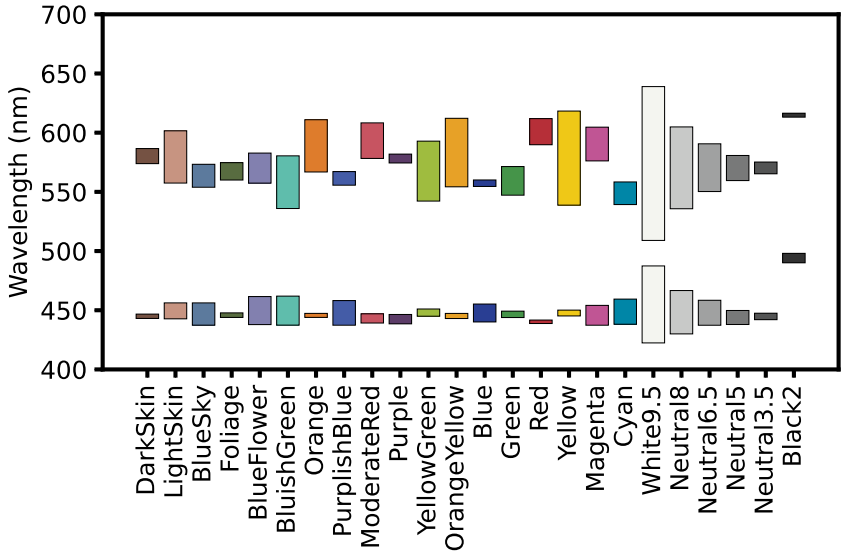

Figure 4.26: Illustration of reflectance spectra of optimized coloured IBSCs: the bar indicates the wavelengths were the reflectance value is 1, while the reflectance is 0 for the rest of wavelengths.

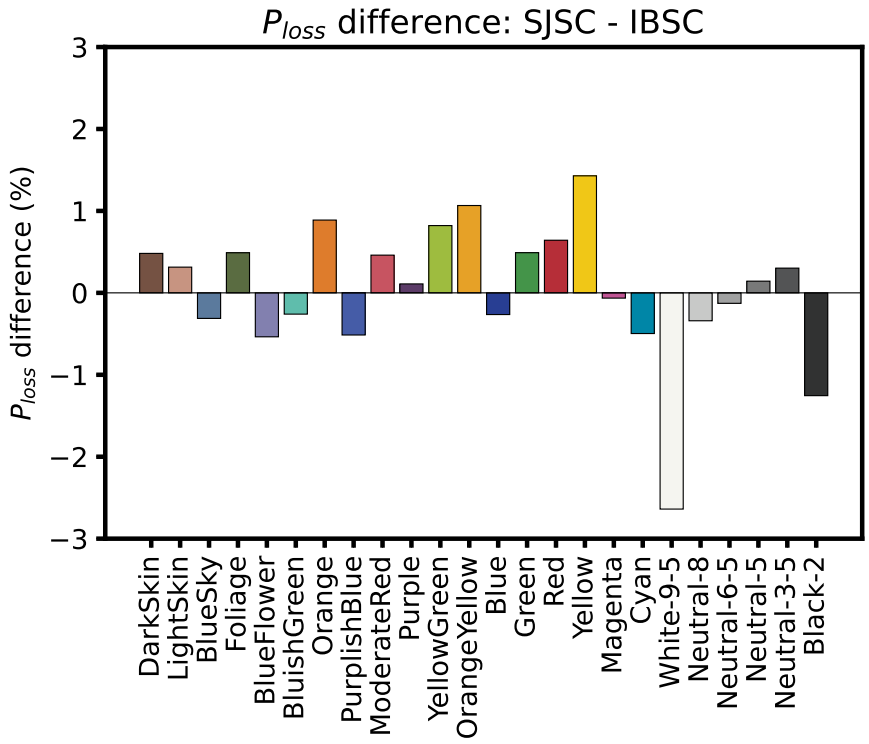

Figure 4.27: Difference (in absolute percentage) of power density loss of optimized coloured SJSCs and IBSCs (positive value means that the single junction solar cell has a higher relative P_{loss}).

Discussion

In Figure 4.22a, the colour patches showing sRGB coordinates of the target colour and the found optimal reflectance spectra seem indistinguishable. Their ΔE_{00} is given in Figure 4.7b, as a reference for possible comparison with other results that may be reported in the future.

Regarding the maximum PCE achievable, in Figure 4.23b, the efficiency decreases linearly with the increasing value of Y, and then drops non-linearly at high Y. For example, the result for the White9.5 colour does not follow the linear trend. So, this behaviour is the same as what has been found for SJSCs in Section 4.1.4. However, the coefficient of determination (R^2) value of the linear regressions of the PCE as a function of Y is lower in the case of IBSCs, as compared to SJSCs. There are two possible hypothesis for this. On the one hand, it could be that the PCE limit values depends more on other factors than just Y for IBSCs, as compared to SJSCs. For example, it could be that the factor of the hue affects more in the case of the IBSCs, which in SJSCs already causes a different PCE limit for the same Y value, as reported by Halme et al.[20] On the other hand, it could be that the dependency between PCE limit and Y for IBSCs is less linear, or it loses its linear behaviour at a lower Y, as compared to the SJSCs. This could come from the fact that the IBSC can be considered equivalent to 3 solar cells, as already explained. Despite the hypotheses, the cause for the higher dispersion away from the linear trend in the case of IBSCs remains uncertain. So, it would be helpful to analyze the optimization of more colours.

The power loss with respect to the ideal black cell follows the inverse trend. Again, as in the case of SJSCs, these values may be more relevant for real IBSCs, which will have considerably lower efficiencies for both the black and the colored devices. That is, it gives an idea about the minimum (best case) efficiency loss of a "real" coloured IBSC (with optimized rectangular shaped reflectance spectrum), compared to the black device. This fact of the relativeness inherent to P_{loss} may be considered more important for IBSCs than for SJSCs, because the IBSCs developed so far are further away from the ideal PCE limit than the single junction solar cells.

Regarding the optimal bandgap and subbandgap values for each colour, it can be seen that they follow some trend as a function of Y. Figure 4.9b shows that the optimal E_{low} has a constant value of 0.93 eV, regardless of Y. In contrast, E_g and E_{high} follow negative linear trends with increasing Y. As Y increases, the optimal E_g has to decrease so that the current in the absorption from VB to CB is increased. If E_{high} was kept constant, that would lower the absorption in the high subbandgap (both because E_g is lowered "stealing" photons from E_{high}, and because the high wavelength reflectance band decreases the absorption in E_{high}), causing current mismatch between the absorption from VB to IB, and from IB to CB. Therefor, as E_g decreases, the optimal E_{high} also decreases, so that the current through the high subbandgap increases and the current through the low subbandgap is lowered, in order to have better current match between them.

In Figure 4.10 the dependency of PCE, the relative power loss and the optimal bandgap as a function of the perceptual lightness (L^*) can be seen. Again, the tendency is similar to that against Y, but specially for PCE and power loss it has a less linear shape. This arises from the cubic relation in the conversion between Y and L^* for most Y values (see equation (2.22)).

Figure 4.11 displays the positions of the reflectance bands for each studied colour. The bars mark the wavelength ranges where the solar cell is perfectly reflective ($R = 1$). As opposed to the case of the single junction solar cell, these optimized reflectance spectra may not be the absolute optimal reflectance spectra for coloured opaque IBSC. As explained by Halme et al.[20], the reflectance spectrum with two rectangular peaks centered around the maxima of the CMFs are the optimum for coloured SJSCs, because they minimize the photon use for colour rendering. However, this is true because the bandgap of the SJSCs falls out of the visible region, so the reflectance spectrum and the bandgap can basically be optimized separately. However, for IBSCs the optimum E_g falls in the VIS. Thus, it has not been proven that the reflectance spectrum with 2 bands is the optimum for coloured IBSCs. For the rectangular band reflectance spectra considered, the bands mostly have the same positions for most colors, around the maxima of the CMFs, as in the case of coloured SJSCs. The exception is the Black2, which gives a significantly different result.

Finally, Figure 4.27 shows the difference of power density loss of optimized coloured SJSCs and IBSCs. It can be observed that for colours with blue hue, the P_{loss} of the IBSC is higher, whereas it is the opposite for colours with green-yellow-red hue. It can be caused by the fact that the current generation across the main bandgap of the IBSC depends more on high energy (blue) photons, so that IBSCs are more affected by the reflection of those photons. On the other hand, as the E_{low} and E_{high} values can be twicked, they can be modified so that the reflectance of photons corresponding to green-yellow-red affects less, in comparison to SJSCs.

As for spring 2023, the search in scientific publication browsers indicates that this is the first time that the optimization of coloured IBSCs has been studied. Therefore, there are no explicit results in the literature with which to compare. However, in this section, it has been possible to compare the observed results and tendencies with the previous results acquired in the analysis of coloured single junction solar cells. Once again, as in the case of SJSCs, the reproducibility of the utilized MOEAD algorithm is studied next.

4.2.4.1 Repeatability of the optimization algorithm

As it has been done for SJSCs, it is necessary to study the repeatability of the MOEAD method for optimization of coloured opaque IBSCs. So, the optimization of the Bluish Green IBSC has been run independently 100 times in order to analyze the repeatability of the results.

The most efficient result has a 44.022 % PCE, for $E_g = 2.358\ eV$ and $E_{low} = 0.924\ eV$, and perfect reflecting bands between 437.4-461.8 nm and 535.9-580.3 nm

(see the reflectance spectrum in Figure 4.28). The distribution of the optimized efficiency results are displayed on the histogram of Figure 4.29a, while Figures 4.29b, 4.29c and 4.29d present the distribution of the optimal bandgaps and sub-bandgaps. Last, the distribution of the optimal reflectance band edge positions are shown in Figure 4.30.

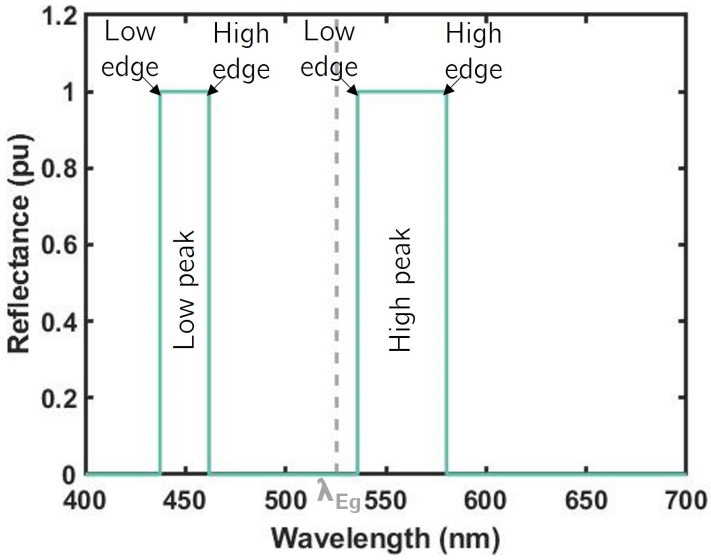

Figure 4.28: Reflectance spectrum of best optimized Bluish Green IBSC out of 100 runs, with the wavelength corresponding to the optimal E_g marked by the gray dashed line. The labels are indications for Figure 4.30.

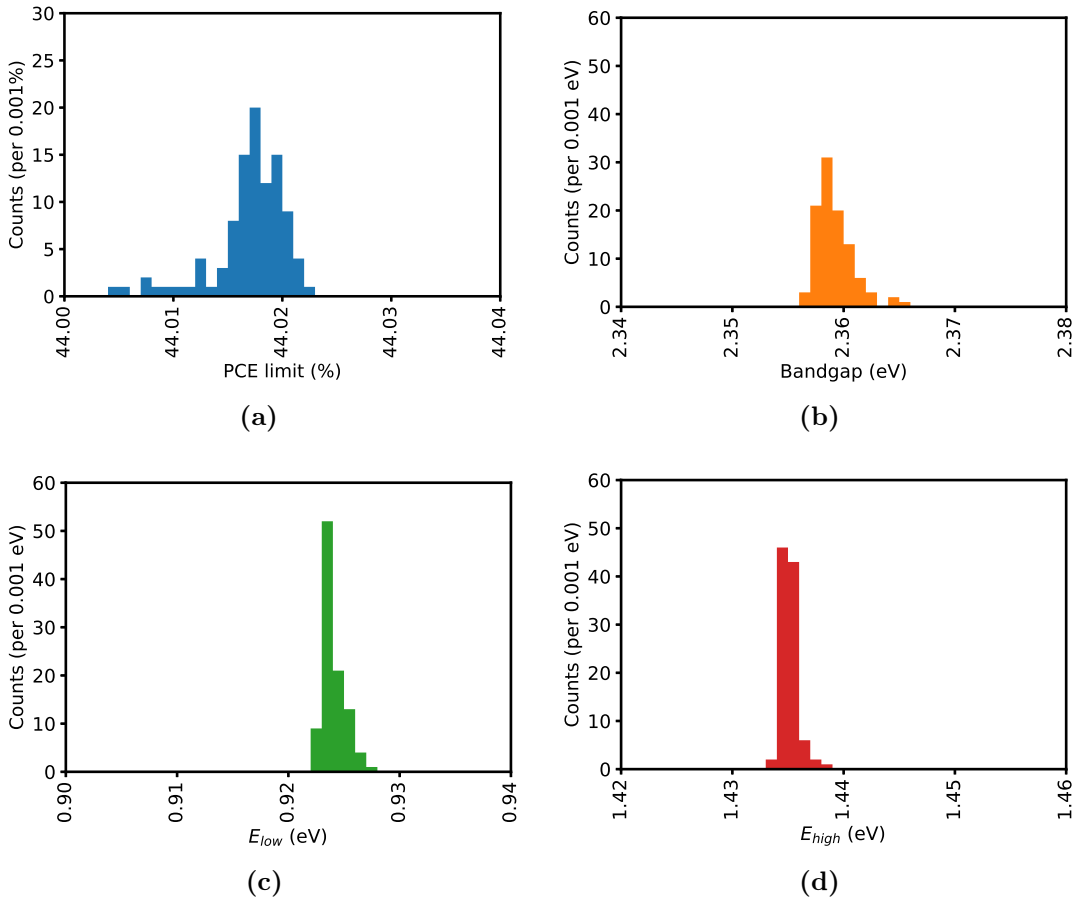

Figure 4.29: Distribution of the results in the 100 optimization runs of the Bluish Green IBSC: (a) PCE limits, (b) optimal E_g, (c) optimal E_{low}, and (d) optimal E_{high}.

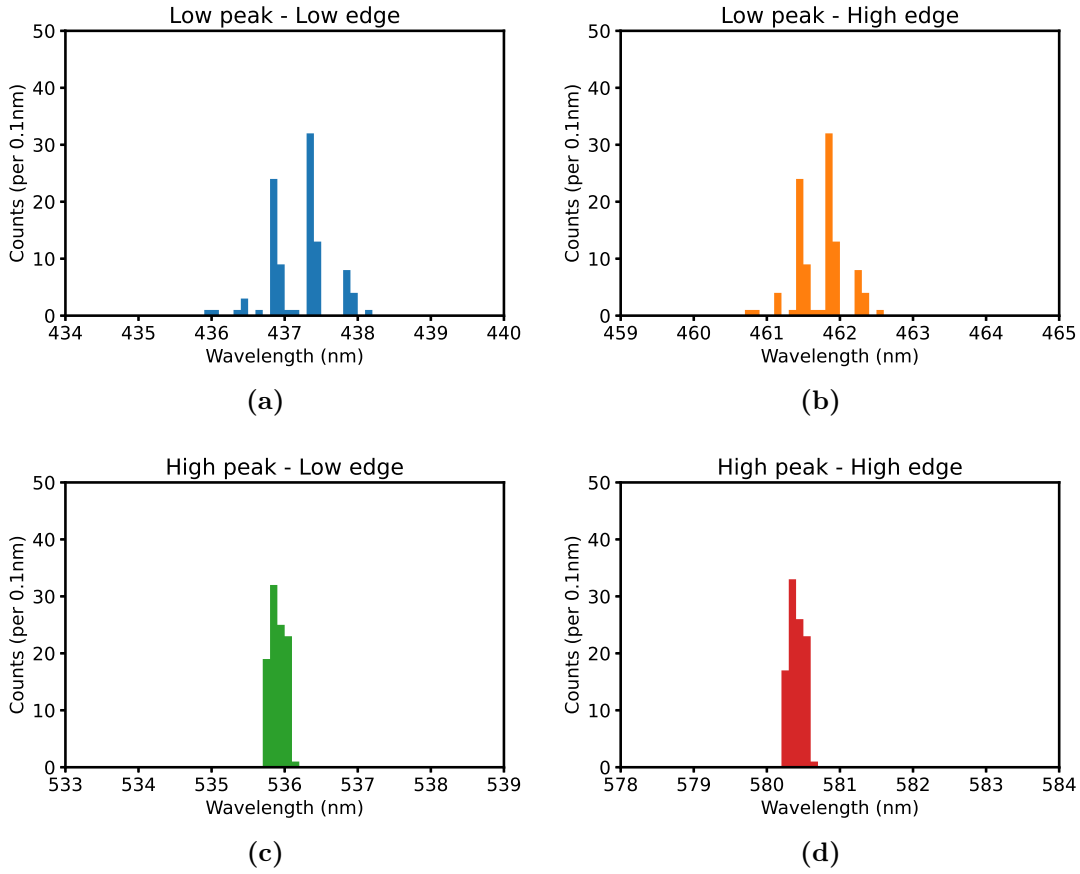

Figure 4.30: Distribution of the reflectance band edge positions in the 100 optimization runs of the Bluish Green IBSC: (a) Low edge of low peak, (b) High edge of low peak, (c) Low edge of high peak, (d) High edge of high peak. The peak edge position labels are indicated in Figure 4.28.

Discussion

The histograms show approximately the accuracy of the optimization algorithm. As for the PCE, all 100 results lie between 44.00% and 44.03%. The optimal bandgaps have values between 2.35 and 2.37 eV, the optimal E_{low} are between 0.92 and 0.93 eV, and the optimal E_{high} are between 1.43 and 1.44 eV. It seems the E_g has more flexibility, which may be because E_{low} and E_{high} have to be more exact in order to ensure current matching across the subbandgaps.

As for the reflectance peak edges, the case is similar to what has been observed in the Bluish Green SJSC. In Figure 4.30 the position of the lower wavelength band has more flexibility, as its edges move in the order of 2-3 nm. On the contrary, the higher wavelength band is more fixed, with less than 0.5 nm of variability.

In general, it can be stated that the MOEAD method employed in the coloured opaque IBSC optimization gives repeatable results with an accuracy similar to that for SJSCs, in the order of 0.03% for the maximum PCE limit and 0.02 eV for the optimal bandgap and subbandgaps. These are in the same order as the difference between the results that have been observed between the Boltzmann-New MPPT

approach (the one used to get these results) and the more accurate Boltzmann 5000 approach, in Sections 4.2.2 and 4.2.3. So, the results obtained for the optimization of colored IBSCs have the error contribution of both sources: the utilization of MOEAD as optimization algorithm (with its inherent randomness), and the use of approximations and simplifications in the code to perform detailed balance analysis. It must be stated that the repeatability analysis has been performed for only one colour. So, it would be convenient to check if the repeatability of the method is similar for other colours.

In short, results obtained in the optimization of coloured opaque IBSCs have been analysed and discussed. They have been compared to the results observed for single junction solar cells in Section 4.1.4. Furthermore, it has been tested that the error of the MOEAD is similar to the error due to the approximations and simplifications in the detailed balance analysis, so that both contribute to the final error. As already commented, other studies on the optimization of coloured IBSCs have not been found in the literature. However, they follow a similar trend to coloured SJSCs, with differences in some aspects. It would be interesting to compare the results with other coloured multibandgap solar cells, for example 2T and 4T double- or triple-junction tandem cells. On this matter, the results from the ECoPV project on optimization of coloured multijunction tandem cells are expected to be published soon. Once those results are available, it would be intriguing to compare the results obtained with coloured IBSCs and tandem cells.

4.3 Efficiency limit with reflectance of MorphoColor concept

In this section, the detailed balance analysis is performed for SJSCs and IBSCs with the reflectance reported by Blasi et al. for the MorphoColor PV colouring concept. This is displayed in Figure 4.31. The corresponding xyY coordinates under D50 illuminant are (0.3244, 0.5274, 0.1855). The results are compared to the PCE limit obtained with an optimized reflectance spectrum with rectangular bands for the same xyY coordinates, i.e. for the same colour stimulus.

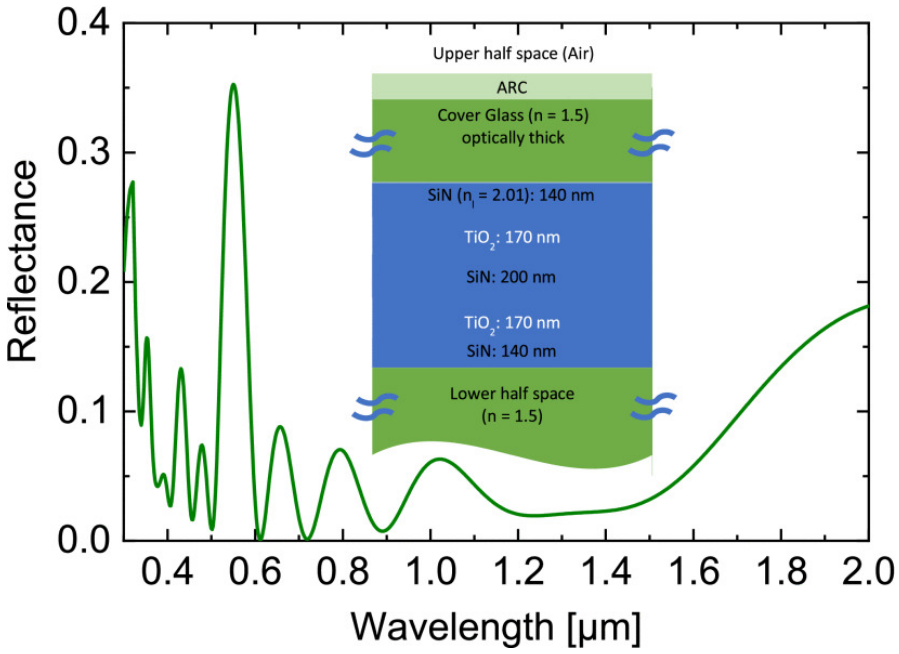

Figure 4.31: Reflectance spectrum of the optimized thin film stack for the MorphoColor concept, simulated using the transfer matrix method. A schematic illustration of the thin film stack is displayed. Reproduced from [68].

First of all, the maximum PCE limit, the optimal bandgap and subbandgaps, and the optimal rectangular-like reflectance spectra have been calculated for a SJSC and an IBSC with such xyY coordinates. The same program employed in Sections 4.1.4 and 4.2.4 has been used. Second, the same optimization has been done, but setting the reflectance fixed in the calculation, with the data from Figure 4.31.[77] For this case, it is not possible to employ the indefinite integral in the calculation of J_0 of each bandgap and subbandgap (as in equation (3.5b)), because the integral cannot be separated in different parts of the spectrum (as the reflectance is not composed of rectangular reflectance bands). Therefore, a discrete summation has been performed instead, with 0.1 nm steps, based on the integral of equation (3.1a), as shown in equation (4.1). Third, the same program has been employed to calculate the PCE limit of the solar cell with the discrete calculation of J_0, using the optimum rectangular-like reflectance spectrum previously found. The wavelength range considered for all calculations was 300-2000 nm, because it is the range of Figure 4.31. This doesn't affect the results considerably, because the amount of photons absorbed or emitted below 300 nm is very small, and no photon is absorbed or emitted above 2000 nm (they are less energetic than the optimized bandgaps and subbandgaps). The results obtained are summarized in Tables 4.8 and 4.9.

$$J_0 \sim q\frac{2\pi}{h^3c^2}\int_{E_g}^{\infty}(1-R(E))E^2 e^{\frac{-E}{k_B T_c}}dE \tag{4.1a}$$

$$J_0 \sim q\frac{2\pi}{h^3c^2}\sum_{\lambda=300nm}^{\lambda_{E_g}}(1-R(\lambda))E(\lambda)^2 e^{\frac{-E(\lambda)}{k_B T_c}}\cdot\Delta\lambda\cdot\frac{hc}{\lambda^2} \tag{4.1b}$$

Table 4.8: PCE limit and power density loss (with respect to black cell) with the reflectance spectrum of the Morphocolor concept or the optimized rectangular band reflectance spectrum, for SJSC and IBSC.

Reflectance spectrum	J_0 calculation	SJSC		IBSC	
		PCE limit (%)	P_{loss} (%)	PCE limit (%)	P_{loss} (%)
MorphoColor	Summation	31.19	7.68	45.99	7.12
Rectangular	Ind. integral	32.38	4.15	47.73	3.61
Rectangular	Summation	32.37	4.19	47.72	3.64

Table 4.9: Optimal bandgap and subbandgaps with the reflectance spectrum of the Morphocolor concept or the optimized rectangular band spectrum, for SJSC and IBSC.

Reflectance spectrum	J_0 calculation	SJSC	IBSC		
		E_g (eV)	E_{low} (eV)	E_{high} (eV)	E_g (eV)
MorphoColor	Summation	1.336	0.932	1.473	2.405
Rectangular	Ind. integral	1.135	0.932	1.467	2.400
Rectangular	Summation	1.135	0.933	1.467	2.400

Discussion

The results of the optimizations in Table 4.8 and 4.9 show that both solutions with rectangular reflectance bands give almost the same result, regardless of the method to calculate J_0. The solar cells with the reflectance of the MorphoColor concept have a lower PCE limit, with approximately double the P_{loss}, both for the SJSC and the IBSC, in comparison with the case of the rectangular-like reflectance spectrum. This is understandable, as the reflectance of the MorphoColor concept has reflection in the UV and NIR too, and some of the reflectance of the VIS is in wavelengths where the CMFs have a low value. So, photons that could be employed for photogeneration are reflected without increasing too much the colouration of the cell. Besides, the IBSC presents a 0.5% lower P_{loss} as compared to the SJSC, both for the rectangular band and the MorphoColor concept reflectance. This can come from the fact that the reflectance reported for the MorphoColor concept corresponds to a green colour. As discussed in Section 4.2.4, it can be assumed that the configuration of the bandgaps of the IBSC (with practically an equivalent circuit to two strings, one with a cell with E_g, and the other with two cells with

E_{high} and E_{low} in series) makes it less sensitive to a high reflectance in the green-yellow-red, as compared to SJSCs. This is also seen in Table 4.9, because the optimal E_g of the SJSC varies depending on the reflectance spectrum, while those of the IBSC almost don't vary. The SJSC with the MorphoColor concept has a higher optimum bandgap (1.336 eV) as compared to the case with the rectangular reflectance bands (1.135 eV), because of the switch in optimal bandgap when increasing Y (which has been observed and discussed in Section 4.1.4).

In summary, the reflectance of the MorphoColor concept produces approximately double the P_{loss} compared to the optimized rectangular band reflectance spectra both for SJSCs and IBSCs. However, the reflectance of the MorphoColor concept still allows to achieve 92-93% of the PCE of the ideal black cell. In addition, it must be mentioned that some findings of the previous sections on the study of coloured SJSCs and IBSCs have also been observed in this last section of the results, when comparing the results obtained with a more real reflectance spectrum of the MorphoColor technology to those from the ideal rectangular-like spectra.

CHAPTER 5

Conclusions

As seen in the previous chapter, many results have been produced and analysed during the development of this thesis. At this stage, it is important to remember the starting point of the presented work. The detailed balance models of the single junction and intermediate band solar cell employed are based on the knowledge from different disciplines, including solar cell physics, the physics of colours, colorimetry, state-of-the-art coloured PV technologies, and modelling. Besides, they have been based on previous work by Linge on detailed balance of IBSCs, the work by Halme et al. on coloured single junction cells, and the ECoPV program dealing with coloured series connected tandem cells using MOEAD for optimization, by Pearce et al. The mentioned disciplines and previous reported work have been the fundamental base for the development of the presented master project.

To begin with, the detailed balance models for calculating the maximum PCE limit achievable with the SJSC and the IBSC have been validated, by comparison with other results from the literature. Moreover, the code to perform the calculations has been accelerated by applying well-substantiated approximations and simplifications. In this part, a new approximate MPPT algorithm has been proposed for IBSCs. The accuracy of the proposed modifications has been checked, by contrasting their results to those obtained with the original models. Then, the possibility to have coloured solar cells has been included, by adding reflectance in the models. By doing so, the importance of including the effect of the reflectance in the radiative recombination current loss has been observed.

Once the detailed balance models for coloured opaque SJSCs and IBSCs have been properly studied and validated, they have been applied on the optimization of solar cells with the colours of the Macbeth ColorChecker chart. The results obtained for the SJSC reproduce the outcome of the work by Halme et al. It has been observed that the maximum PCE achievable depends strongly in the relative

luminosity (Y) of the colour. The PCE decreases linearly as Y increases, especially for low Y values, but the calculations show that the power loss is lower than 12% (with respect to the black cell) for the studied colours with Y smaller than 0.5. As for the optimal bandgap, it mostly presents a value around 1.34 eV for colours with small luminosity, and 1.13 eV otherwise. It is important to emphasize that apart from Y, the hue of the colour also plays a role in both the PCE limit and the optimal bandgap of the cell. The individual deviations for each colour from the linear PCE vs Y trend suggest that blue-red colours have a lower PCE than yellow-green coloured cells for the same Y, as reported by Halme et al. It must be stated that the exact results obtained in this thesis differ from those presented by Halme et al., because the illuminant employed for the calculations of the XYZ tristimulus values of the optimal reflectance spectra is different. This highlights the need to come to an agreement on the illuminant selection for the definition of colours in the research of coloured PV (together with other agreements, such as the experimental standards to measure reflection). Otherwise, when the same procedure as Halme et al. is employed for the colour coordinate manipulation, the results of this thesis reproduce theirs.

The outcome of the optimization of coloured IBSCs follows similar tendencies to that of the SJSCs, with some differences. For example, in coloured IBSCs the optimal E_g and E_{high} follow a negative linear trend with respect to the increase of Y, while the E_{low} remains constant. The power loss of coloured IBSCs with respect to the black cell has a similar value to that of SJSCs (lower than 12% for Y smaller than 0.5), but the IBSCs with bluish hue have a higher power loss compared to SJSCs, whereas it is the opposite for IBSCs with yellow-green-red hue. It is suggested that this comes from the fact that in the detailed balance model, the IBSC is equivalent to 3 cells connected in 2 parallel strings (one with a cell of E_g bandgap, and the other with the E_{low} and E_{high} cells in series).

For both the SJSC and IBSC calculations the repeatability of the MOEAD in the optimization has been checked, by running 100 iterations of the optimization of the Bluish Green cell. The results generally show a high repeatability. For SJSCs, the error due to the variability of the MOEAD makes the error caused by approximations for accelerating the code negligible. On the contrary, for IBSCs the error coming from both the variability of the MOEAD and the approximations and simplifications to accelerate the code have a similar contribution, so both must be considered. It must be said that the repeatability study has only been performed for one colour, so it would be interesting to carry it out for other colours to check if the trends are the same.

In the coloured solar cell optimizations, the modelled reflectance spectra have the shape of perfectly reflecting rectangular bands, with a null baseline. This has been demonstrated to be the optimal case for SJSCs, by Halme et al. However, it may not be the optimal case for IBSCs, as the optimal E_g falls in the VIS region. Therefore, the results obtained for IBSCs in this thesis are the optimal ones for coloured cells with the described reflectance shape, but there may be other better performing reflectance spectra types.

Finally, the maximum PCE limit achievable with the reflectance spectrum reported for the MorphoColor concept has been calculated, both for SJSCs and IBSCs. It is observed that the reflectance spectrum for the MorphoColor concept decreases the maximum PCE limit achievable with both types of cells, in comparison to the case with optimal rectangular band reflectance for the same colour. That is, the minimum power loss achievable with the rectangular band reflectance cannot be reached using one of the most advanced PV colouring technologies nowadays. Nevertheless, the MorphoColor concept could reach 92-93% of the PCE limit of the black cell. However, it must be stated that only the reflectance has been employed in the analyses of this thesis, and the absorption of the additional layers would have to be taken into consideration to obtain results which are closer to practical cases, as well as other recombination mechanisms.

To sum up, this thesis presents a detailed balance model to perform the optimization of coloured opaque SJSCs and IBSCs. Most of the analysis of the project has been done for rectangular band reflectance spectra, but the model can be applied to other reflectance shapes, as it has been done for the MorphoColor concept. The outcome of this thesis enables the evaluation of the influence of the colouring layers on the performance of SJSCs and IBSCs prior to the fabrication. Thus, it could help reduce the need for prototyping, therefore shortening the time and reducing the costs of customised module production for integration of coloured PV in multiple targets.

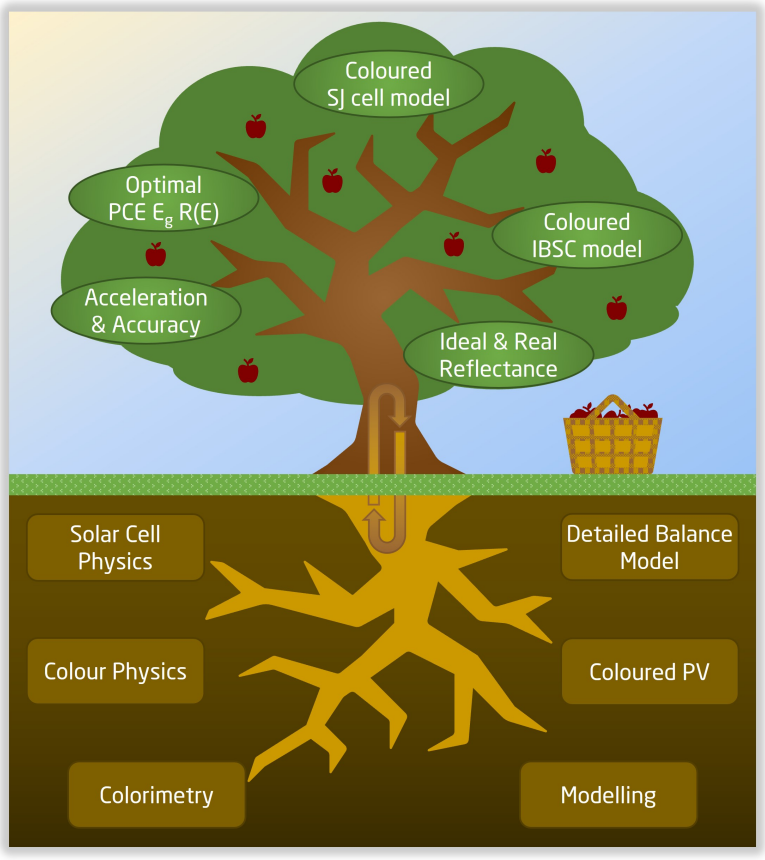

Figure 5.1: Schematic illustration of the outcome of the thesis.

5.1 Future work

As the master thesis comes to its end there are many paths that have been opened and remain unexplored, which can be considered for further research in the future. First of all, it would be interesting to study the optimal coloured opaque single junction solar cells and IBSCs, with other reflectance spectra than the rectangular bands. For example, the simulation of reflectance spectra based on Gaussian peaks has been reported already, and the original ECoPV program includes that possibility too. In addition, the number of reflectance peaks could be varied.

Following that thread, the study of the maximum PCE limit achievable with reflectance spectra of other PV colouring technologies could be of interest. Besides, other reflectance spectra obtained with the MorphoColor concept could be employed in the calculations, to analyze more achievable colours.

Employing the same model and rectangular-like reflectance spectra presented in this thesis, it would be intriguing to study the optimization of IBSCs with varying Y but constant xy chromaticity, as done by Halme et al. for the single junction cell. This could show if the different trends suggested for the blue-red and yellow-green IBSCs in the PCE vs Y regression are true or not (Figure 4.23b suggests higher PCE for yellow-green hue compared to blue-red cells, at same Y).

Another path for the continuation of this thesis could be introducing more loss mechanisms in the model. The first step could be to account for not only the reflection, but also for the absorption of light by the colouring layers, when data of actual coloured PV technologies is used. Then, the detailed balance model could be extended, to include other recombination mechanisms than just radiative recombination. The inclusion of such extensions could give a better idea of the relative loss on a real cell of a certain colour with respect to the ideal black cell.

Finally, it would be convenient to generate a GUI to facilitate the calculations using the developed code by other users. For example, it could consist of a program where one could introduce the desired colour coordinates or the reflectance spectrum of a colour filter previously measured, in order to calculate the PCE loss or the optimum bandgap of the solar cell. This could enable other people to easily perform their own desired calculations, which could accelerate and cut prices on the customization of coloured solar modules, or help other researchers reach their own conclusion about the dependency of the PCE on the colour or reflectance spectrum of the solar cells.

References

[1] *Renewables 2022*. Report. IEA, 2022, Paris, License: CC BY 4.0. URL: https://www.iea.org/reports/renewables-2022.

[2] *World Energy Outlook 2022*. Report. IEA, 2022, Paris, License: CC BY 4.0. URL: https://www.iea.org/reports/world-energy-outlook-2022.

[3] Simon Philipps and Werner Warmuth. *Photovoltaics Report*. Report. Fraunhofer ISE, 21 February 2023 2023. URL: https://www.ise.fraunhofer.de/en/publications/studies/photovoltaics-report.html.

[4] Felix Haase et al. "Laser contact openings for local poly-Si-metal contacts enabling 26.1%-efficient POLO-IBC solar cells". In: *Solar Energy Materials and Solar Cells* 186 (2018), pp. 184–193. ISSN: 0927-0248. DOI: https://doi.org/10.1016/j.solmat.2018.06.020. URL: https://www.sciencedirect.com/science/article/pii/S0927024818303076.

[5] NREL. *Best research-cell efficiency chart*. URL: https://www.nrel.gov/pv/cell-efficiency.html.

[6] Martin A Green. *Third generation photovoltaics : advanced solar energy conversion*. eng. Berlin, 2003.

[7] Patrick Schygulla et al. *Quadruple Junction Solar Cell with 47.6 % Conversion Efficiency under Concentration*. 2022. URL: https://publica.fraunhofer.de/handle/publica/436210.

[8] Marie Beyer. *French consortium to set up 5 GW factory for 4T tandem perovskite-silicon modules*. Nov. 2022. URL: https://www.pv-magazine.com/2022/11/14/french-consortium-to-set-up-5-gw-factory-for-4t-tandem-perovskite-silicon-modules/.

[9] S. A. Blokhin et al. "AlGaAs/GaAs photovoltaic cells with an array of InGaAs QDs". In: *Semiconductors* 43.4 (2009), pp. 514–518. ISSN: 1090-6479. DOI: 10.1134/S1063782609040204. URL: https://doi.org/10.1134/S1063782609040204.

[10] K. Sablon et al. "GaAs quantum dot solar cell under concentrated radiation". In: *Applied Physics Letters* 107.7 (2015). doi: 10.1063/1.4928669, p. 073901. ISSN: 0003-6951. DOI: 10.1063/1.4928669. URL: https://doi.org/10.1063/1.4928669.

[11] Antonio Luque and Antonio Martı. "Increasing the Efficiency of Ideal Solar Cells by Photon Induced Transitions at Intermediate Levels". In: *Phys. Rev. Lett.* 78 (26 June 1997), pp. 5014–5017. DOI: 10.1103/PhysRevLett.78.5014. URL: https://link.aps.org/doi/10.1103/PhysRevLett.78.5014.

[12] *Photovoltaic applications*. URL: https://www.nrel.gov/pv/applications.html.

[13] Izumi Kaizuka and Gaëtan Masson. 2022. URL: https://iea-pvps.org/trends_reports/trends-2022/.

[14] Tiantian Zhang, Meng Wang, and Hongxing Yang. "A Review of the Energy Performance and Life-Cycle Assessment of Building-Integrated Photovoltaic (BIPV) Systems". In: *Energies* 11.11 (2018). ISSN: 1996-1073. DOI: 10.3390/en11113157. URL: https://www.mdpi.com/1996-1073/11/11/3157.

[15] Martina Pelle et al. *Coloured BIPV Technologies: Methodological and Experimental Assessment for Architecturally Sensitive Areas*. Electronic Article. 2020. DOI: 10.3390/en13174506.

[16] Martina Pelle et al. *Opaque Coloured Building Integrated Photovoltaic (BIPV): A Review of Models and Simulation Frameworks for Performance Optimisation*. Electronic Article. 2023. DOI: 10.3390/en16041991.

[17] Lars Oliver Grobe et al. "Designing the colour, pattern and specularity of building integrated photovoltaics". In: 2020.

[18] Arne Røyset, Tore Kolås, and Bjørn Petter Jelle. "Coloured building integrated photovoltaics: Influence on energy efficiency". In: *Energy and Buildings* 208 (2020), p. 109623. ISSN: 0378-7788. DOI: https://doi.org/10.1016/j.enbuild.2019.109623. URL: https://www.sciencedirect.com/science/article/pii/S0378778819322091.

[19] A. Røyset et al. *Efficiency Loss in Coloured Photovoltaics Estimating the Contribution from Reflection Loss and Absorption Loss*. Conference Paper. 2021. DOI: 10.4229/EUPVSEC20212021-4AV.2.10.

[20] Janne Halme and Pyry Mäkinen. "Theoretical efficiency limits of ideal coloured opaque photovoltaics". In: *Energy Environmental Science* 12.4 (2019), pp. 1274–1285. ISSN: 1754-5692. DOI: 10.1039/C8EE03161D. URL: http://dx.doi.org/10.1039/C8EE03161D.

[21] Zhenpeng Li and Tao Ma. "Theoretic efficiency limit and design criteria of solar photovoltaics with high visual perceptibility". In: *Applied Energy* 324 (2022), p. 119761. ISSN: 0306-2619. DOI: https://doi.org/10.1016/j.apenergy.2022.119761. URL: https://www.sciencedirect.com/science/article/pii/S0306261922010431.

[22] Jenny Nelson. *The Physics of Solar Cells*. doi:10.1142/p276. PUBLISHED BY IMPERIAL COLLEGE PRESS and DISTRIBUTED BY WORLD SCIENTIFIC PUBLISHING CO., 2003, p. 384. ISBN: 978-1-86094-340-9. DOI: doi:10.1142/p276. URL: https://doi.org/10.1142/p276.

[23] Max Karl Ernst Ludwig Planck. "Zur Theorie des Gesetzes der Energieverteilung im Normalspectrum". In: *Verhandl. Dtsc. Phys. Ges.* 2 (1900), p. 237. URL: http://cds.cern.ch/record/262745.

[24] *Tables for Reference Solar Spectral Irradiances: Direct Normal and Hemispherical on 37 Tilted Surface*. DOI: 10.1520/g0173-03r08. URL: http://dx.doi.org/10.1520/G0173-03R08.

[25] Abdelrahman Attia. *P-N Junction*. Apr. 2020. DOI: 10.13140/RG.2.2.13294.23363.

[26] Joel Jean et al. "Pathways for solar photovoltaics". In: *Energy Environ. Sci.* 8 (4 2015), pp. 1200–1219. DOI: 10.1039/C4EE04073B. URL: http://dx.doi.org/10.1039/C4EE04073B.

[27] Yong Li. "Synthesis, Characterization, and Photovoltaic Applications of Mesoscopic Phthalocyanine Structures". PhD thesis. Nov. 2011. DOI: 10.13140/RG.2.1.1834.0722.

[28] Yuguo Tao. "Screen-Printed Front Junction n-Type Silicon Solar Cells". In: *Printed Electronics*. Ed. by Ilgu Yun. Rijeka: IntechOpen, 2016. Chap. 4. DOI: 10.5772/63198. URL: https://doi.org/10.5772/63198.

[29] C.B. Honsberg and S.G. Bowden. *Detailed Balance*. 2019. URL: www.pveducation.org.

[30] Martin J. Klein. "Principle of Detailed Balance". In: *Phys. Rev.* 97 (6 Mar. 1955), pp. 1446–1447. DOI: 10.1103/PhysRev.97.1446. URL: https://link.aps.org/doi/10.1103/PhysRev.97.1446.

[31] William Shockley and Hans J. Queisser. "Detailed Balance Limit of Efficiency of p-n Junction Solar Cells". In: *Journal of Applied Physics* 32.3 (1961), pp. 510–519. DOI: 10.1063/1.1736034. eprint: https://doi.org/10.1063/1.1736034. URL: https://doi.org/10.1063/1.1736034.

[32] T. Tiedje et al. "Limiting efficiency of silicon solar cells". In: *IEEE Transactions on Electron Devices* 31.5 (1984), pp. 711–716. DOI: 10.1109/T-ED.1984.21594.

[33] Turid Reenaas. *Third generation solar cells; Nanotechnology in solar cells*. 2022.

[34] Sven Rühle. "Tabulated values of the Shockley–Queisser limit for single junction solar cells". In: *Solar Energy* 130 (2016), pp. 139–147. ISSN: 0038-092X. DOI: https://doi.org/10.1016/j.solener.2016.02.015. URL: https://www.sciencedirect.com/science/article/pii/S0038092X16001110.

[35] Takeshi Tayagaki et al. "Three-Terminal Tandem Solar Cells With a Back-Contact-Type Bottom Cell Bonded Using Conductive Metal Nanoparticle Arrays". In: *IEEE Journal of Photovoltaics* 10.2 (2020), pp. 358–362. DOI: 10.1109/JPHOTOV.2019.2957661.

[36] William E. McMahon et al. "A framework for comparing the energy production of photovoltaic modules using 2-, 3-, and 4-terminal tandem cells". In: *Sustainable Energy Fuels* 7 (2 2023), pp. 461–470. DOI: 10.1039/D2SE01167K. URL: http://dx.doi.org/10.1039/D2SE01167K.

[37] Emily L. Warren et al. “A Taxonomy for Three-Terminal Tandem Solar Cells”. In: *ACS Energy Letters* 5.4 (2020), pp. 1233–1242. DOI: 10.1021/acsenergylett.0c00068. eprint: https://doi.org/10.1021/acsenergylett.0c00068. URL: https://doi.org/10.1021/acsenergylett.0c00068.

[38] Andrew S Brown and Martin A Green. “Detailed balance limit for the series constrained two terminal tandem solar cell”. In: *Physica E: Low-dimensional Systems and Nanostructures* 14.1 (2002), pp. 96–100. ISSN: 1386-9477. DOI: https://doi.org/10.1016/S1386-9477(02)00364-8. URL: https://www.sciencedirect.com/science/article/pii/S1386947702003648.

[39] Joseba Miren Ormaetxea Orobengoa. *Specialization project. Initial photoluminescence spectroscopy studies of TiO2*. Norwegian University of Science and Technology, NTNU, 2022, pp. 7–8.

[40] Stephen P. Bremner, Michael Y. Levy, and Christiana B. Honsberg. “Limiting efficiency of an intermediate band solar cell under a terrestrial spectrum”. In: *Applied Physics Letters* 92.17 (Apr. 2008). 171110. ISSN: 0003-6951. DOI: 10.1063/1.2907493. eprint: https://pubs.aip.org/aip/apl/article-pdf/doi/10.1063/1.2907493/14393746/171110_1_online.pdf. URL: https://doi.org/10.1063/1.2907493.

[41] Ramiro Í et al. “Review of Experimental Results Related to the Operation of Intermediate Band Solar Cells”. In: *IEEE Journal of Photovoltaics* 4.2 (2014), pp. 736–748. ISSN: 2156-3403. DOI: 10.1109/JPHOTOV.2014.2299402.

[42] Iñigo Ramiro and Antonio Martí. “Intermediate band solar cells: Present and future”. In: *Progress in Photovoltaics: Research and Applications* 29.7 (2021), pp. 705–713. DOI: https://doi.org/10.1002/pip.3351. eprint: https://onlinelibrary.wiley.com/doi/pdf/10.1002/pip.3351. URL: https://onlinelibrary.wiley.com/doi/abs/10.1002/pip.3351.

[43] Douglas J.R. Baquião and Gustavo M. Dalpian. “Computational screening of bulk materials with intrinsic intermediate band”. In: *Computational Materials Science* 158 (2019), pp. 382–388. ISSN: 0927-0256. DOI: https://doi.org/10.1016/j.commatsci.2018.11.030. URL: https://www.sciencedirect.com/science/article/pii/S0927025618307572.

[44] Kurt Nassau and David G. Stork. “The Physics and Chemistry of Color: The Fifteen Causes of Color”. In: 1983.

[45] Kurt Nassau. *"colour", Encyclopedia Britannica*. 27. Mar 2023, accessed 30. Mar 2023. URL: https://www.britannica.com/science/color.

[46] Kurt Nassau. “7 - The Physics and Chemistry of Color: the 15 Mechanisms”. In: *The Science of Color (Second Edition)*. Ed. by Steven K. Shevell. Second Edition. Amsterdam: Elsevier Science Ltd, 2003, pp. 247–280. ISBN: 978-0-444-51251-2. DOI: https://doi.org/10.1016/B978-044451251-2/50008-8. URL: https://www.sciencedirect.com/science/article/pii/B9780444512512500088.

[47] Zhenpeng Li et al. “Transparent and Colored Solar Photovoltaics for Building Integration”. In: *Solar RRL* 5.3 (2021). https://doi.org/10.1002/solr.202000614, p. 2000614. ISSN: 2367-198X. DOI: https://doi.org/10.1002/solr.202000614. URL: https://doi.org/10.1002/solr.202000614.

[48] *ISO 10526:1999(E), 1999.*

[49] International Commission on Illumination (CIE). *CIE standard illuminant D50, 1 nm wavelength steps, original source: ISO/CIE FDIS 11664-2:2022, Table B.1.* DOI: 10.25039/cie.ds.etgmuqt5. URL: http://dx.doi.org/10.25039/CIE.DS.etgmuqt5.

[50] Waveform. *What is D50 for Graphic Arts Printing?* Sept. 2018. URL: https://www.waveformlighting.com/color-matching/what-is-d50-for-graphic-arts-printing.

[51] International Commission on Illumination (CIE). *CIE standard illuminant D65, 1 nm wavelength steps, original source: ISO/CIE FDIS 11664-2:2022, Table B.1.* DOI: 10.25039/CIE.DS.hjfjmt59. URL: https://cie.co.at/datatable/cie-standard-illuminant-d65.

[52] Schanda János. *Colorimetry: Understanding the CIE system.* Wiley, 2007.

[53] E.C. Carter et al. 2018.

[54] Chet S. Haase and Gary W. Meyer. “Modeling Pigmented Materials for Realistic Image Synthesis”. In: *ACM Trans. Graph.* 11.4 (Oct. 1992), pp. 305–335. ISSN: 0730-0301. DOI: 10.1145/146443.146452. URL: https://doi.org/10.1145/146443.146452.

[55] P. Pearce. *ECoPV.* https://github.com/qpv-research-group/ECoPV. 2023.

[56] T Smith and J Guild. “The C.I.E. colorimetric standards and their use”. In: *Transactions of the Optical Society* 33.3 (Jan. 1931), p. 73. DOI: 10.1088/1475-4878/33/3/301. URL: https://dx.doi.org/10.1088/1475-4878/33/3/301.

[57] Richard R. Lunt. “Theoretical limits for visibly transparent photovoltaics”. In: *Applied Physics Letters* 101.4 (2012), p. 043902. DOI: 10.1063/1.4738896. eprint: https://doi.org/10.1063/1.4738896. URL: https://doi.org/10.1063/1.4738896.

[58] Charles A. Poynton. “Digital Video and HDTV Algorithms and Interfaces”. In: 2012, p. 275.

[59] David L. MacAdam. “Visual Sensitivities to Color Differences in Daylight∗”. In: *J. Opt. Soc. Am.* 32.5 (May 1942), pp. 247–274. DOI: 10.1364/JOSA.32.000247. URL: https://opg.optica.org/abstract.cfm?URI=josa-32-5-247.

[60] Sappi Limited. 2013, p. 5.

[61] *PVPS Task 15 - Coloured BIPV : Market, Research and Development 2022.* Report. IEA, 2022, Paris, License: CC BY 4.0. URL: https://iea-pvps.org/key-topics/iea-pvps-15-r07-coloured-bipv-report/.

[62] Bruce Justin Lindbloom. *Delta E (CIE 2000).* Apr. 2017. URL: http://www.brucelindbloom.com/index.html?Eqn_DeltaE_CIE2000.html.

[63] Guoliang Shang, Manfred Eich, and Alexander Petrov. "Photonic glass based structural color". In: *APL Photonics* 5.6 (June 2020). 060901. ISSN: 2378-0967. DOI: 10.1063/5.0006203. eprint: https://pubs.aip.org/aip/app/article-pdf/doi/10.1063/5.0006203/13561652/060901_1_online.pdf. URL: https://doi.org/10.1063/5.0006203.

[64] Gerhard Peharz et al. "Application of plasmonic coloring for making building integrated PV modules comprising of green solar cells". In: *Renewable Energy* 109 (2017), pp. 542–550. ISSN: 0960-1481. DOI: https://doi.org/10.1016/j.renene.2017.03.068. URL: https://www.sciencedirect.com/science/article/pii/S0960148117302598.

[65] David L. MacAdam. "Maximum Attainable Luminous Efficiency of Various Chromaticities". In: *J. Opt. Soc. Am.* 40.2 (Feb. 1950), pp. 120–120. DOI: 10.1364/JOSA.40.000120. URL: https://opg.optica.org/abstract.cfm?URI=josa-40-2-120.

[66] Tilmann E. Kuhn et al. "Review of technological design options for building integrated photovoltaics (BIPV)". In: *Energy and Buildings* 231 (2021), p. 110381. ISSN: 0378-7788. DOI: https://doi.org/10.1016/j.enbuild.2020.110381. URL: https://www.sciencedirect.com/science/article/pii/S0378778819339155.

[67] HQ Kromatix SA. *Kromatix Technology: Adding Colour to the Solar Industry*. May 2021. URL: https://demo.kromatix.com/technology/.

[68] Benedikt Bläsi et al. "The MorphoColor Concept for Colored Photovoltaic Modules". In: *IEEE Journal of Photovoltaics* 11.5 (2021), pp. 1305–1311. DOI: 10.1109/JPHOTOV.2021.3090158.

[69] Verena Neder, Stefan L. Luxembourg, and Albert Polman. "Efficient colored silicon solar modules using integrated resonant dielectric nanoscatterers". In: *Applied Physics Letters* 111.7 (2017), p. 073902. DOI: 10.1063/1.4986796. eprint: https://doi.org/10.1063/1.4986796. URL: https://doi.org/10.1063/1.4986796.

[70] Kyu-Tae Lee et al. "Colored ultrathin hybrid photovoltaics with high quantum efficiency". In: *Light: Science & Applications* 3.10 (Oct. 2014), e215–e215. ISSN: 2047-7538. DOI: 10.1038/lsa.2014.96. URL: https://doi.org/10.1038/lsa.2014.96.

[71] Christer Linge. "Master Thesis: Modeling of Intermediate Band Tandem Solar Cell". Thesis. 2011. URL: https://ntnuopen.ntnu.no/ntnu-xmlui/handle/11250/246422.

[72] J.G. Davidson C. S. McCamy H. Marcus. "A Color-Rendition Chart". In: *Journal of Applied Photographic Engineering* 2 (1976), pp. 95–99.

[73] C. B. Honsberg and S. G. Bowden. *Voltage at the maximum power point - VMP*. 2019. URL: https://www.pveducation.org/pvcdrom/voltage-at-the-maximum-power-point-vmp.

[74] Andreas Pusch, Phoebe Pearce, and Nicholas J. Ekins-Daukes. "Analytical Expressions for the Efficiency Limits of Radiatively Coupled Tandem Solar Cells". In: *IEEE Journal of Photovoltaics* 9.3 (2019), pp. 679–687. DOI: 10.1109/JPHOTOV.2019.2903180.

[75] D. Pascale. “RGB Coordinates of the Macbeth Color Checker”. In: (Jan. 2006).

[76] Qingfu Zhang and Hui Li. “MOEA/D: A Multiobjective Evolutionary Algorithm Based on Decomposition”. In: *IEEE Transactions on Evolutionary Computation* 11.6 (2007), pp. 712–731. DOI: 10.1109/TEVC.2007.892759.

[77] B. Tummers. 2006. URL: https://datathief.org/.

Appendix

A Detailed balance model for single junction solar cell with reflection, comparison to Li et al.

In this appendix, the results obtained with the the detailed balance model (Boltzmann-Lambert approach and the Sunlight-reflected submodel) for single junction solar cell (see Section 4.1.3) are compared to the results reported by Li et al.[47] for fully transparent solar cells. For that purpose, the reflectance spectrum introduced in the calculations with the Sunlight-reflected submodel has been narrowed to 435-670 nm, in order to match the reflectance spectrum of the work by Li et al. Figure A.2 shows the maximum PCE limit obtained, together with the results of Li et al.

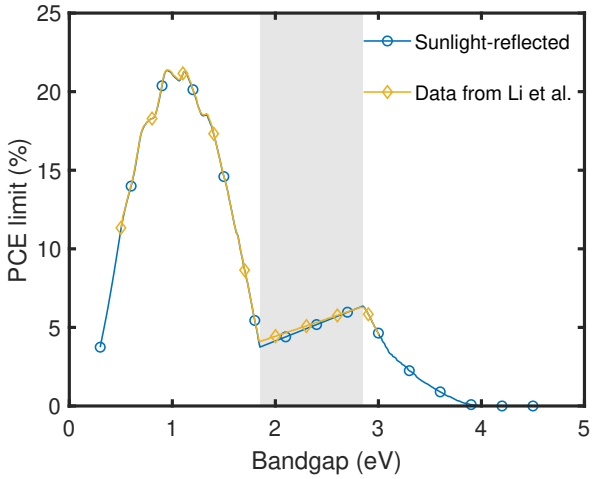

Figure A.2: Maximum PCE limit of single junction solar cell with R=1 between 435-670 nm (shaded in grey), based on the Boltzmann-Lambert approach, with the Sunlight-reflected submodel for introducing the reflectance. The data from Li et al. has been extracted using DataThief.[47, 77]

It can be seen that the results obtained with the detailed balance model generally match the reported results by Li et al. However, the match is not as good in the energy range where the reflection band is located, and no explanation has been found for that.

Besides, it must be stated that the results by Li et al. actually should not match those of the implemented model in this thesis. As the work by Li et al. handled transparent solar cells, their model does not include the perfect back reflector, so the solar cell is able to emit blackbody radiation from the back surface as well, doubling the loss by recombination current, as described by Halme et al. ("semi-transparent cells assume no back-reflector").[20]

If this technicality is added in the detailed balance model implemented in Matlab for this thesis, the PCE limits obtained are lower, as shown in Figure A.3.

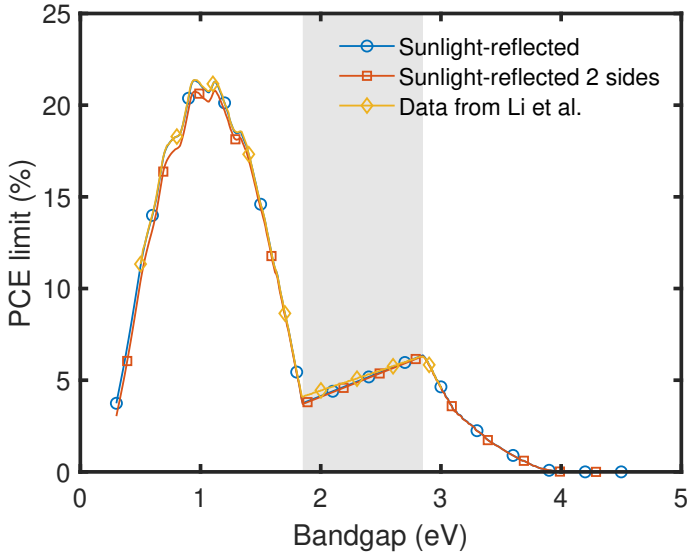

Figure A.3: Maximum PCE limit of single junction solar cell with R=1 between 435-670 nm (shaded in grey), based on the Boltzmann-Lambert approach, with the Sunlight-reflected submodel for introducing the reflectance. The "Sunligh-reflected 2 sides" line considers double the current density loss due to recombination, because the transparent solar cells assume no back-reflector. The data from Li et al. has been extracted using DataThief.[47, 77]

As seen in the figure above, when considering that transparent solar cells have no back-reflector the efficiency of the solar cell decreases (because the current density loss due to radiative recombination doubles). So, the results obtained considering this do not exactly match the results by Li et al. Moreover, it has been observed that if the resolution of the summation for the AM1.5G spectrum is refined from 1 nm to 0.1 nm, the obtained PCE limits exceed the results reported by Li et al. It must be stated that the report by Li et al. is missing information about the resolution of the AM1.5G spectral irradiance they use, which would be crucial to make a more proper comparison.

Therefore, out of this discussion it is concluded that the graph of the PCE

limit as a function of the bandgap obtained with the model of this thesis follows the same trend as the results reported by Li et al. for transparent solar cells. However, a more detailed comparison would require a better knowledge of their model, f.e. in terms of their resolution in the incident AM1.5G spectral irradiance.

B Comparison of obtained results to Halme et al.

Figure 4.8 in Section 4.1.4 shows that the PCE limits obtained for the single junction solar cells with the 24 colours of the Macbeth ColorChecker chart follow the same trend as reported by Halme et al.[20] However, if the exact values of the PCE limits are compared, one can see that they differ to those reported by Halme et al. The difference in PCE limit is represented in Figure B.4a, and Figure B.4b shows the difference in the optimal bandgap values found.

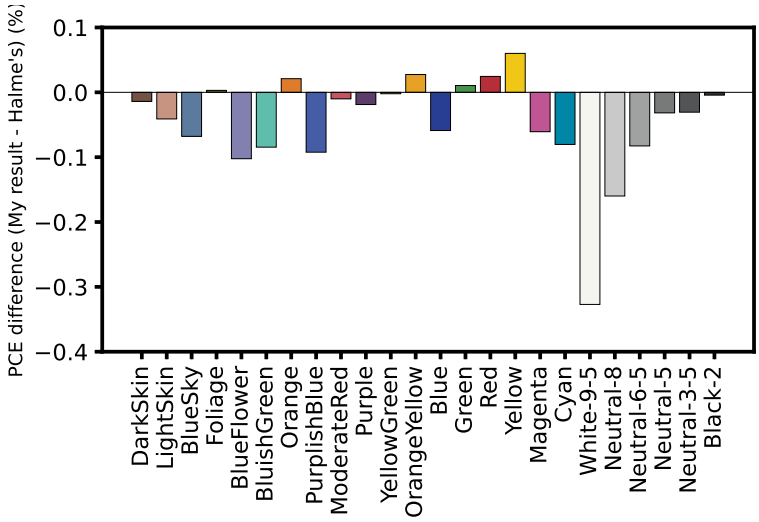

(a)

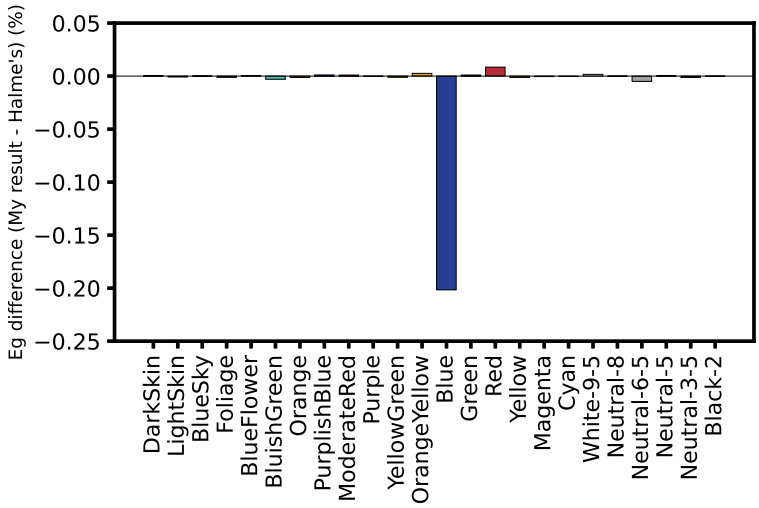

(b)

Figure B.4: Difference to Halme's results, for optimized coloured single junction solar cells with colours of the Macbeth ColorChecker chart: (a) PCE limit difference (absolute percentage) and (b) Bandgap difference.

The reason behind that is that Halme et al. used AM1.5G as illuminant to calculate the XYZ tristimulus values of the optimized colour based on the reflectance spectrum. On the contrary, in this thesis D50 has been employed as illuminant for the calculation of XYZ values. That means that both works are optimizing

for slightly different target colours: Halme et al. optimized the reflectance spectra so that under AM1.5G illumination the colour appearance would be the same as that of the Macbeth ColorChecker chart under D50 illuminant. However, the same reflectance spectra will have another appearance under D50 illuminant. On the contrary, in this thesis, the optimized reflectance spectra appear the same as the Macbeth ColorChecker chart, when both are illuminated with the D50 illuminant.

The optimization for the 24 colours has been run again, but employing the AM1.5G as illuminant for calculating the XYZ values of the optimized colours (as in the work by Halme et al.). In this case, as shown by Figure B.5a, the obtained results are more similar to those reported by Halme et al. Finally, Figure B.5b shows the appearance of these new reflectance spectra under D50 illuminant and AM1.5G illuminant, compared to the colours of the Macbeth ColorChecker chart under D50 illuminant. One can see the slight difference in colour between the first row (the reflectance spectra obtained by Halme's method under D50 illuminant) and the other two rows (the reflectance spectra obtained by Halme's method under AM1.5G illuminant, and the Macbeth ColorChecker chart under D50 illuminant, which are indistinguishable).

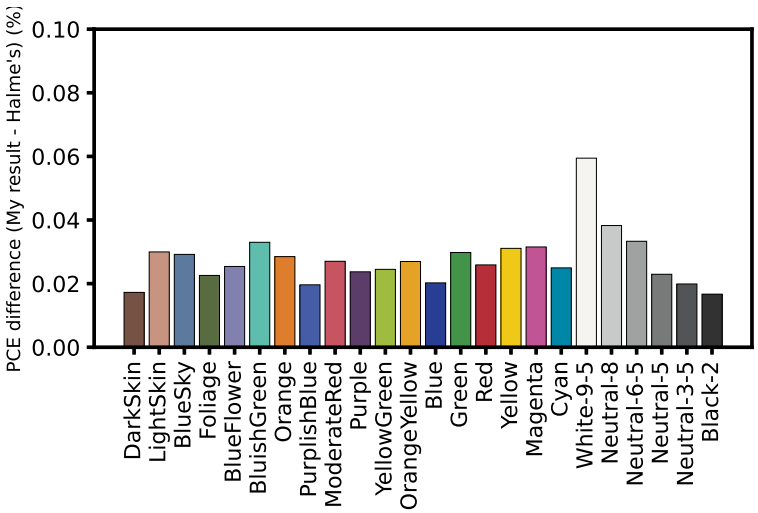

(a)

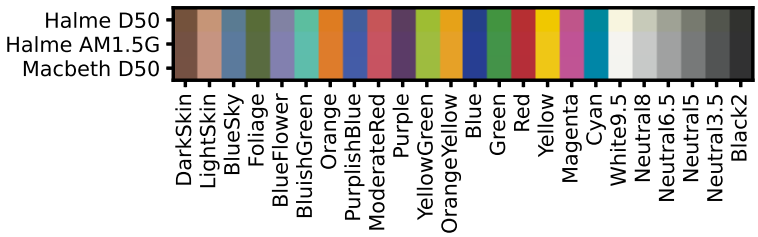

(b)

Figure B.5: (a) Difference to Halme's results, for optimized coloured single junction solar cells with colours of the Macbeth ColorChecker chart using AM1.5G as illuminant to calculate the XYZ tristimulus values of optimized reflectance spectra. (b) Appearance of these new reflectance spectra under D50 illuminant and AM1.5G illuminant, compared to the colours of the Macbeth ColorChecker chart under D50 illuminant.

C Distribution of optimal bandgap in 100 runs for Bluish Green single junction solar cell

In Section 4.1.4.1, Figure 4.14b shows that the optimal bandgap results have values between 1.125 and 1.140 eV, for the 100 optimization repetitions of the Bluish Green single junction solar cell. These seem to cluster around 2 main bandgaps (1.1295 and 1.1345 eV), as shown by Figure 4.14b. The explanation for that is given in this appendix

The efficiency for coloured single junction solar cells with the reflectance spectrum of Figure 4.13 with a certain bandgap can be calculated applying the detailed balance model, with the approximations and simplifications already explained (see Sections 4.1.2 and 4.1.3). If one calculates the efficiency for the bandgap range shown in Figure 4.14b, for bandgaps between 1.12 and 1.14 eV, with 0.0001 eV steps, the PCE limits that are obtained are displayed in Figure C.6.

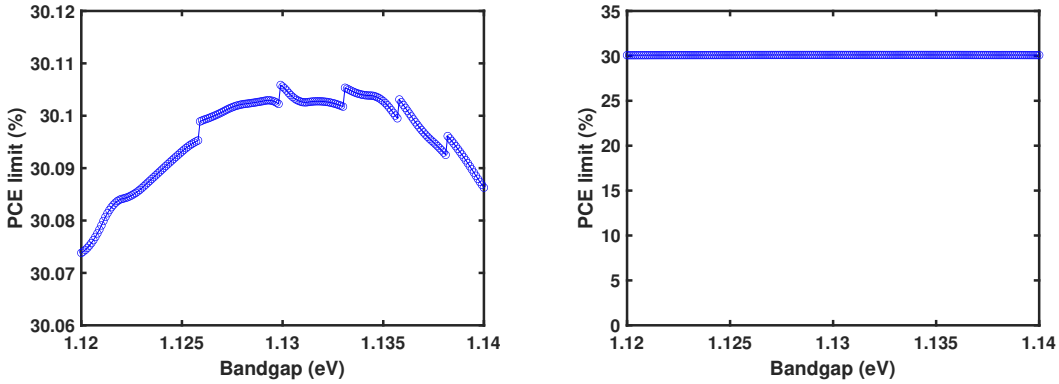

(a) (b)

Figure C.6: PCE limit of Bluish Green solar cell with bandgap between 1.12 and 1.14 eV, with varying scale in Y axis.

In Figure C.6a, the maximum PCE limit presents two peaks with 30.1059% and 30.1053% at 1.1299 eV and 1.1331 eV bandgap values, respectively. Therefore, it can be concluded that the distribution of bandgap results of the 100 optimization runs clusters around those peaks.

In addition, one can see that the graph in Figure C.6a presents some sudden changes in PCE limit. The explanation to these can be found in Table C.1 and Figure C.7.

Table C.1: Bandgap values near maximum PCE limit, around which the results of the MOEAD cluster

Bandgap (eV)	Equivalent wavelength (nm)
1.1296	1097.593
1.1297	1097.496
1.1298	1097.399
1.1299	1097.302
1.1300	1097.205
1.1301	1097.107

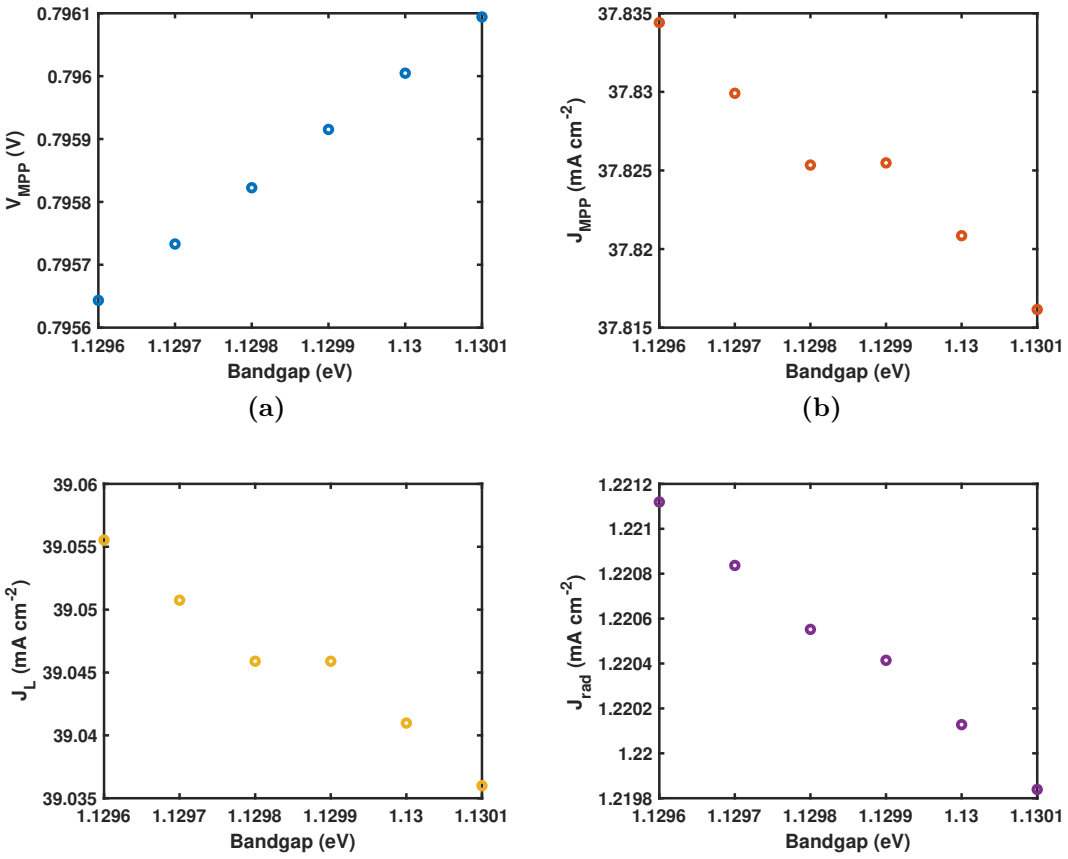

Figure C.7: Current voltage characteristic of single junction solar cell with bandgap near maximum PCE limit, around which the results of the MOEAD cluster: (a) V_{MPP}, (b) J_{MPP}, (c) J_L, and (d) J_{rec}.

One of the sharp increases in PCE in Figure C.6a occurs at a 1.1299 eV bandgap. It can be seen that from 1.1298 eV to 1.1299 eV, the V_{MPP} increases (Figure C.7a), but the J_{MPP} does not decrease, it remains constant. This is what gives the sharp increase in PCE limit at 1.1299 eV. The reason behind that is that from 1.1298 to 1.1299 eV, the equivalent wavelength change is 1097.399 to 1097.302 nm, so the first decimal place is not changed. Therefore, the absorp-

tion of photons from the Sun (and J_L) is kept constant, causing J_{MPP} to remain constant.

So, the sharp increases in Figure C.6a come from the spectral resolution (0.1 nm) in the summation to calculate the photocurrent due to absorption of the AM1.5G spectrum (J_L, see equation (3.4)). It is quite surprising that the bandgap step (0.0001 eV) in the bandgap range studied (1.12-1.14 eV), is more or less equivalent to the wavelength resolution (0.1 nm), which causes the sharp peaks to be so clear. However, these artifacts are almost irrelevant in practicals term (see Figure C.6b).

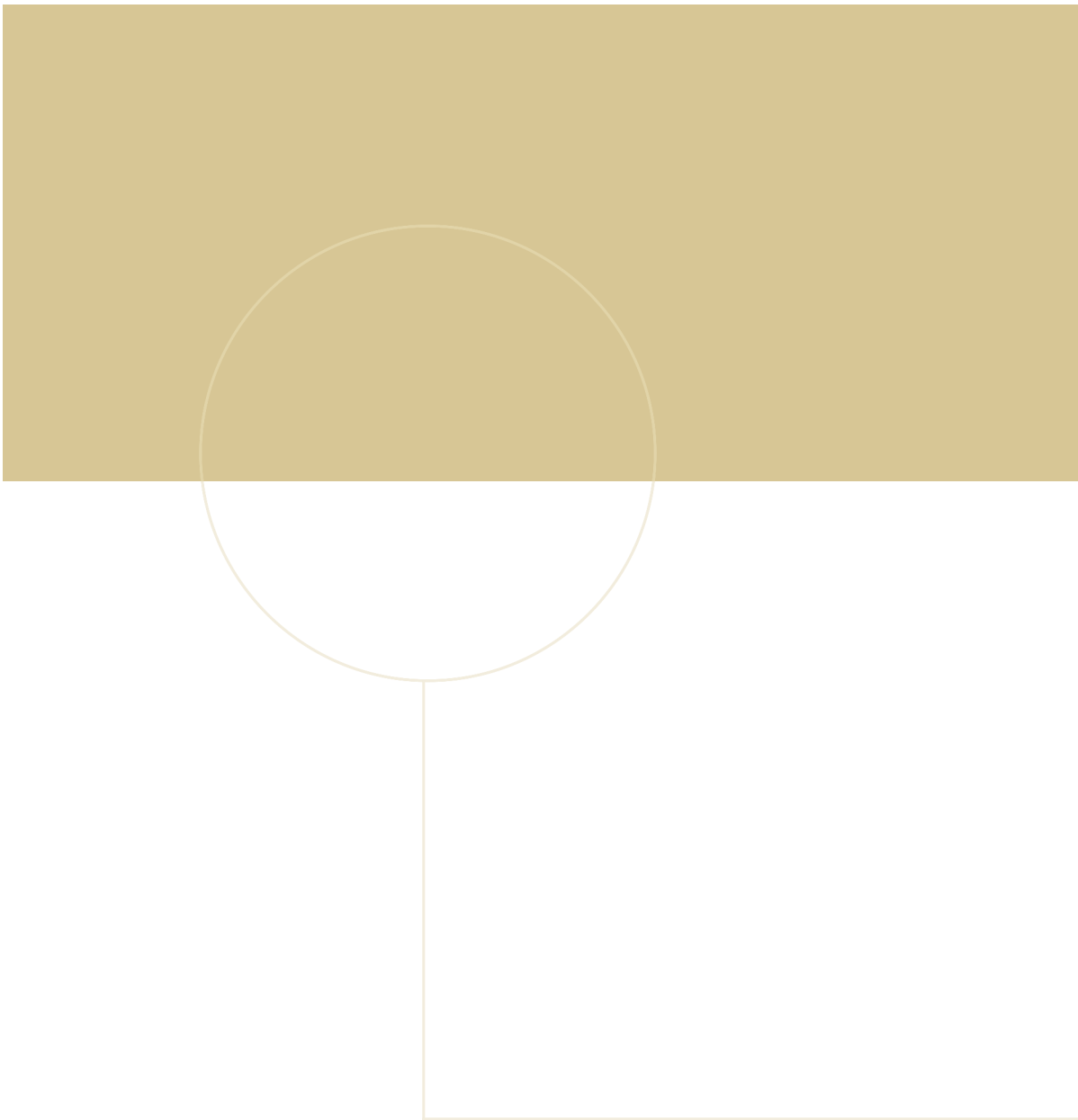

NTNU

Norwegian University of
Science and Technology